Master Thesis: Water surface monitoring using GNSS-R Opportunity Signals

European Master of Research on Information and Communication Technologies

Title: MERIT master

Author: Alberto Alonso Arroyo

Advisors: Prof. Adriano José Camps Carmona

Dr. Nereida Rodríguez Álvarez

Year: 2012

ABSTRACT

This Master Thesis follows the future research lines recommended in Dr. Nereida Rodríguez Álvarez Ph.D Thesis dissertation. It is based on the application of the Interference Pattern Technique (IPT) on dynamic surfaces trying to monitor the water-level.

The Global Navigation Satellite Systems (GNSS) signals are presented and then the Delay Doppler Map (DDM) technique and the IPT technique are introduced in detail. The basic equations are presented to fully understand the concepts. Both techniques can be applied today to Earth observation to retrieve geophysical parameters of the surface, such as the soil moisture, the topography and the wind speed.

Then, the instrument that implements the IPT technique is described: it is the Soil Moisture Interference pattern technique GNSS-R Observations at L-band (SMIGOL) reflectometer. SMIGOL is an autonomous instrument consisting of a patch antenna with a symmetric pattern, a commercial GPS receiver, a GPS amplifier, a datalogger, a microcontroller, and a well-tailored power supply system containing batteries, solar panels, a buck boost power supply, and a battery charger.

Some of the applications developed in the remote sensing laboratory (RSLab) using the IPT are presented, including soil moisture, vegetation height, water surface monitoring on reservoirs and topography. All these applications are supported with a critical analysis, and with the results of different field campaigns performed to validate the algorithms developed.

Finally, a very detailed analysis of a field campaign performed in Vilanova i la Geltrú, Catalunya, Spain, to see how the IPT performs over dynamic surfaces is shown. All the intermediate steps of the signal processing are explained. From this campaign two different conclusions result; water-level monitoring cannot be performed under the same hypotheses as in reservoirs, and; the high dynamics of the water appear as a noise in the interference patterns which is correlated to the wind speed. An empirical formula relating the IPT observables and the wind speed is derived.

ACRONYMS LIST

ACF	Auto Correlation Function
AM	Amplitude Modulation
BPSK	Binary Phase Shift Keying
CDMA	Code Division Multiple Access
DBF	Digital Beam Forming
DDM	Delay Doppler Map
DSSS	Direct Sequence Spread Spectrum
FFT	Fast Fourier Transform
FOC	Fully Operational Capability
FOV	Field Of View
GEO	Geostationary Earth Orbit
GNSS	Global Navigation Satellite Systems
GPS	Global Positioning System
H-Pol	Horizontal Polarisation
IFFT	Inverse Fast Fourier Transform
IPT	Interference Pattern Technique
LEO	Low Earth Orbit
LFSR	Linear Feedback Shift Register
LHCP	Left Hand Circular Polarisation
LNA	Low Noise Amplifier
MERITXELL	Multi-frequency Experimental Radiometer With Interference Tracking For Experiments Over Land And Littoral
PRN	Pseudo Random Noise
PRSG	Passive Remote Sensing Group
RADAR	RAnge Detection And Ranging
RHCP	Right Hand Circular Polarisation
RL	Return Loss
RSLab	Remote Sensing Laboratory
SMIGOL	Soil Moisture Interference pattern technique GNSS-R Observations at L-band
SMOS	Soil Moisture Ocean Salinity
SNR	Signal to Noise Ratio

SSS	Sea Surface Salinity
TSIP	Trimble Standard Interface Protocol
UART	Universal Asynchronous Receiver Transmitter
UPC	Universitat Politècnica de Catalunya
V-Pol	Vertical Polarisation

OUTLINE

LIST OF FIGURES

1 CHAPTER 1 INTRODUCTION

1.1 REMOTE SENSING AT RSLAB

For more than 20 years, Universistat Politècnia de Catalunya (UPC), and specially Remote Sensing Laboratory Group (RSLab), have been interested in developing remote sensing techniques for Earth observation. Active and passive instruments, such as radars or radiometers, have been developed over the years mainly dedicated to monitor environment.

Earth observation is a necessary element to characterise all natural effects that happen on Earth and especially global warming, which is one of the main scientists' and environmentalists' concern. RSLab group has been collaborating with scientific groups showing how remote sensing techniques can be useful to estimate and retrieve geophysical parameters, which can be used to characterise land, ocean or icy surfaces. Furthermore, a continuous monitoring can help to detect or prevent natural disasters such as tsunamis or earthquakes.

This Master Thesis has been performed at the RSLab, which is mainly dedicated to passive remote sensing. Many passive instruments have been developed which can be classified in two different groups: radiometers and reflectometers with signals of opportunity.

Radiometers are based on sensing the emissivity of bodies that are not at 0 K following Planck's law, which describes the amount of energy ideal blackbodies in thermal equilibrium emit due to being at a temperature above 0 K.

There are mainly two different group of radiometers, real aperture radiometers and synthetic aperture radiometers.

The other big field in passive remote sensing is reflectometry, which is based on sensing opportunity signals that are reflected over the surface. Opportunity signals are seen as signals that exist, but have not been transmitted by our system, such as, Global Navigation Satellite Systems (GNSS) signals. This means that with just a receiver, reflectometry techniques can be applied. In chapter 2 the two main techniques that the RSLab has been developing are detailed: the Delay-Doppler

Map (DDM) technique, and the Interference Pattern Technique (IPT). This Master Thesis is based on a particular application of the IPT.

1.2 PASSIVE ADVANCED UNIT (PAU) PROJECT

This project has been performed since 2005 at the RSLab. It is about monitoring the sea-state to correct the brightness temperature at L-Band. To do so, some instruments have been developed. Different concepts and approaches to GNSS-R techniques have appeared giving place to some Ph.D dissertations and journal articles. In this section some of the instruments developed are briefly commented.

- The SMIGOL-Reflectometer applies smartly the IPT technique to retrieve geophysical parameters over land, such as, soil moisture, vegetation height, and topography. Figure 1.1 shows the SMIGOL-Reflectometer in a field campaign.

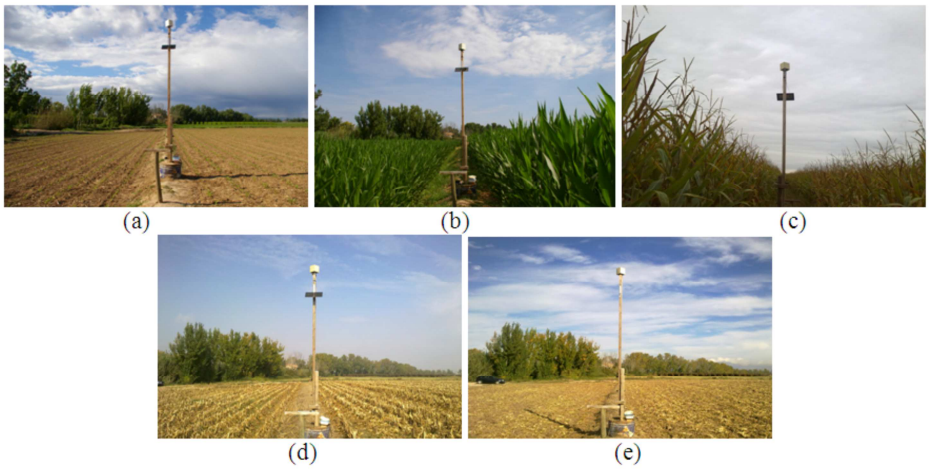

Figure 1.1: The SMIGOL-Reflectometer deployed in a field campaign [1].

- GriPAU is a combination of a radiometer and a reflectometer to measure the sea-state, using the DDM technique, and the Sea Surface Salinity (SSS), using radiometric observations at L-Band, and correcting the brightness temperature by using GNSS Observations. Figure 1.2 shows the instrument configuration where one antenna is pointing to the GNSS direct signal and the other two antennas are pointing to the sea surface. One is the radiometer antenna and the other one is collecting the GNSS reflected signal.

Figure 1.2: GriPAU at a field campaign [2].

- PAU-RAD is a real aperture radiometer working at 1.57542 GHz (GPS L1 Band) that uses digital beam forming (DBF) to create more than one beam that can be scanned electronically, enhancing the performance of conventional radiometers. It is shown in Figure 1.3.

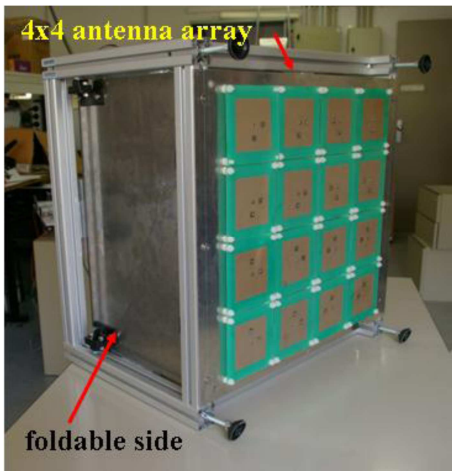

Figure 1.3: PAU-RAD [3].

- PAU-SA is a synthetic aperture radiometer working at L-Band. It is based on the SMOS principles and it has a Y-shaped antenna to obtain a hexagonal sampling of the spatial-frequency domain.

Figure 1.4: PAU-SA appearance and its structure remarking the Y-shaped antenna [4].

- MERITXELL (Multi-frequency Experimental Radiometer With Interference Tracking For Experiments Over Land And Littoral) is a classical multifrequency Dicke radiometer, that includes L-, S-, C- X-, K-, Ka-, and W-bands, plus a multi-spectral camera, a video camera, and a thermal infrared camera, in addition to the thermal infrared (PAU/IR) and GNSS-R reflectometer (PAU/GNSS-R) units. In Figure 1.5 the structure of the instrument is presented remarking each frequency channel in red.

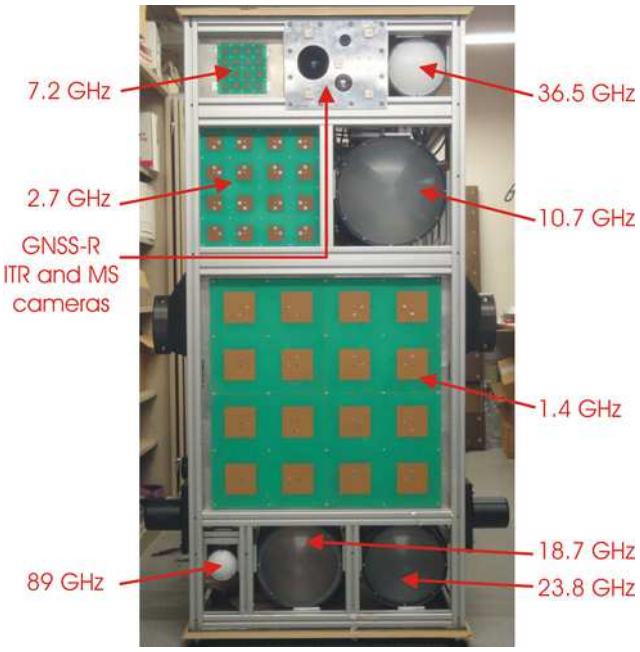

Figure 1.5: MERITXELL (Multi-frequency Experimental Radiometer With Interference Tracking For Experiments Over Land And Littoral) [5].

1.3 MOTIVATION

Using GNSS signals for Earth observation is a relatively new field of research since 1993 when Martin Neira proposed it to measure ocean mesoscale altimetry. Since that lots of different applications have been appearing such as:

- altimetry,
- wind-speed measurements,
- sea-state determination,
- soil moisture retrievals,
- vegetation height retrievals,
- topography retrievals,
- snow-depth retrievals,
- water-level monitoring, and

- others pending to be tested experimentally, as it will be explained in this Master Thesis.

Water level monitoring is a key element in the water cycle of the Earth. Some techniques already known have proved its validity. But, other techniques should be tested in order to give some alternatives or improve the performance of actual techniques.

During the final project degree the main goal was to help to enhance the performance of the SMIGOL-Reflectometer by adding extra complexity to improve the field of view of the instrument and also adding wireless capacity. At this point, the performance of the IPT technique over new scenarios can be tested.

Testing the IPT over dynamic scenarios, such as ocean, to monitor water-level is one the future lines of development shown by Dr. Nereida Rodríguez Álvarez in her Ph.D. Thesis dissertation.

1.4 MASTER THESIS GOAL

The main goal of this Master Thesis is to test the validity of the IPT technique over new scenarios. Experimental results have proven that the topography retrievals of the IPT technique can be applied also to monitor water level in reservoirs, where the scenario remains calm. So, the purpose is to see if it performs equally over dynamic scenarios.

For example, sea is a dynamic scenario that is important to characterise. Here mainly two different variables are going to affect the topography retrievals: sea-waves and sea-tides. Sea-waves are a very high-speed phenomena as compared to the SMIGOL-Reflectometer measurement time to retrieve surface's topography. Otherwise, sea-tides are a low-dynamic effect in the Mediterranean sea that can potentially be monitored by using the IPT technique.

Therefore, a site in the Mediterranean sea has been chosen to test the technique where ground-truth data is provided to compare the results retrieved.

As a secondary goal, it is important to analyse the instrument sensitivity to high-dynamic phenomena, such as the waves or the wind, because if sensibility is enough, sea surface roughness and wind speed could be retrieved.

Finally, the retrievals obtained over this Master Thesis are not based on a new theoretical model. Its goal is just to prove the feasibility of well-known algorithms in new scenarios and to see if there are other applications of the IPT technique. Therefore, the retrievals obtained will be given as an empirical formula showing that it is possible to estimate in new way geophysical parameters of interest for the scientific community.

1.5 MASTER THESIS STRUCTURE

This Master Thesis is structured in 6 different chapters:

- Chapter 1 – Introduction: It is an introductory chapter that talks about the research group where this master thesis has been developed and their main activities. The motivation and the goals of the master thesis are presented ending the chapter with the structure of the report.
- Chapter 2 – GNSS & GNSS-R: This chapter introduces the GNSS signals, especially the GPS ones because they have been used to develop all the IPT theory. Then, an overview of the GPS system is presented. To end the chapter the DDM and the IPT techniques are described, showing their main applications and all the mathematics needed to understand and develop them.
- Chapter 3 – Hardware description: This chapter makes an overview of the SMIGOL-Reflectometer, an instrument developed at the RSLab based on the IPT technique. Firstly, its main restrictions are presented to then comment deeply each instrument hardware block. To end the chapter a summary of all the blocks is given focusing on the most important aspects of the technology developed.
- Chapter 4 – IPT: In this chapter the main existing applications of the IPT technique are shown. After presenting all the mathematics, some simulations are shown to better understand the concept and then empirical results, which support theoretical developments, are given. A critical analysis of all the results is provided in each section.
- Chapter 5 – Field Experiment: This chapter presents the field experiment carried out to prove the validity of the IPT technique over a dynamic surface. A description of the field campaign is given. Ground-truth data is provided and the empirical results obtained are shown. A critical analysis of

the results obtained is provided showing the algorithm applied to process the data and justifying the approximations performed.

- Chapter 6 – Conclusions & Future Work: The main conclusions of this Master Thesis are commented along this chapter. It justifies why a new range of applications is opened by using the IPT. In this chapter my point of view where this technique can be applied is given.

Each chapter is ended with a summary emphasising the main points commented.

2 CHAPTER 2 GLOBAL NAVIGATION SATELLITE SYSTEMS

Since the starting of XX century the need of global navigation systems has increased year after year. In spite of the first applications of the systems were military-oriented now GPS navigators are available for civilian use.

Nowadays, the most known GNSS system is the Global Positioning System (GPS) which was designed by the U.S. Department of Defense to help their military forces to locate over the Earth. After that, some countries started to develop their own GNSS systems, such as Russia with GLONASS, China with COMPASS, and Europe with GALILEO, in order not to depending on U.S. decisions about GPS system [6].

A GNSS system is based on a constellation of satellites that gives coverage over a wide region. Depending on the region to be covered the constellation of satellites is designed in one way or another. For example, the GPS system has been designed to give worldwide coverage, and therefore the constellation of satellites shown in Figure 2.1 was designed. The GPS constellation needs 24 operative satellites to give fully operational capability (FOC) distributed in six different orbit planes with and inclination of 55º and a separation between them of 60º. However, it is formed by 30 satellites just to give some back-up support to the system. The satellites are working in a 12-hour orbital period at an altitude of 20.200 km.

Figure 2.1: GPS constellation.

There are different known applications for the GNSS systems, some of them are presented in the following lines. The first three applications presented are the most used civilian applications [6]:

- Personal navigation: To locate ourselves over the world.
- Aviation application: En-route and landing applications, only as a supporting system.
- Automotive applications: Give instructions to drivers to go from one place to another.
- Weak signal navigation: Indoor navigation mainly.
- Marine applications: Navigate over the sea.
- Space applications: Mainly to locate LEO satellites, but GEO satellites as well.
- Agriculture, forestry, and natural resources applications: Geological monitoring, forest management, mining and oil exploration.
- Geodesy and surveying: Monitoring the movements of the Earth's crustal plates or ice shelves.
- Scientific applications: Mainly remote sensing applications, as it will be seen along this report.

This chapter is going to be mostly concentrated in GPS system because it is the system that has been used along all the experiments presented, but everything can be extended to other GNSS systems with the only need of changing the GNSS receiver.

2.1 GPS SIGNALS

GPS signals are transmitted at different frequencies in L-Band. Table 2.1 shows a brief summary of all the bands used and their purpose.

Table 2.1: GPS Signals Band Classification.

Band	Frequency (GHz)	Description
L1	1.57542	Coarse-acquisition (C/A) and encrypted precision P(Y) codes, plus the L1 civilian (L1C) and military (M) codes on future Block III satellites.
L2	1.2276	P(Y) code, plus the (L2C) and military codes on the Block IIR-M and newer satellites.
L3	1.38105	Used for nuclear detonation (NUDET) detection.
L4	1.379913	Being studied for additional ionospheric correction.
L5	1.17645	Proposed for use as a civilian safety-of-life (SoL) signal.

To be more understandable with all the signal descriptions, just the L1 and the L2 bands will be taken into account along the following explanations and equations, but a similar model can be applied for all bands. GPS signals are formed mainly by three different elements, the carrier frequency, the navigation data, and the spreading sequence. In a general way, a GPS signal is expressed by eqn. (2.1).

$$s^i(t) = \sqrt{2 \cdot P_c} \cdot \left(C^i(t) \oplus D^i(t)\right) \cdot \cos(2 \cdot pi \cdot f_{L1} t) + \sqrt{2 \cdot P_{PL1}} \cdot \left(P^i(t) \oplus D^i(t)\right) \cdot \sin(2 \cdot pi \cdot f_{L1} t) + \sqrt{2 \cdot P_{PL2}} \cdot \left(P^i(t) \oplus D^i(t)\right) \cdot \sin(2 \cdot pi \cdot f_{L2} t) \quad (2.1)$$

where:

- P_c, P_{PL1}, P_{PL2}, are the powers related to each signal band in baseband,
- $C^i(t)$: Civilian spreading sequence (C/A code),
- $D^i(t)$: Navigation data,
- $P^i(t)$: Precision or military spreading sequence (P-code),
- f_{L1}, f_{L2}: The carrier frequencies shown in Table 2.1, and
- i: The number of satellite chosen.

Figure 2.2 shows the generation scheme of GPS signals.

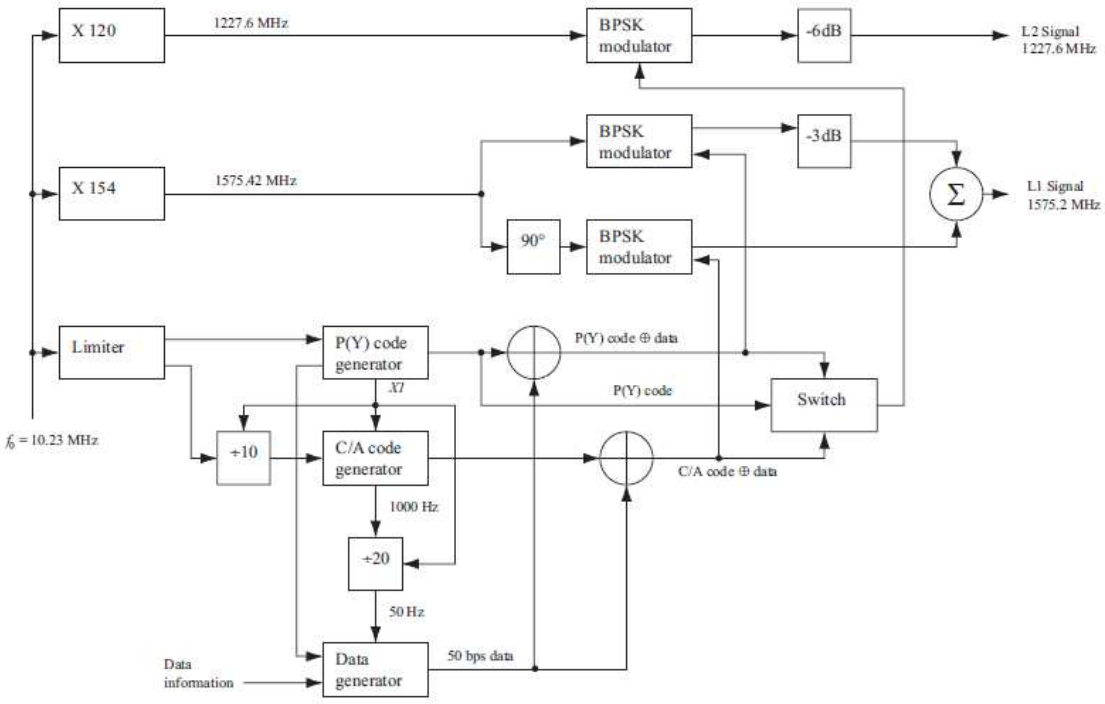

Figure 2.2: Generation scheme of GPS signals [7].

As seen in Figure 2.2, everything begins from the frequency f_0 = 10.23 MHz. From here, the L1 and L2 carriers are generated and it is also the generated the chipping

rate of P-code. Then, with dividers the chipping rates of C/A code, and the navigation data are obtained. As the C/A code is the only open code, it is the one that is going to be explained in this chapter as well as the GPS navigation message structure. Figure 2.3 shows a clearer representation of the GPS signal where it can be clearly seen the C/A code period (1 ms) and the data rate (50 bps).

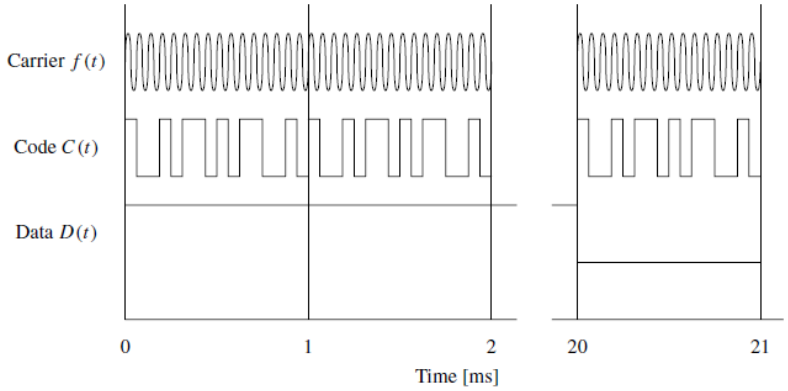

Figure 2.3: GPS signal as a function of time [7].

2.1.1 C/A CODE

The C/A code is based on a smart combination of pseudo-random noise (PRN) signals of maximum length (2^N-1), which can be created using linear feedback shift registers (LFSR), being N=10. This leads to codes of 1023 chips where the chip period is around 977.5 ns (1ms /1023). This smart combination of PRN signals results in what is known as Gold codes which are widely used in code division multiplexing access (CDMA), and direct sequence spread spectrum (DSSS) systems.

In GPS systems, PRN signals are obtained from LFSR registers that can be defined by the following polynomials:

$$f(x) = 1 + x^3 + x^{10} \tag{2.2}$$

$$f(x) = 1 + x^2 + x^3 + x^6 + x^8 + x^9 + x^{10} \tag{2.3}$$

Then, by applying the algorithm shown in Figure 2.4, the gold sequences are obtained.

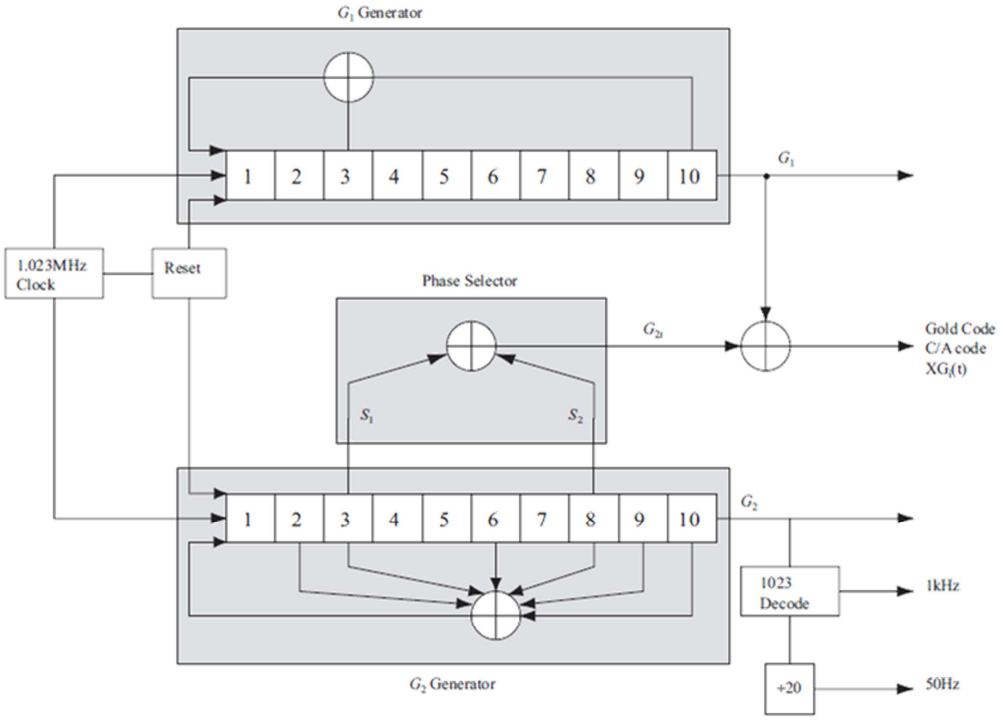

Figure 2.4: Gold sequence generation algorithm [7].

But why GPS Signals are based on Gold Sequences? The reason is simple; they want to take advantage of their correlation properties:

$$r_{ik}(m) = \sum_{l=0}^{1022} C^i(l) \cdot C^k(l+m) \approx 0 \quad for\ all\ m\ and\ k \neq i. \tag{2.4}$$

$$r_{kk}(m) = \sum_{l=0}^{1022} C^k(l) \cdot C^k(l+m) \approx 0 \ for\ all\ m \geq 1. \tag{2.5}$$

With these properties it is very easy to identify to which satellites the receivers are locked and also to obtain the resolution expected. In total, there are only 36 different sequences of 1023 chips that satisfy the correlation properties expressed in eqns. (2.4) and (2.5).

Gold codes are signals modulated in binary phase shift keying (BPSK), which is why their values are +1 or -1 (Figure 2.5, subfigures (a) and (b)), whose autocorrelation function (ACF) is very small in spite of one point that is maximum (1023, Figure 2.5 (c)) and the cross correlation function between different codes is very small (Figure 2.5 (d)). In Figure 2.5 there have been only used the first two Gold codes, but the others are similar.

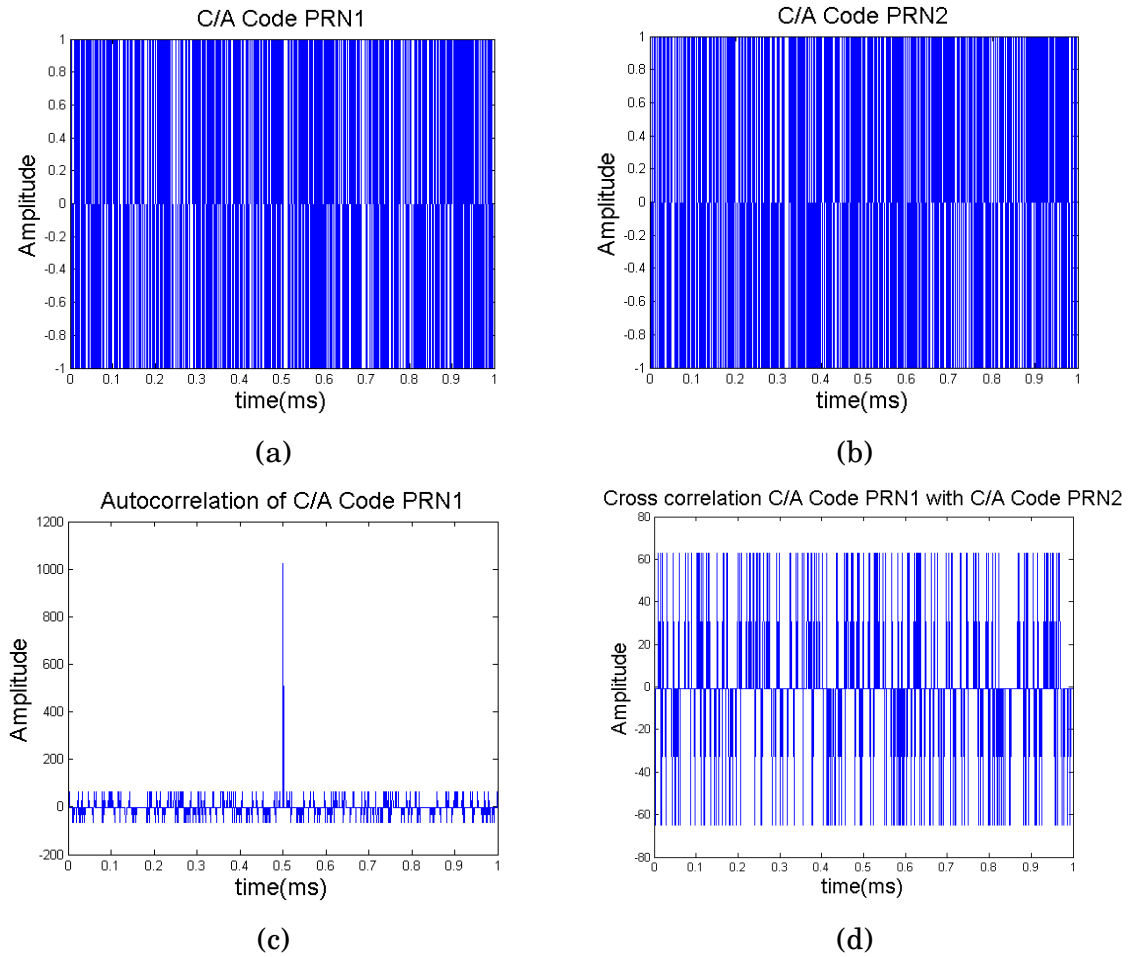

Figure 2.5: Summary of Gold codes properties.

Finally, one aspect must be taken into account: the Doppler shift that the signal will suffer is mainly caused by the movement of the satellites. This may cause misalignment between the received signal and the local replica of the code generated in the receiver.

2.1.2 NAVIGATION DATA

Navigation data are the signals encoded at L1 band that allow a GPS receiver to estimate the position of the GPS satellites they are locked and consequently establish correctly the receiver's position on Earth. Its basic structure is a packet of 1500 bits containing 5 subframes of 300 bits that are formed by 10 words of 30 bits each one. The transmission rate of the Navigation data is 50 bps which means that the whole message lasts for 12.5 minutes. Figure 2.6 shows graphically what has been explained in this paragraph.

The Navigation message is formed by different elements:

- TLM: Contains a preamble used for synchronisation.

- HOW: Contains the *time of the week* parameter.
- Satellite clock and health data: All clock information and confirmation of reliable data.
- Satellite Ephemeris Data: Contains Ephemeris data which is data related to the satellite orbit to estimate its position.
- Support data (Almanac): Ephemeris data of the other satellites with less precision to accelerate the position estimation algorithm.
- Ionospheric corrections.

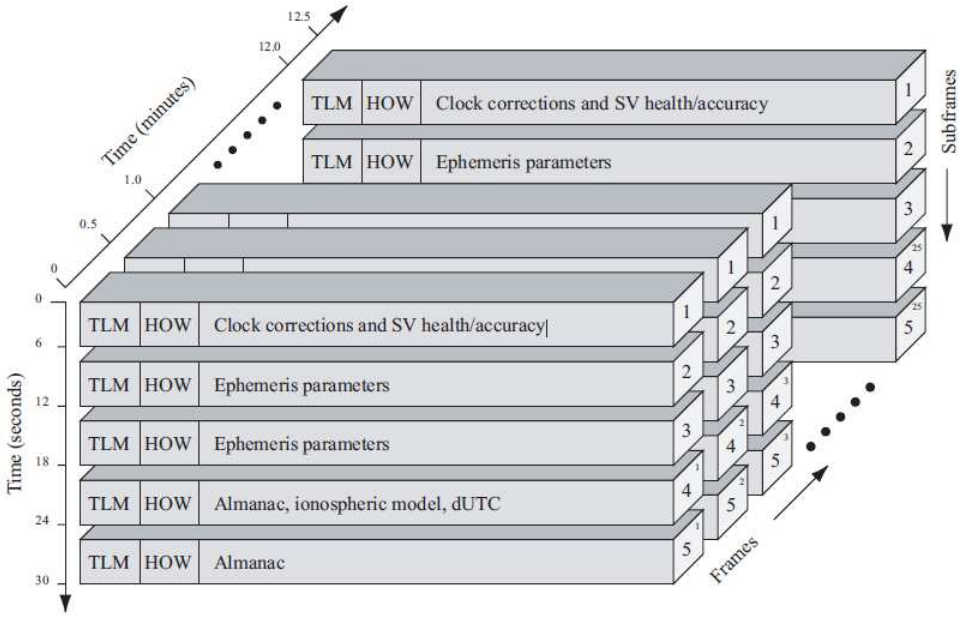

Figure 2.6: Navigation message structure [7].

2.1.3 SPECTRUM ANALYSIS OF GPS SIGNALS

GPS signals are obtained by multiplying different pulses with different lengths, as seen in Figure 2.3 and eqn. 2.1. So, another way to express the GPS signal without considering the carrier frequency is shown in eqn. (2.6):

$$s(t) = \left(\sum_{m=1}^{20} \left(\sum_{n=0}^{1023} C(n) \cdot \prod\left(\frac{\left(t - n \cdot \frac{T_{chip}}{2}\right)}{T_{chip}} \right) \right) \cdot \prod\left(\frac{t - m\frac{T_{ca}}{2}}{T_{ca}} \right) \right) \cdot \sum_{k-\infty}^{+\infty} D(k) \cdot \prod\left(\frac{\left(t - k \cdot \frac{T_{data}}{2}\right)}{T_{data}} \right) \quad (2.6)$$

where:

- $\prod\left(\frac{t-Tp/2}{Tp}\right)$ is the pulse function with T_p duration,

- T_{chip} = 1ms/1023 ≈ 0.97 μs,
- T_{data} = 20 ms,
- T_{ca}=1 ms,
- $C(n)$: C/A code, and
- $D(k)$: Navigation data

If the Fourier transform is applied, the result obtained is proportional to the convolution of the Fourier transform of the pulse T_{chip} with the Fourier transform of the pulse T_{ca} sampled in frequency at the sampling rate of the Fourier transform of the navigation data. In other words:

$$F\{s(t)\} \propto F\left\{\prod\left(\frac{\left(t - n \cdot \frac{T_{chip}}{2}\right)}{T_{chip}}\right)\right\} * F\left\{\prod\left(\frac{t - m\frac{T_{ca}}{2}}{T_{ca}}\right)\right\} \quad (2.7)$$

Then, with the help of Matlab the spectrum can be computed. Figure 2.7 shows the GPS signal spectrum for satellite number 1. Here, it can be seen that the whole bandwidth of the GPS signal is determined by the chip duration. Then, the effect of the convolution cannot be seen due to resolution, but the sampling effect is clearly identified.

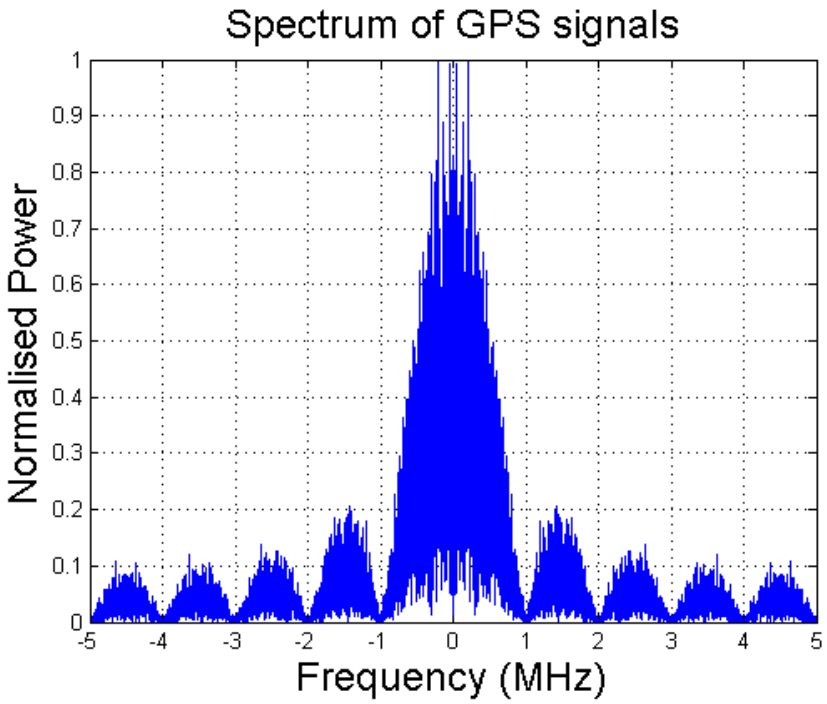

Figure 2.7: Spectrum of the GPS C/A signals.

Just by looking at Figure 2.7 we can understand why the GPS signals are called spread spectrum signals. The bandwidth of a signal transmitted at 50 bps should be just 100 Hz whereas GPS signals have 2 MHz bandwidth (defined between zeros).

2.2 POSITION ESTIMATION

There are different configurations that have been developed to enhance the precision of GPS systems, but in this part of the report just the general acquisition algorithm will be commented. The starting point is eqn. (2.8) [6].

$$\rho^i(t) = r^i(t, t-\tau) + c \cdot \left[\delta t_u(t) - \delta t^i(t-\tau)\right] + I^i(t) + T^i(t) + e^i(t) \tag{2.8}$$

where:

- i: Individual identifier for the transmitting satellite,
- $\rho^i(t)$: Pseudo-range observed,
- t: Time of reception,
- $r^i(t, t-\tau)$: True geometric range between the satellite and the receiver,
- τ: Delay of the signal,
- c: Speed of the light in the vacuum,
- $\delta t_u(t)$: Receiver clock offset from GPS time,
- $\delta t^i(t-\tau)$: Satellite clock offset,
- $I^i(t)$: Ionospheric propagation delay,
- $T^i(t)$: Tropospheric propagation delay, and
- $e^i(t)$: Miscellaneous errors (noise, multipath, uncertainty in satellite position, etc.).

Note that nearly all the elements depend on the satellite despite of the receiver clock offset. Therefore, eqn. (2.8) can be expressed as eqn. (2.9) just by arranging all the error terms.

$$\rho_c^i = r^i + c \cdot \delta t_u(t) + \tilde{e}_T^i, \tag{2.9}$$

where:

$$r^i = \sqrt{(x^i - x) + (y^i - y) + (z^i - z)} = \left\|\boldsymbol{x^i} - \boldsymbol{x_u}\right\|, \tag{2.10}$$

Being $\boldsymbol{x^i}$ the satellite position in (x, y, z) coordinates, and $\boldsymbol{x_u}$ the receiver position in the same coordinates, taking into account that for GPS, the WGS-84 reference ellipsoid is used. Then, eqn. (2.11) is obtained:

$$\rho_c^i = \left\|\boldsymbol{x^i} - \boldsymbol{x_u}\right\| + c \cdot \delta t_u(t) + \tilde{e}_T^i \tag{2.11}$$

At this point, a convergence algorithm is applied following next equations:

$$\delta\rho^i = \rho_c^i - \rho_0^i, \tag{2.12}$$

$$\delta\rho^i = \left\|\boldsymbol{x^i} - \boldsymbol{x_u}\right\| + b + \tilde{e}_T^i - \left[\left\|\boldsymbol{x^i} - \boldsymbol{x_0}\right\| + b_0\right], \text{ and} \tag{2.13}$$

$$\delta\rho^i = -\frac{\boldsymbol{x^i} - \boldsymbol{x_0}}{\left\|\boldsymbol{x^k} - \boldsymbol{x_u}\right\|}\delta\boldsymbol{x} + \delta b + \tilde{e}_T^i = -L_{unit}^i \cdot \delta\boldsymbol{x} + \delta\boldsymbol{x} + \tilde{e}_T^i. \tag{2.14}$$

So, the process is to select a point on the Earth, compute the theoretical pseudo-ranges to each satellite that has been seen by the receiver and then compare them with the measured pseudo-ranges. Then, the estimated point is smartly changed until the RMSE solution is found, which means that the position has been obtained.

However, the previous equations can be expressed in a matrix notation which would help the reader to follow the explanation.

$$\delta\boldsymbol{\rho} = \begin{bmatrix}\delta\rho^1 \\ \delta\rho^2 \\ \cdots \\ \delta\rho^N\end{bmatrix} = \begin{bmatrix}-\boldsymbol{L}_{unit}^{1\ T} & 1 \\ -\boldsymbol{L}_{unit}^{2\ T} & 1 \\ \cdots & 1 \\ -\boldsymbol{L}_{unit}^{N\ T} & 1\end{bmatrix} \cdot \begin{bmatrix}\delta\boldsymbol{x} \\ \delta b\end{bmatrix} + \begin{bmatrix}\tilde{e}_T^1 \\ \tilde{e}_T^2 \\ \cdots \\ \tilde{e}_T^N\end{bmatrix}, \tag{2.15}$$

Where, $\boldsymbol{G}$ is the geometric matrix:

$$\boldsymbol{G} = \begin{bmatrix}-\boldsymbol{L}_{unit}^{1\ T} & 1 \\ -\boldsymbol{L}_{unit}^{2\ T} & 1 \\ \cdots & 1 \\ -\boldsymbol{L}_{unit}^{N\ T} & 1\end{bmatrix}. \tag{2.16}$$

Then, without considering the satellite errors the position can be estimated by means of eqn. (2.17):

$$\begin{bmatrix}\delta\boldsymbol{x} \\ \delta b\end{bmatrix} = (\boldsymbol{G}^T\boldsymbol{G})^{-1} \cdot \boldsymbol{G}^T \cdot \delta\boldsymbol{\rho}, \tag{2.17}$$

$$\boldsymbol{x}_{0|New} = \boldsymbol{x}_{0|Old} + \delta\boldsymbol{x} \qquad b = \delta b. \tag{2.18}$$

Figure 2.8 tries to summarise all the equations presented in section 2.2.

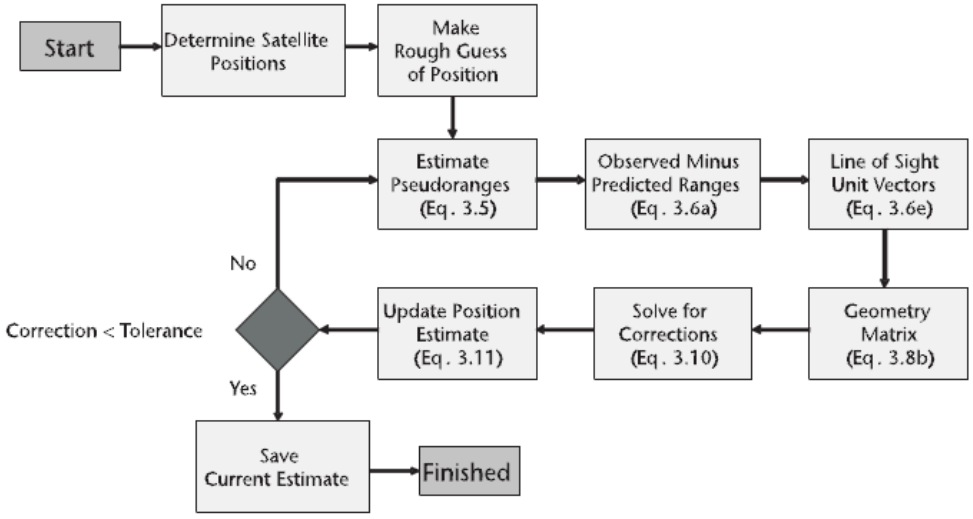

Figure 2.8: Convergence algorithm to obtain GPS position [7].

2.3 PRECISION DEFINITION

The precision of the GPS solution is defined by the $\boldsymbol{H}$ matrix. The $\boldsymbol{H}$ matrix is defined as:

$$\boldsymbol{H} = (\boldsymbol{G}^T\boldsymbol{G})^{-1} = \begin{bmatrix} H_{11} & - & - & - \\ - & H_{22} & - & - \\ - & - & H_{33} & - \\ - & - & - & H_{44} \end{bmatrix}, \tag{2.19}$$

where:

- $\sqrt{H_{11}}$: East Dilution Of Precision (EDOP).
- $\sqrt{H_{22}}$: North Dilution Of Precision (NDOP).
- $\sqrt{H_{33}}$: Vertical Dilution Of Precision (VDOP).
- $\sqrt{H_{44}}$: Time Dilution Of Precision (TDOP).
- $\sqrt{H_{11} + H_{22}}$: Horizontal Dilution Of Precision (HDOP).
- $\sqrt{H_{11} + H_{22} + H_{33}}$: Positioning Dilution Of Precision (PDOP).
- $\sqrt{H_{11} + H_{22} + H_{33} + H_{44}}$: Geometric Dilution Of Precision (GDOP).

Another way to look at $\boldsymbol{H}$ is to associate each term to a coordinate as:

- H_{11} can be associated to the X-coordinate,
- H_{22} can be associated to the Y-coordinate,
- H_{33} can be associated to the Z-coordinate, and

- H_{44} can be associated to time synchronisation errors.

This is why it is well-known that a GPS receiver needs at least 4 satellites in view to estimate the position on the Earth.

2.4 GLOBAL NAVIGATION SATELLITE SYSTEMS-REFLECTOMETRY (GNSS-R)

Remote sensing using GNSS signals can be seen an extension of RADAR remote sensing. In RADAR systems there is a transmitter and a receiver, but in GNSS-R, GNSS signals are taken as opportunity signals, and a GNSS-R system just needs a receiver or a set of receivers to perform correctly.

The main idea behind any GNSS-R system is that GNSS signals are scattered by the surface where they are reflected hiding in them information about this surface. Different ways to configure the system and extract the information hidden is what is known as GNSS-R techniques. In this report two of them are going to be presented: the Delay Doppler Map technique (DDM), and the Interference Pattern Technique (IPT).

The first proposal of using GNSS-R techniques to measure mesoscale altimetry over Ocean was made by Martín-Neira in 1993, [8]. Since then, a wide range of applications has appeared and new ones are under research. Now, some applications are presented:

- Ocean altimetry measurements [8],
- Sea surface Roughness [9],
- Sea ice sensing [10],
- Wind speed [11],
- Surface soil moisture content [1],
- Vegetation height retrievals [1],
- Topography retrievals [1],
- Water level measurements [1],
- Sea-state [2],
- Ocean salinity [2].

Now the DDM and IPT techniques are presented.

2.4.1 DELAY-DOPPLER MAP (DDM)

The geometry of a GNSS-R system can be modelled as shown in Figure 2.9. This figure means that GNSS signals are reflected over a scattering surface, called glistering zone, whose area depends on the receiver's height and surface roughness, and then reaches the receiver. Along the glistering zone there is a point of specular reflection, which is the point that minimises the distance Transmitter-Earth-Receiver. This point is used for altimetry measurements, and as a reference for the Doppler frequency shift estimation.

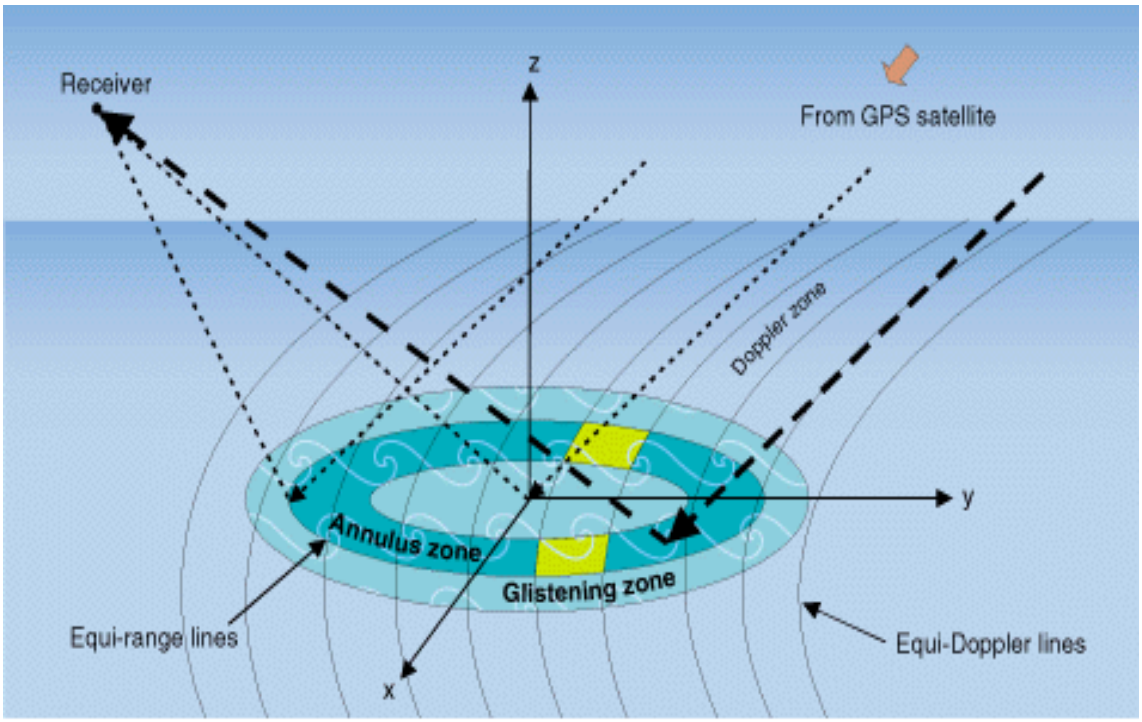

Figure 2.9: GNSS-R geometry [6].

The glistering zone contributes to the received signal with a different delay and a different Doppler shift from the specular reflection point signal. This allows plotting the so called DDM.

Furthermore, in Figure 2.9 there are also plotted some curves called Iso-Doppler lines, which are points of the glistering zone where the Doppler frequency shift is the same, and ellipses called Iso-delay lines, which refer to signals reflecting in some specular point that when reaching the sensor they have travelled the same distance (and therefore have experienced the same delay).

Once at this point, two questions quickly arise. What is a DDM? How can we obtain a DDM?

The first step in producing the DDM is de-spreading or cross-correlating of the recorded signal's I and Q data with a replica of the PRN code of the available GPS satellite for a set of different time lags and carrier frequency offsets, which means different Doppler shifts. This cross-correlation is performed over a coherent integration time, until the coherence of the signal is preserved. Now, eqn. (2.20) shows the DDM equation.

$$\langle |Y(\tau, fd)|^2 \rangle = \langle \left| \int_0^{T_i} s(t) \cdot a(t+\tau) \cdot e^{-j2\pi(f_{L1}+f_d)t} dt \right|^2 \rangle, \tag{2.20}$$

where [2]:

- $s(t)$ is the received signal,
- $a(t)$ is the local replica of the GPS C/A Code,
- (τ, fd) are the Delay-Doppler coordinates,
- f_{L1} carrier frequency of L1 Band, and
- T_i is the coherent integration time.

Incoherent integration can be applied to the DDM during $N \cdot T_i$, which physically means averaging to reduce the noise effect on the DDM, eqn. 2.21.

$$\overline{|Y(\tau, fd)|^2} = \frac{1}{N} \cdot \sum_{n=1}^{N} |Y(\tau, fd)|^2 \tag{2.21}$$

This mathematical function (DDM) described by eqns. (2.20) and (2.21) is very similar to the Woodward Ambiguity Function (WAF) studied for long time in RADAR field and looks like Figure 2.10.

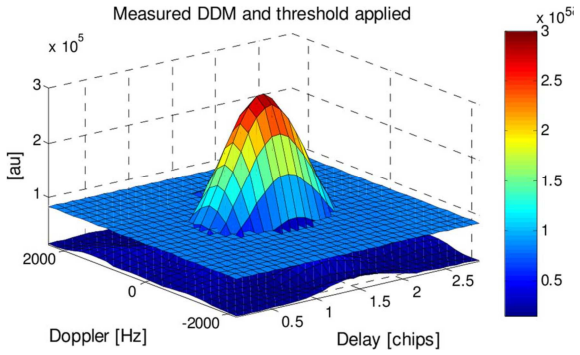

Figure 2.10: DDM representation in 3-D [2].

Eqn. (2.22) presents the complex theoretical model of the DDM that would be retrieved from the ocean surface. This model was proposed by Zavorotny and

Voronovich in 2000, it shows all the factors that must be taken into account when performing and understanding the DDM technique.

$$\langle |Y(\delta\tau, \delta f_d)|^2 \rangle = \frac{T_i^2 P_T G_T L_{atm} \lambda^2}{(4\pi)^3} \iint \frac{G_R(\vec{\rho}) \Lambda^2\left(\delta\tau - \tau(\vec{\rho})\right) \left|S\left(\delta f_d - f_d(\vec{\rho})\right)\right|^2}{R_0^2(\vec{\rho}) \cdot R^2(\vec{\rho})} \pi |\Gamma|^2 \cdot \frac{q^4(\vec{\rho})}{q_z^4(\vec{\rho})} \cdot P_{\vec{v}}\left(-\frac{\vec{q}_\perp}{q_z}\right) \cdot d^2\rho \quad (2.22)$$

Where:

- T_i is the coherent integration time,
- $P_T G_T$ is the transmitter effective isotropic radiated power (EIRP),
- L_{atm} is the atmospheric attenuation,
- G_R is the receiver's antenna gain,
- Λ is the PRN code correlation function defined as $\Lambda(\tau) = 1 - |\tau|/\tau_c$ if $|\tau|/\tau_c$, and 0 elsewhere, with τ_c being the length of a chip of the C/A code defined as 1 ms/1023;
- $S(f)$ is the sinc-shaped function defined as $S(f) = sin(\pi f)/\pi f$,
- $\tau(\vec{\rho})$ and $f_d(\vec{\rho})$, are, respectively, the time delay, and the Doppler frequency shift for the signal traveling between the transmitter, arbitrary surface point $\vec{\rho}$, and the receiver, relatively to the same values associated with the nominal specular point on the mean ocean surface. The shapes of the iso-delay annulus zones described by the equation $\tau(\vec{\rho}) = \text{const}$ and the equi-Doppler zones described by equation $f_d(\vec{\rho}) = \text{const}$ are shown schematically in Figure 2.9,
- R_0 is the distance from the GPS transmitter to the scattering point $\vec{\rho}$,
- R is the distance from $\vec{\rho}$ to the receiver,
- Γ is the Fresnel reflection coefficient for the ocean surface,
- $\vec{q}$ is the scattering vector which depends on $\vec{\rho}$ and is defined as $\vec{q} = k \cdot (\hat{n}_s - \hat{n}_i) = \vec{q}_\perp + q_z \hat{z}$ with $\hat{n}_i$ and $\hat{n}_s$ being unit vectors, respectively, of the incident and scattered waves, with $k = 2\pi/\lambda$ and $q = |\vec{q}|$; and,

- $P_{\vec{v}}$ denotes here the probability density function (PDF) of the ocean surface slopes $\vec{v}$.

A graphical representation is shown in Figure 2.11 to better understand the meaning of a DDM over the ocean surface. In both subfigures, (a) and (b), all the previous mentioned parameters can be observed such as the specular reflection point and the glistering zone until the power of the DDM falls below a threshold.

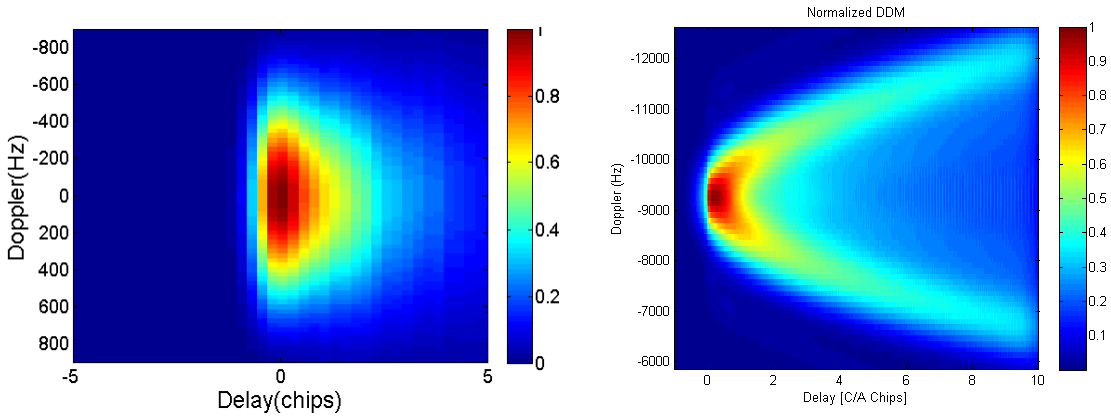

(a) (b)

Figure 2.11: (a), Measured normalised DDM for PRN 9 from 386 m height using the geometry information at UTC 10:06 plotted in a linear units, (b), simulated normalised DDM seen from space-borne remarking the shape due to having higher dopplers and delays [12].

The last point remaining is to understand the results of a DDM to apply it for retrieving wind speed, oil slicks detection, sea surface roughness and a wide range of environmental applications that can be found in the references.

2.4.2 INTERFERENCE PATTERN TECHNIQUE (IPT)

This technique is a particular technique used in GNSS-R well-suited for ground based instruments. It is based on the electromagnetic addition (interference) of direct and reflected GNSS signals, so it relies on the coherent addition of direct and reflected waves as shown in Figure 2.12. The result obtained is a constructive/destructive interference between both waves.

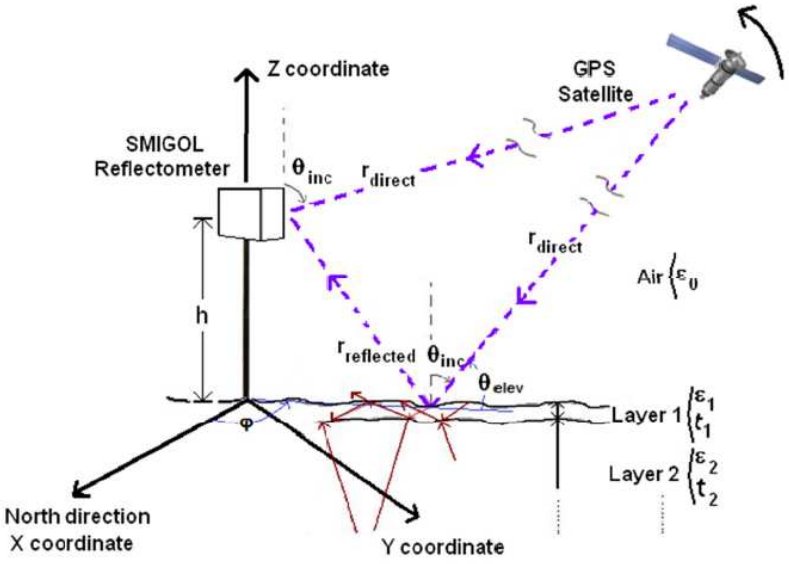

Figure 2.12: Geometry of the IPT technique [1].

As it can be seen in Figure 2.12 signals emitted by the satellite reach the sensor at different times, but the delay between them must be well below the chip period or coherence time (0.97 μs), which limits the maximum height of the ground based instrument. As the incidence angle in the antenna receiver is the same for both waves, which can be seen just by analysing the geometry of the problem (paraxial approximation), the main restriction of the technique is having an antenna pointing to the horizon with a symmetric pattern to simplify the modelling of the interference pattern. This means the system is self-calibrated and the only difference between direct and reflected waves remains just in the interaction of the reflected wave with the surface. Interference patterns obtained look like the one shown in Figure 2.13 where a theoretical interference pattern for horizontal polarisation (H-Pol) and vertical polarisation (V-Pol) has been shown as a function of the elevation angle.

There are two main reasons for using linear polarization instead of the right hand circular polarization (RHCP), the one that is transmitted by GPS satellites, or left hand circular polarization (LHCP), the theoretical polarization for the reflected GPS wave.

- If using linear polarization the same antenna can be used for obtaining direct and reflected signals whereas for obtaining RHCP and LHCP it is preferable to use different antennas.

- Linear polarisation is more sensible to the interaction with the surface than circular polarization as it can be seen in Figure 2.13 for V-Pol that there is a point of minimum amplitude called notch due to the Brewster angle. Consequently, it is assured that the optimum polarization to retrieve geophysical parameters due to its sensibility to the changes in the dielectric constant is linear V-Pol.

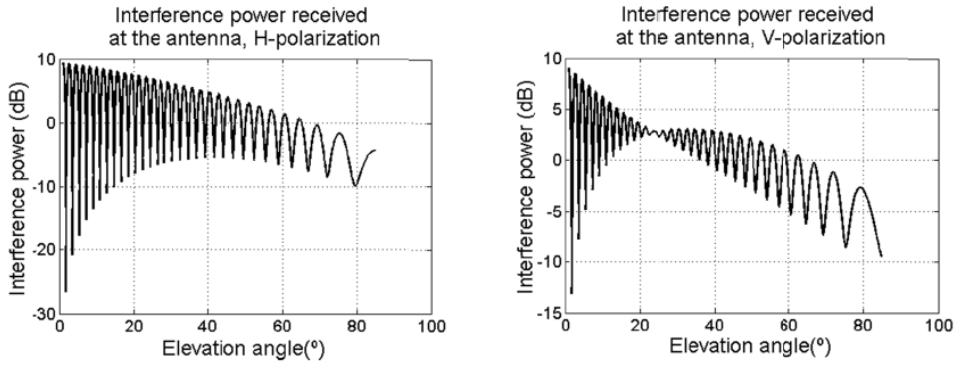

Figure 2.13: Interference patterns obtained for H-Pol and V-Pol [1].

Therefore, the power reaching the antenna can be modelled by eqn. (2.23).

$$P \propto |E_i + E_r|^2 \equiv \left| E_{0i} \cdot F_i(\theta)^{\frac{1}{2}} \cdot e^{j\varphi_i} + E_{0i} \cdot F_r(\theta)^{\frac{1}{2}} \cdot R(\theta, \varepsilon_r) \cdot e^{j\varphi_r} \right|^2 = E_{0i} \cdot F_n(\theta) \cdot \left| 1 + R(\theta, \varepsilon_r) \cdot e^{j\emptyset} \right|^2 , \quad (2.23)$$

where:

- E_{0i} is the amplitude of the direct incident wave,
- $F_i(\theta)^{\frac{1}{2}}$ the contribution of antenna pattern to the direct wave,
- $F_r(\theta)^{\frac{1}{2}}$ the contribution of antenna pattern to the reflected wave,
- $e^{j\varphi_i}$, $e^{j\varphi_r}$ the relative phase of direct and reflected wave respectively,
- θ is the elevation angle,
- $R(\theta, \varepsilon_r)$ the field reflection coefficient of the surface, or Fresnel reflection coefficient, which depends on θ and ε_r (the dielectric constant of the surface),
- $F_{n[dB]}(\theta) \cong -12 \left(\frac{90 - \theta_{inc}}{\Delta\theta_{-3dB}} \right)^2$ is the modeled antenna pattern, and
- $\emptyset = \varphi_i - \varphi_r = \frac{4\pi}{\lambda} \cdot h \cdot \sin(\theta)$ the difference in phase between direct and reflected signals.

If eqn. (2.23) is expressed in dB the term $E_{0i} \cdot F_n(\theta)$ can be seen as a modulation factor, allowing us to determine $R(\theta, \varepsilon_r)$, which hides geophysical parameters of the reflected surface.

Considering just a two-layer model, which means that direct signal comes from free space and reaches just a layer of soil, the Fresnel reflection coefficients obtained are the following.

$$r_H = \frac{n_i \cdot \cos(\theta_{inc}) - n_{i+1} \cdot \cos(\theta_{trans})}{n_i \cdot \cos(\theta_{inc}) + n_{i+1} \cdot \cos(\theta_{trans})}, \tag{2.24}$$

$$r_V = \frac{n_{i+1} \cdot \cos(\theta_{inc}) - n_i \cdot \cos(\theta_{trans})}{n_{i+1} \cdot \cos(\theta_{inc}) + n_i \cdot \cos(\theta_{trans})}, \tag{2.25}$$

where:

- H stands for horizontal polarization whereas V for vertical polarization,
- $n_i = \sqrt{\varepsilon_{r_i} \cdot \mu_{r_i}}$ is the refraction index of the propagating layer, generally air,
- $n_{i+1} = \sqrt{\varepsilon_{r_{i+1}} \cdot \mu_{r_{i+1}}}$ is the refraction index of the reflecting surface,
- θ_{inc} is the incidence angle and θ_{trans} is the transmitted angle.

The relation between incidence and transmitted angle can be easily obtained by Snell's law, therefore eqns. (2.24) and (2.25) become (2.26) and (2.27) respectively.

$$r_{H_{i,i+1}} = \frac{\sqrt{\varepsilon_{r_i} - \varepsilon_{r_i} \cdot sin^2(\theta_{inc})} - \sqrt{\varepsilon_{r_{i+1}} - \varepsilon_{r_i} \cdot sin^2(\theta_{inc})}}{\sqrt{\varepsilon_{r_i} - \varepsilon_{r_i} \cdot sin^2(\theta_{inc})} + \sqrt{\varepsilon_{r_{i+1}} - \varepsilon_{r_i} \cdot sin^2(\theta_{inc})}}, \tag{2.26}$$

$$r_{V_{i,i+1}} = \frac{\varepsilon_{r_{i+1}} \cdot \sqrt{\varepsilon_{r_i} - \varepsilon_{r_i} \cdot sin^2(\theta_{inc})} - \varepsilon_{r_i} \cdot \sqrt{\varepsilon_{r_{i+1}} - \varepsilon_{r_i} \cdot sin^2(\theta_{inc})}}{\varepsilon_{r_{i+1}} \cdot \sqrt{\varepsilon_{r_i} - \varepsilon_{r_i} \cdot sin^2(\theta_{inc})} + \varepsilon_{r_i} \cdot \sqrt{\varepsilon_{r_{i+1}} - \varepsilon_{r_i} \cdot sin^2(\theta_{inc})}}. \tag{2.27}$$

These equations are computed in the interface between both media and the reflection coefficient can be obtained. This model can be extrapolated to an N-surface layer model. For simplicity aspects, in this report is just shown the result obtained for a 3-layer model is presented in eqn. (2.28).

$$R = e^{-\left(\frac{4 \cdot \pi \cdot \sigma}{\lambda}\right)^2} \cdot \frac{r_{i,i+1} + r_{i+1,i+2} \cdot e^S \cdot e^{j2\psi}}{1 + r_{i+1,i+2} \cdot r_{i+1,i+2} \cdot e^S \cdot e^{j2\psi}}, \tag{2.28}$$

where:

- σ is the soil surface roughness,

- $\psi = \frac{2\pi}{\lambda} \cdot t_{i+1} \cdot \sqrt{\varepsilon_{r_{i+1}} - \varepsilon_{r_i} \cdot sin^2(\theta_{inc})}$ where t_{i+1} is the height of the $i+1$ layer and,
- $S = -8 \cdot \left(\frac{\pi \cdot \sigma_l}{\lambda} \sqrt{\varepsilon_{r_{i+1}} - \varepsilon_{r_i} \cdot sin^2(\theta_{inc})}\right)^2$ models the roughness of the interaction.

As seen in Figure 2.13, the notch that appeared for V-Pol is related to the Brewster angle eqn. (2.29), which by definition is the point of minimum reflection coefficient at V-Pol.

$$\theta_B = \arctan\left(\frac{n_2}{n_1}\right) = \arctan\left(\sqrt{\frac{\varepsilon_{r_2}}{\varepsilon_{r_1}}}\right) \tag{2.29}$$

By analyzing the whole interference pattern other geophysical parameter can be retrieved as it will be explained in Chapter 4 with some existing applications such as determination of soil moisture, vegetation height, topography estimation, and water-level monitoring. Finally, this technique is the basis of this Master Thesis, in which new applications will be explored.

2.5 SUMMARY

Along this chapter GNSS systems have been introduced and their main characteristics have been shown.

GPS signals are made from gold sequences, which are direct sequence spread spectrum signals with special correlation properties that enhance the performance of the system. The public GPS service signals contains the C/A code that has a period of 1 ms and the navigation data that is transmitted at 50 bps. GPS signals fall below noise level, but due to correlation properties and repetition of C/A code the signal can be recovered.

The retrieval position algorithm has been briefly discussed to present the errors affecting the GPS precision, to finally define the precision of the system.

On the other hand, an overview of GNSS-R is presented just to put the reader in the context to better understand the contents of this Master Thesis. Then, two different techniques used in the RSLab research group at UPC have been

presented focusing in the understanding of the concept and providing references for deeper understanding.

Finally, the IPT basic equations have been presented in detail, since this is the technique that will be used in this Master Thesis.

As has been seen along section 2.4, GNSS-R techniques have environmental and geological applications giving different solutions to estimate geophysical parameters that are involved in the environmental cycle of the Earth, such as the soil moisture, the sea surface wind speed, the vegetation height, the sea-state, water-level, and a wide range of applications that can be found in the references given along this chapter.

3 CHAPTER 3 HARDWARE DESCRIPTION

In this chapter the hardware used to implement the IPT is described. The instrument is known as the Soil Moisture Interference pattern technique GNSS-R Observations at L-Band Reflectometer (SMIGOL-Reflectometer).

3.1 THE SMIGOL-REFLECTOMETER

From section 2.4.2, it is known that the main restriction in the system is to get linear polarization with a symmetric antenna pattern at V-Pol, which describes the antenna restrictions and determines its design. Then, to get and interpret correctly the power of the GPS signals a GPS receiver with some characteristic properties is needed. Also the system needs somehow to store the data acquired so a datalogger and microSD card are included. Then, another element in the system is its intelligence to correctly apply all the functions required, such as programming correctly the receivers or turning on and off the datalogger and the GPS receiver, which are done by a PIC microcontroller. Finally, as the system is autonomous, it includes a suitable solar power supply system. Figure 3.1 shows the SMIGOL's block diagram and its functionalities.

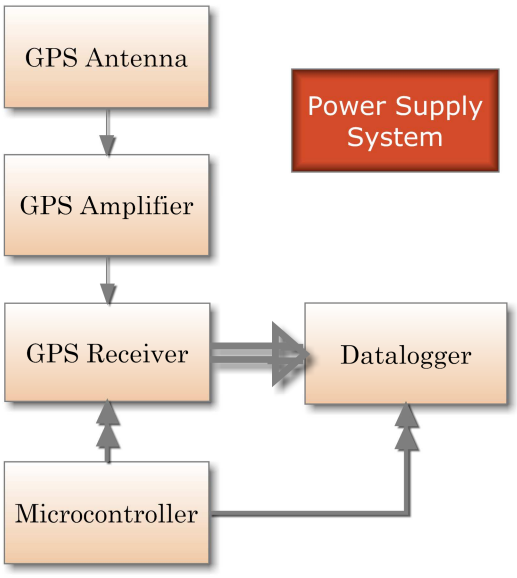

Figure 3.1: Overview of the SMIGOL Reflectometer.

As seen in Figure 3.1, a GPS amplifier has been added to the block diagram because GPS signals are so weak that is necessary to amplify them to be correctly read, and in reception see an interpretable interference pattern. It is related to

receive signals above the sensibility level of the receiver, but avoiding entering in a saturation zone.

3.2 SYSTEM LIMITATIONS

In this section the main restrictions of the systems are discussed

3.2.1 MAXIMUM HEIGHT

The height of the instrument, as described in section 2.4.2 is limited by the coherence time of the GPS signal, $\tau_c = 1\,ms/1023 \approx 0.97\mu s$. This means that the path difference between direct and reflected signals should be less than the coherence time as shown in eqn. (3.1).

$$\frac{\Delta r}{c} = \frac{r_{reflected} - r_{direct}}{c} \approx \frac{2 \cdot h \cdot \sin(90 - \theta_{inc})}{\mathrm{c}} \leq \tau_c \tag{3.1}$$

where:

- $r_{reflected}$: satellite-surface-antenna path,
- r_{direct}: satellite-antenna path,
- c: speed of the light in the vacuum,
- h: the height of the instrument, and
- $\theta_{elev} = 90 - \theta_{inc}$ being θ_{inc} the incidence angle over the surface.

Isolating h, eqn. (3.2) is obtained:

$$h \leq \frac{\tau_c \cdot c}{2 \cdot \sin(\theta_{elev})} \tag{3.2}$$

A graphical explanation is seen in Figure 3.2.

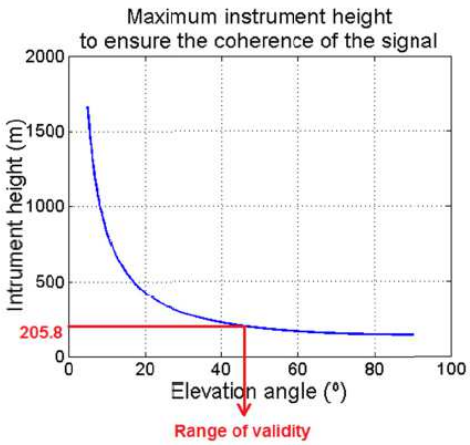

Figure 3.2: Maximum height of SMIGOL Reflectometer [1].

This means that for higher elevation angles the difference in path is larger so the instrument is limited to the maximum elevation angle that is aimed to observe. Generally, interference patterns are analysed between 10º-45º, to avoid distortion and multiple reflections caused by the antenna mast.

3.2.2 ANTENNA FOOTPRINT

Antenna footprint over the reflected surface must be considered to have an idea of what the instrument is measuring. As the antenna is pointing to the horizon, the footprint cannot be the antenna pattern as it is usually done in antenna field. Nevertheless, all the terms presented in section 2.4.1 for the DDM technique lead to a new definition, which is the glistering zone around the specular reflection point.

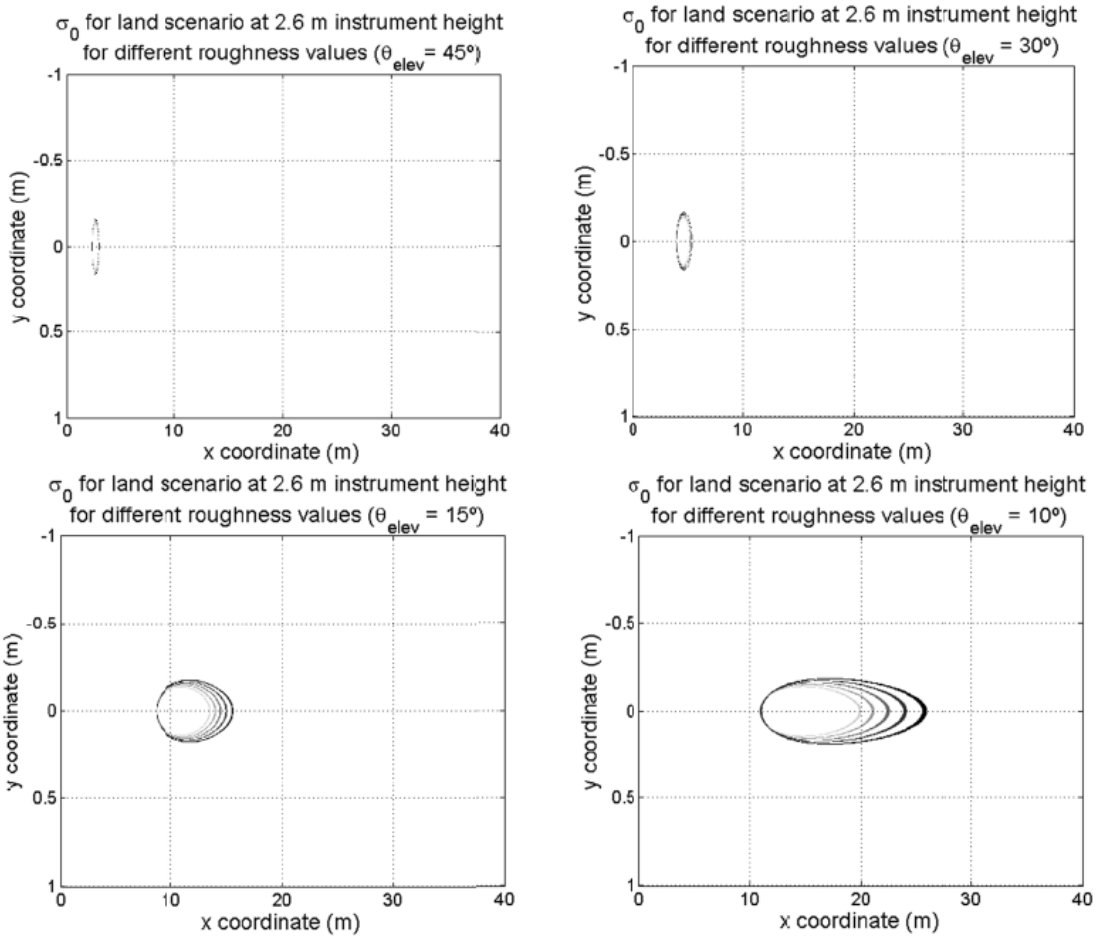

Figure 3.3: Simulated antenna footprint for different elevation angle conditions [1].

As seen in Figure 3.3, as the elevation angle is smaller, the ellipse (or glistering zone) seen over the surface under measurement is enlarged which is coherent because the specular point is further away than for higher elevation angles. The

scattering or glistering zone is the one that says which elements of the surface contribute to the measurements.

3.2.3 RESOLUTION

A way to define the ground resolution of the SMIGOL-Reflectometer is to consider the difference between two consecutive specular reflection points. They depend mainly on the elevation angle as has been seen in Figure 3.3 and on the instrument's height.

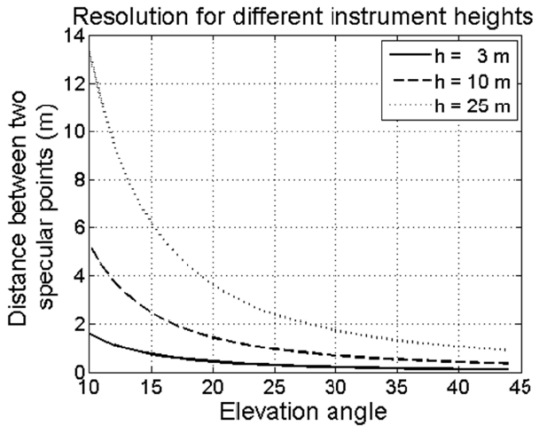

Figure 3.4: Resolution of the SMIGOL Reflectometer as a function of the elevation angle for h=3, 10 and 25 m [1].

From Figure 3.4 two main conclusions can be extracted. For lower elevation angles the glistering zone to consider is larger, which results in having more separation between specular reflection points. Then, as the height is increased, once again the glistering zone is larger and the specular reflection points are more spaced. On the contrary, the higher the height is, the larger the Field Of View (FOV) is.

3.3 GPS ANTENNA

As seen in section 2.4.2, the requirements of the antenna to correctly apply the IPT technique are the following:

- Centred at GPS L1 band (1.57542 GHz) to get the C/A code.
- Matching bandwidth of, at least, 2 MHz to correctly recover the GPS signals.
- Symmetric pattern to equally affect the direct and reflected GPS signals.
- Cross-polar rejection to avoid missing information due to H-Pol interference.

3.3.1 ANTENNA STRUCTURE

The easiest way to design an antenna with previous specifications is using a microstrip printed *patch* antenna. These antennas are known due to be a resonant structure whose size is approximately λeff/2. At GPS L1 the wavelength is 19.04 cm, which means that the antenna should be approximately 9.52x9.52 cm. Diffraction at the edges could appear because the 20x20 cm ground plane cannot be considered infinite. To overcome that problem a substrate called Rogers RO4003 has been included in the patch antenna structure.

The ε_r of the RO4003 is 3.53, resulting in an antenna of theoretically 5.07x5.07 cm, reducing the size nearly by half. Then by empirical approximations the final size of the patch antenna is 4.83x4.83 cm, as seen in Figure 3.5, which is the layout of the patch designed.

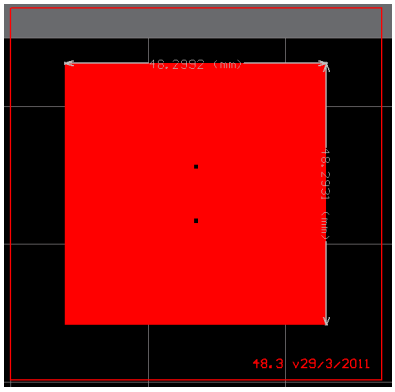

Figure 3.5: Patch antenna dimensions.

One remarkable aspect of Figure 3.5 is that the antenna has two feeding points. This is due to symmetrise the radiation pattern to fulfill correctly the specifications. Then, a 180º hybrid has been introduced to help the symmetrisation of the pattern and make easier and more stable the matching frequency of the antenna. Figure 3.6 shows how the hybrid introduced looks like.

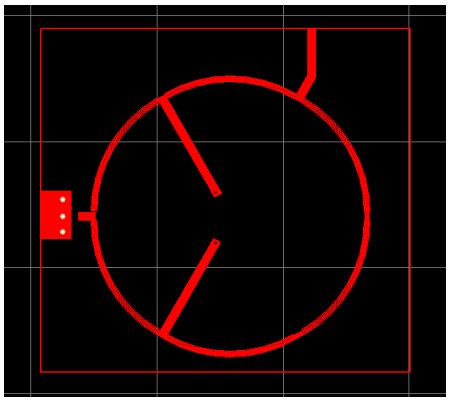

Figure 3.6: 180º hybrid layout.

3.3.2 ANTENNA CHARACTERIZATION

To prove that the behaviour of the antenna is the one expected, it has been characterized in the UPC anechoic chamber. Figure 3.7 summarises the main radiation characteristics of the antenna. It can be seen that the beamwidth of the antenna (-3 dB fading) is larger than 90º, and along it, the radiation pattern is perfectly symmetric (Figure 3.7, subfigures (a), (b) and (c)). Furthermore, a 3-D representation is shown in Figure 3.7 (d) to clearly see the symmetrisation of the pattern along the antenna beamwidth.

Another aspect to comment is the rejection of the perpendicular polarisation, because H-Pol masks the data to be retrieved. Figure 3.8 shows that in the boresight direction the cross-polar rejection is close to 40 dB having as a minimum value 15 dB of rejection.

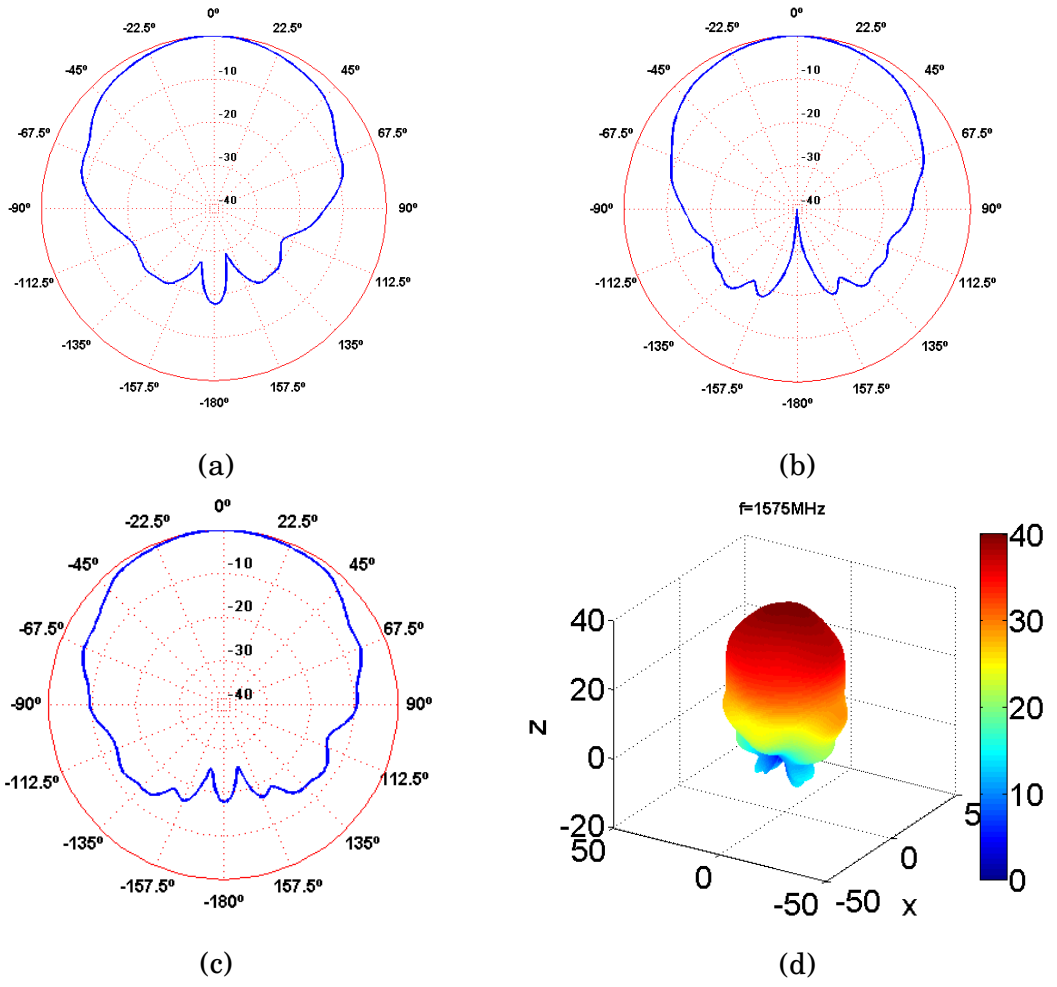

Figure 3.7: Antenna characterization. (a): cut for φ=0º, θ rotation variable. (b): cut for φ=45º, θ rotation variable. (c): cut for φ=90º, θ rotation variable. (d): 3-D representation of antenna radiation pattern [1].

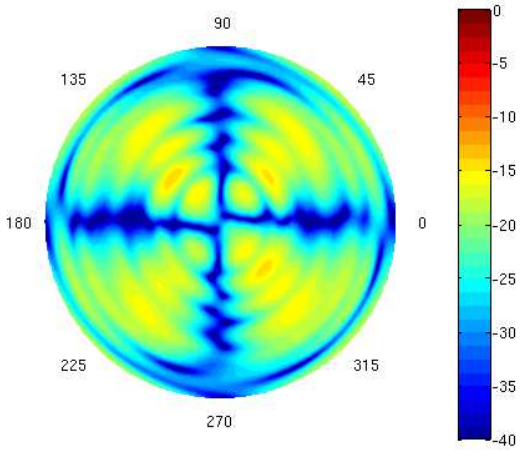

Figure 3.8: Cross-polar rejection representation [1].

Keeping on with the antenna analysis, the final step is to see the matching conditions of the antenna. Figure 3.9 shows that the antenna has been perfectly matched obtaining 30 dB of Return losses at the central frequency and the bandwidth, which is defined as Return Losses (RL) = -10 dB, is around 25 MHz, which is larger than the specification requirements (2 MHz).

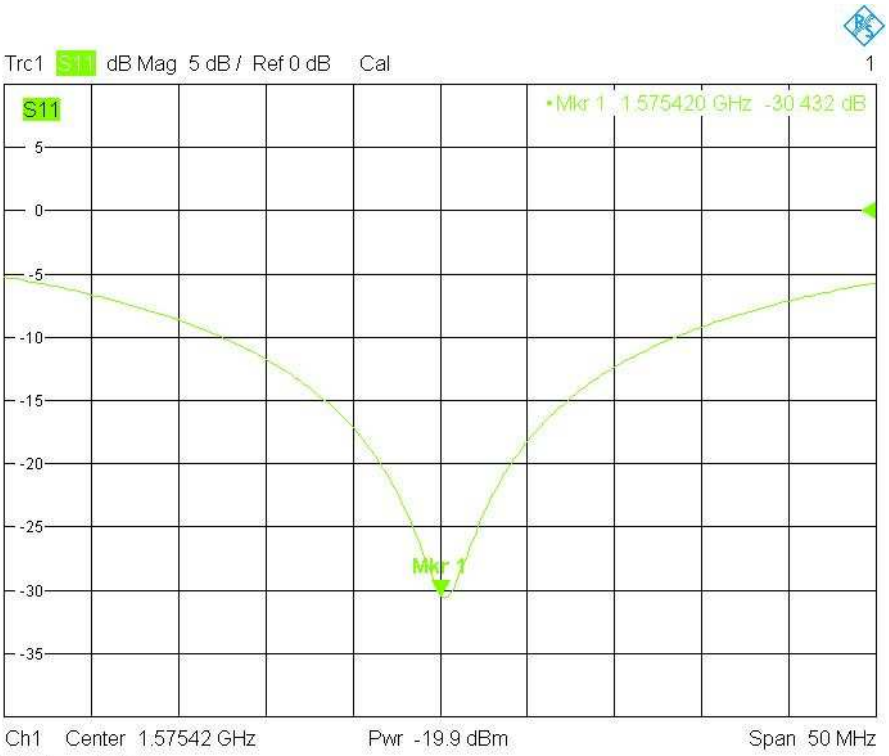

Figure 3.9: Matching representation using a vector analyser [13].

Finally, the antenna of the device looks like Figure 3.10 where the patch (a) and the 180º hybrid (b) can be clearly identified.

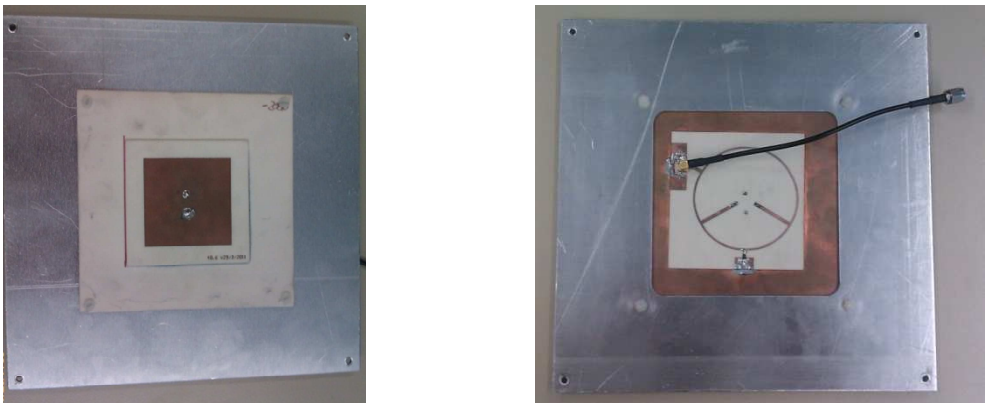

(a) (b)

Figure 3.10: Physical aspect of the antenna. (a): front view. (b): back view.

3.4 GPS AMPLIFIER

It has not been fully justified, but by empirical tests it was observed that a GPS amplifier had to be added to the system after each antenna to recover enough signal power and have some sensibility improvements.

The GPS amplifier included is the SMA661AS which can be found at [14] and has the following properties:

- Low noise factor: 1.15 dB (LNA).
- Theoretical gain: 18 dB.
- Highly Stable.
- High linearity: IP3 = 3dBm.
- Power supply: 3.3V, 8.5 mA.

The amplifier chip includes the matching and biasing networks, which means that only the power supply must be included. Figure 3.11 shows the amplifier model that has been physically implemented (b) in the layout designed (a).

(a) (b)

Figure 3.11: GPS Amplifier: (a) Layout, (b) Physical implementation.

Then, the amplifier has been characterised using a network analyser. Surprisingly, measurements obtained differ a little from theoretical parameters given in the datasheet of the device. Figure 3.12 shows the measurements with the network analyser.

- S11 Parameter: -7.3 dB.
- S21 Parameter: 13.5 dB.
- S22 Parameter: -10.5 dB.

But, the gain obtained is enough to achieve the sensibility specifications for the retrieval algorithms.

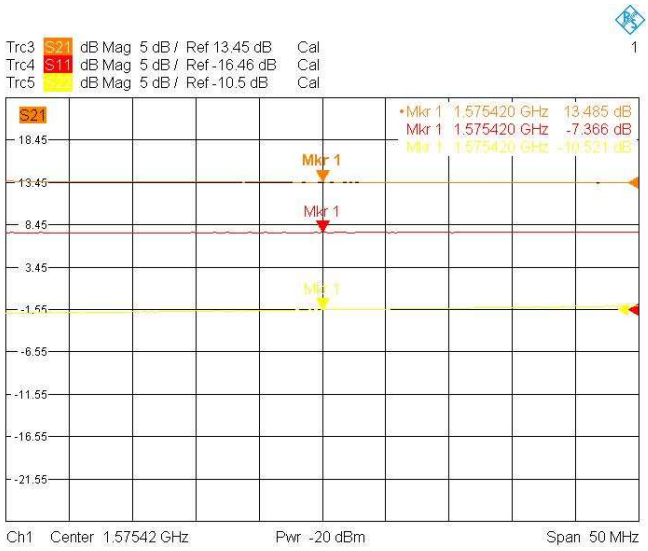

Figure 3.12: S-Parameters of the GPS Amplifier [13].

3.5 GPS RECEIVER

The system needs a GPS receiver that gives at least the following parameters to correctly apply the retrieval algorithm:

- Azimuth information.
- Elevation information.
- SNR.

The GPS receiver is the GPS Trimble Lassen iQ, which is shown in Figure 3.13.

Figure 3.13: GPS receiver of the SMIGOL-Reflectomer [15].

3.5.1 RECEIVER'S DESCRIPTION

The GPS receiver has some specific properties that make it suitable for being used in the SMIGOL –Reflectometer:

- Low power consumption: 3.3V, 26 mA. Critical aspect in an autonomous device.
- Small size: 3x3 cm.
- Trimble Standard Interface Protocol (TSIP) communication protocol: Used just as a matter of experience in the group with this protocol.
- 12-Channel receiver.
- Azimuth and Elevation packets available.
- SNR information.

3.5.2 RECEIVER'S CONFIGURATION

As a matter of communication protocols, the GPS receiver must be configured as follows just because the datalogger only understands data in this format and cannot be changed.

- Speed: 9600 bps.
- Parity: Non.
- Stop bits: 1.

The only difference with the default configuration of the GPS receiver is the parity of the communication protocol. To change all these data, software provided by Trimble, called TSIPCHAT, has been used.

3.5.3 TSIP PROTOCOL

The TSIP protocol has the following structure:

<DLE><ID><*data string bytes*><DLE><ETX>

Where:

- DLE: Refers to 0x10 hex character,
- ID: Packet identification,
- *data string bytes*: Configuration information or GPS information,
- ETX: Refers to 0x03 hex character.

This means that any TSIP configuration packet or TSIP information packet that the GPS sends has the same structure. To configure the receiver to send SNR information the microcontroller must sent to the receiver, when it is turned on, the following stream:

- 0x10 <DLE>
- 0x35 <ID>
- 0x00
- 0x00
- 0x00
- 0x01
- 0x10 <DLE>
- 0x03 <ETX>

Finally, to ask for azimuth and elevation information the following packet must be send to the receiver:

- 0x10
- 0x3C<ID>
- 0x00
- 0x10 <DLE>
- 0x03 <ETX>

As it is not the goal of this Master's Thesis, not very detailed information about the receiver has been shown, just the basics, but for more information it is advisable to look at the datasheet or [13].

3.6 DATALOGGER

As in any remote and autonomous system, the data acquired must be stored somehow to then process it, which is done by a datalogger and a microSD card. In the early versions of the device, datalogger Logomatic v2 was included (Figure 3.14).

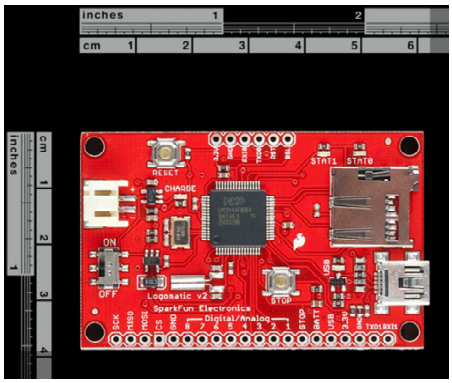

Figure 3.14: Dataloggger Logomatic v2 [15].

The main characteristics of this datalogger are the following:

- Voltage supply: 3.3V,
- Current: 80 mA,
- Small size,
- Storage capacity: microSD card,
- Data rates: 2400 bps - 115200 bps,
- Cold start: 2 seconds.

The main problem of this datalogger is the high current that it needs to work out. So, in the second generation of the hardware it has been changed to datalogger OpenLog (Figure 3.15), which has the following properties:

- Voltage supply: 3.3V,
- Current:
    - 2 mA Idle
    - 8 mA storing
- Very small size.
- Storage capacity: microSD card,
- Data rates: 2400 bps – 115200 bps, and
- Cold start: 2 seconds.

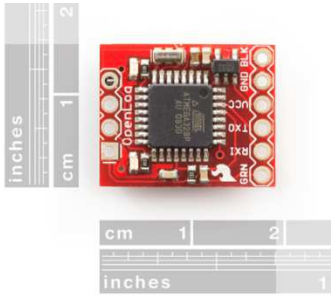

Figure 3.15: Datalogger Openlog [15].

By changing the datalogger, power consumption problems have been overcome. The change in the datalogger is totally transparent to the system because the only function that it does is to store in a file all data received by its input port.

3.7 SYSTEM INTELLIGENCE: PIC MICROCONTROLLER

The "intelligence" of the system is given by a PIC microcontroller (µC). Mainly, their main activities are:

- Turn on GPS receiver, datalogger and GPS amplifier via a C-MOS switch (Figure 3.16). When the PIC introduces a logic '0' the N-MOS transistor is in its cut region making the P-MOS transistor being in the cut region too, which means that the any device connected is not powered. On the contrary, when the PIC introduces a logic '1' the N-MOS transistor works in its conducting region, resulting in different voltages at the source and gate ports of the P-MOS transistor, making it work in the conducting region. So any device connected is powered.

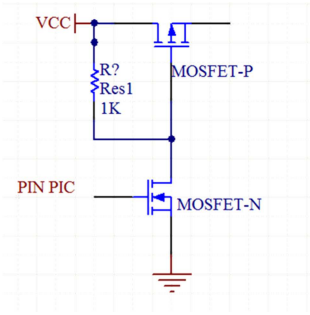

Figure 3.16: C-MOS Switch [13].

- Configure the GPS receiver in raw data mode when they are initialized, via a Universal Asynchronous Receiver-Transmitter (UART) connection.
- Monitor the battery voltage to protect the system and to increase the battery life-time. These monitoring is done by sensing PIN AN0 [1]. If the voltage drops below 3.1V the system is automatically disconnected until the charging process has made the supply voltage to go above 3.6V, which allows the system to be reconnected again, creating a hysteresis cycle. Without the hysteresis cycle the system could enter in a infinite loop of being connected and disconnected.
- Every 30 seconds elevation and azimuth commands are sent to the GPS receiver via UART to obtain elevation and azimuth data of satellites.

- After 6 hours of continuous working cycle the GPS receiver, the datalogger and the GPS amplifier are disconnected to allow the solar panels to charge the batteries. It is done just for power requirements and not getting rid of power supply.
- After 6 hours sleeping the PIC restarts the whole system.

Figure 3.17 shows a summary of the working cycle that the system does to obtain the data required. Then, Figure 3.18 show the hardware integration of the system resulting in shared board between the PIC and the GPS receiver.

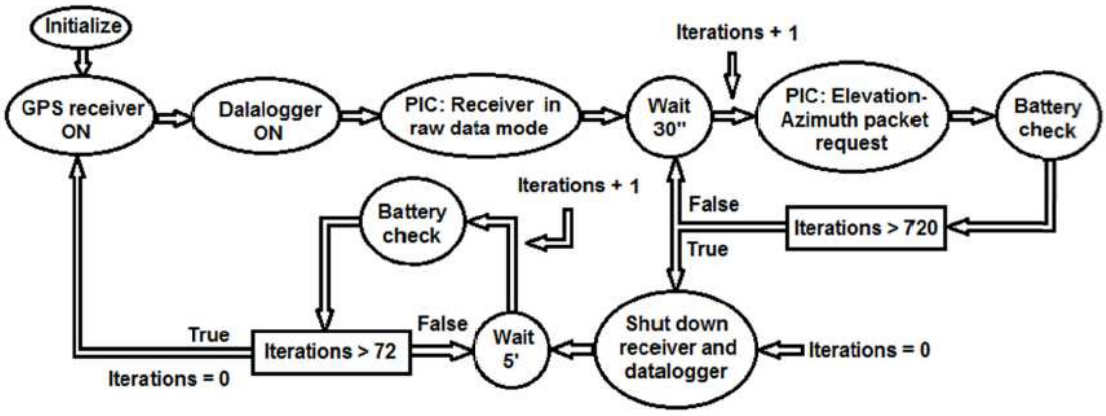

Figure 3.17: Working process flowgraph of the SMIGOL-Reflectometer [1].

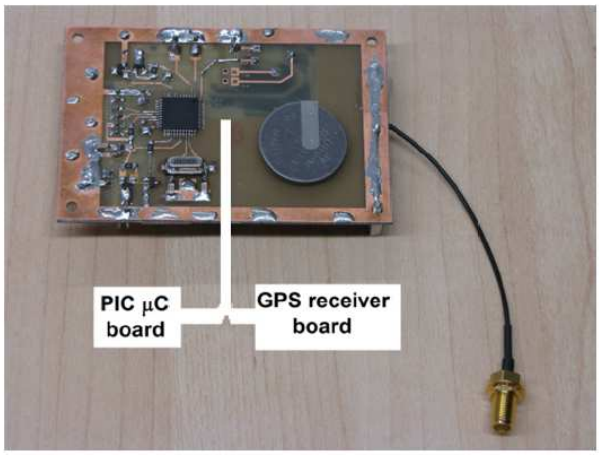

Figure 3.18: Hardware integration: PIC board and GPS Receiver board [1].

3.8 POWER SUPPLY SYSTEM

A first requirement before designing a power supply system is to make a power consumption budget. In the SMIGOL-Reflectometer case is the following:

- GPS Receiver: 34 mA,
- GPS Amplifier: 8 mA,

- Datalogger Logomatic v2: 80 mA,
- PIC: 10 mA,
- Total: 132 mA.

As the instrument is autonomous it needs at least batteries and a recharge system driven by solar panels. Furthermore, a buck boost power supply is added to take profit of all the current given by the solar panels. The main sketch of the power supply system is shown in Figure 3.19.

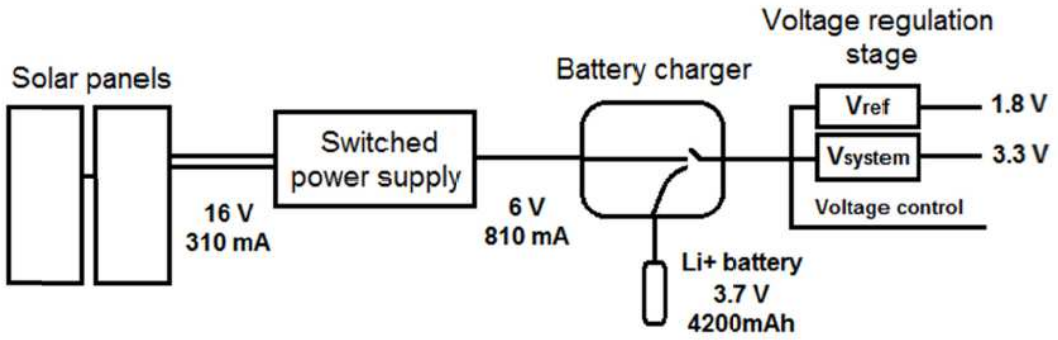

Figure 3.19: Overview of the power supply system [1].

The voltage of the solar panels is given to the buck boost power supply to regulate the voltage and convert the excess voltage into current. Then, the battery charger acts as a switch. The system is powered by the solar panels, when its power is above the power budget level. At the same time, batteries are charged with the excess current. During night time, when the power given by the solar panels is not enough, the system is driven by the batteries. The only requirement for this design is just to be able to charge the batteries during day-time.

This configuration has 3 different outputs:

- 3.3V: Supply the system,
- 1.8V: Reference voltage for the PIC, and
- Voltage control: used by the battery life-time control explained in section 3.7.

3.8.1 BUCK BOOST POWER SUPPLY

Figure 3.20 shows the main schematic of a buck boost power supply. To make easier the designers work, there are some electronic components prepared to work as adjustable buck boost power supply sources. In the SMIGOL Reflectometer the chip LM2575 has been chosen to do this work. In Figure 3.21 the recommended

circuit for this chip is shown. By tuning R1 and R2 resistances the 6V at the output can be obtained, which is limited by a voltage regulator in the system input. Figure 3.21 shows the physical implementation of the buck-boost power supply.

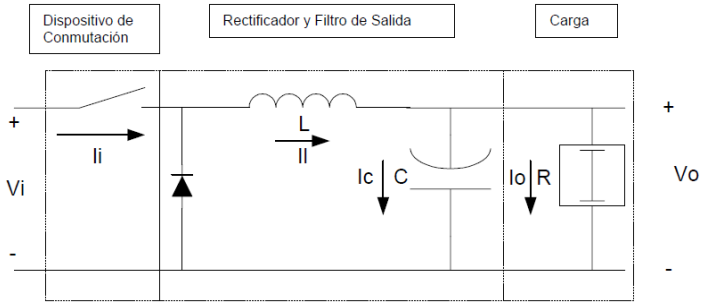

Figure 3.20: Schematic of a buck-boost power supply.

C_{IN} — 100 µF, 75V, Aluminum Electrolytic
C_{OUT} — 330 µF, 25V, Aluminum Electrolytic
D1 — Schottky, 11DQ06
L1 — 330 µH, PE-52627 (for 5V In, 3.3V out, use 100 µH, PE-92108)

Adjustable Output Voltage Version

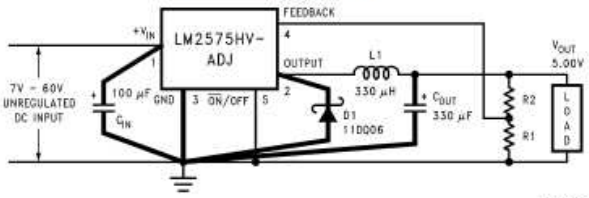

$$V_{OUT} = V_{REF}\left(1 + \frac{R2}{R1}\right)$$

$$R2 = R1\left(\frac{V_{OUT}}{V_{REF}} - 1\right)$$

where V_{REF} = 1.23V, R1 between 1k and 5k.
R1 — 2k, 0.1%
R2 — 6.12k, 0.1%
Note: Pin numbers are for the TO-220 package.

Figure 3.21: LM2575 recommended circuit.

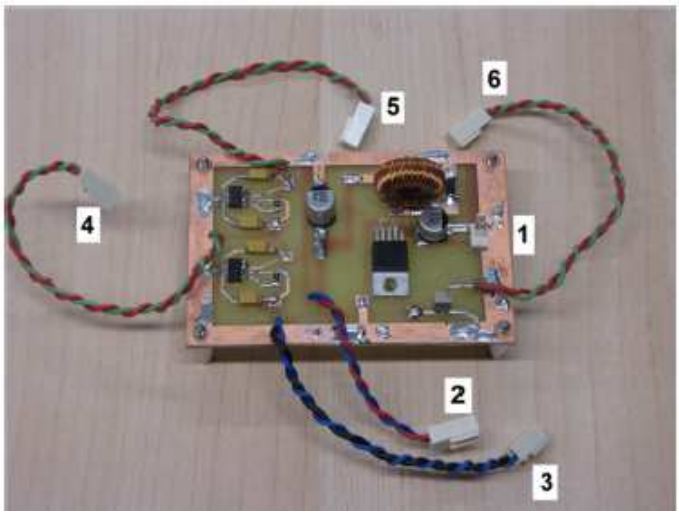

Figure 3.22: Physical implementation of the buck-boost power supply [1].

The connections shown in Figure 3.22 are the following:

1. Solar Panel connection.
2. Battery charger input.
3. System's input voltage (Battery charger output).
4. 3.3 V, working voltage of all the elements in the system.
5. 1.8 V, reference voltage for the PIC.
6. Reference voltage to check the battery health.

3.8.2 BATTERIES

Litium batteries are the ones chosen to drive the SMIGOL-Reflectomer. Their main properties are:

- Output voltage: 4.2V,
- Maximum current given: 4200 mAh.

Figure 3.23: Lithium batteries [13].

3.8.3 BATTERY CHARGER

To do this function an electronic component designed specially to charge Lithium batteries is used (MAX1757). The recommended circuit is the one shown in Figure 3.24 and its physical implementation in Figure 3.25. This device chooses from where the whole system is powered. If there is enough sun power the system is powered from the solar panels and the extra current generated is used to charge the batteries. On the contrary, if there is not enough sun power, the system is powered directly by the lithium batteries. Here is where the hysteresis cycle commented before plays an important role in order not to damage the batteries.

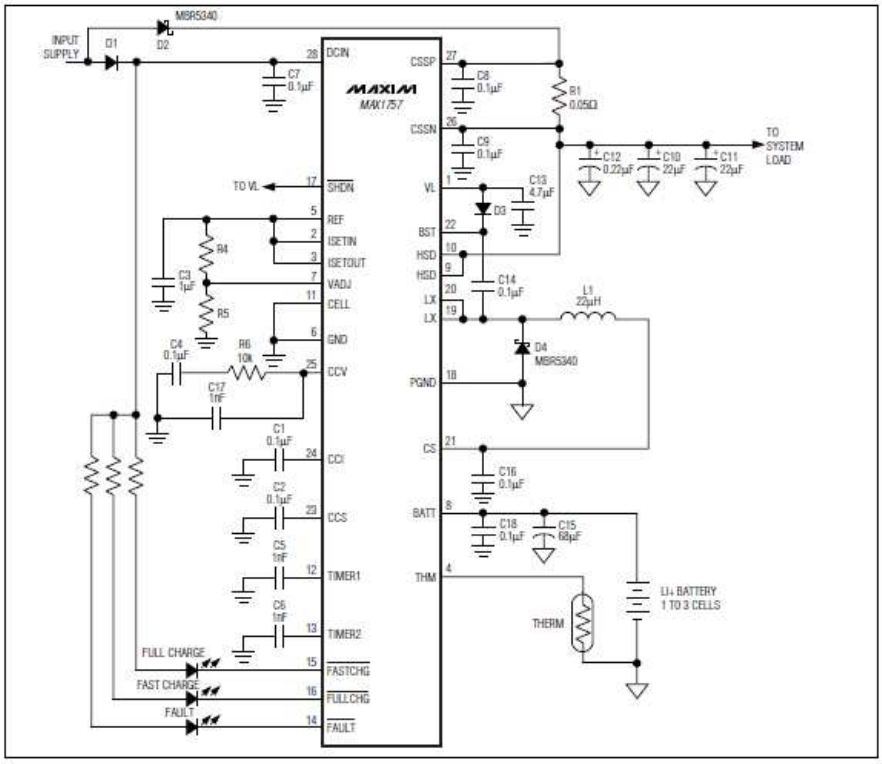

Figure 3.24: Recommended circuit for the MAX1757 [13].

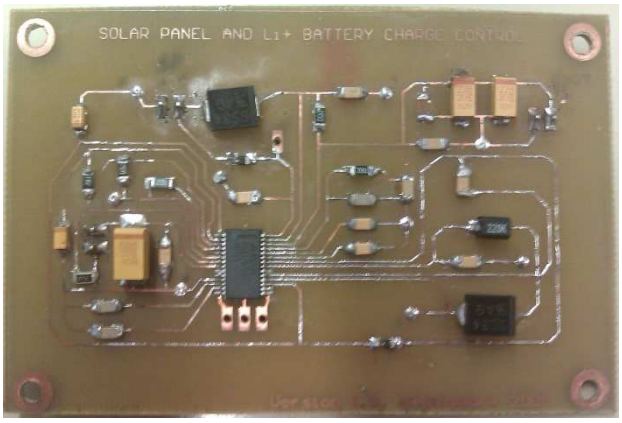

Figure 3.25: Physical implementation of the battery charger [13].

3.8.4 SOLAR PANELS

The last part of the power supply system is the solar panels. Two different models have been tested depending on the weather conditions that will suffer the device during measurements (Figure 3.27). Furthermore, in order to protect the solar panels they are connected using a diode system shown in Figure 3.26.

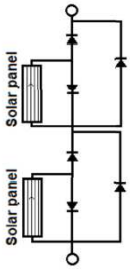

Figure 3.26: Solar panel connections [1].

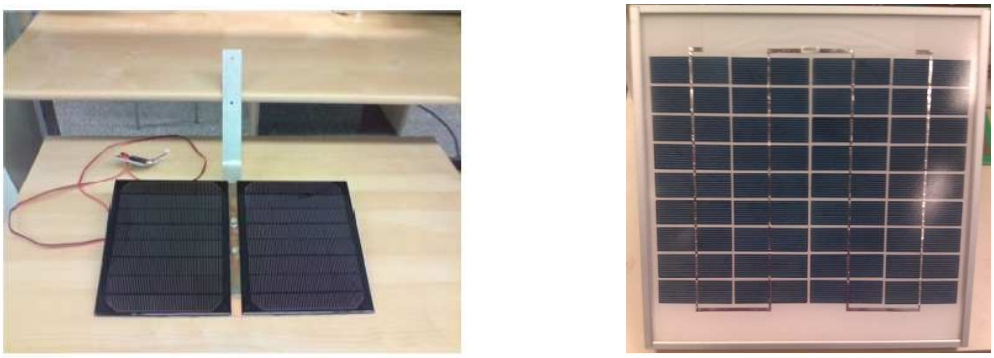

(a) (b)

Figure 3.27: Solar panels. (a): Normal operation. (b): for extreme working conditions such as low temperatures or snow.

3.9 INTEGRATION&STRUCTURE

To use it as a ground based instrument an aluminium cube of 4 mm thickness has been used as seen in Figure 3.28.

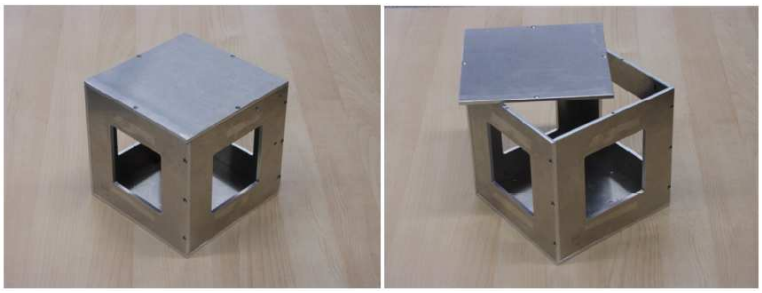

Figure 3.28: Aluminium external structure.

It is made of metal to enlarge the ground plane of the antennas to avoid diffraction at the edges. Although the structure is prepared to work with four faces, for some applications or tests just one is necessary.

All the hardware is integrated in a layered structure to fit it well inside the box. Figure 3.29 shows the layered structure.

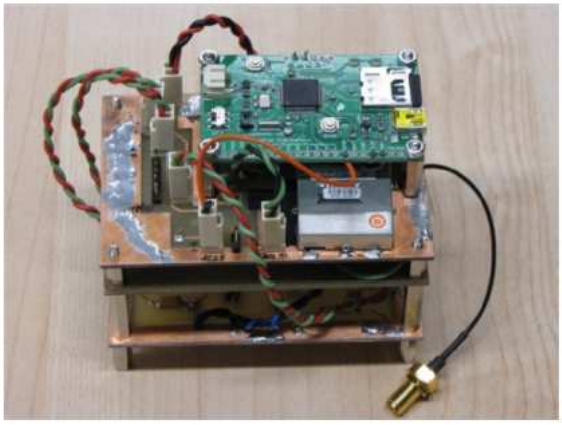

Figure 3.29: Hardware integration [1].

Finally, the instrument is covered by a radome, as seen in Figure 3.30, to protect it from environmental conditions.

Figure 3.30: SMIGOL-Reflectometer covered by a radome.

3.10 THE SMIGOL-WHITE VERSION

For a different measurement campaign with extreme environmental conditions, such as very low temperature and snow, a different integrated structure was designed. The lithium batteries were changed by lead batteries and the structure was smartly designed to be putted in any place. The rest of the hardware developed has remained the same. Figure 3.31 shows the physical appearance of the SMIGOL-White instrument.

As this device has been totally proved under very bad conditions, working perfectly during 6 months, it is the one that has been chosen to do the measurements shown in Chapter 5.

Figure 3.31: SMIGOL-White structure.

3.11 SUMMARY

This chapter has presented the main features of the hardware instrumentation used for the measurements done in this Master's Thesis. An overview of the whole design is seen commenting then each block individually.

The SMIGOL-Reflectometer basically consists on:

- A GPS Antenna at the L1 band with a symmetric pattern at V-Pol,
- a GPS amplifier,
- a GPS commercial receiver that gives azimuth and elevation information,
- a low-power datalogger to store the data,
- a PIC microcontroller to give intelligence to an autonomous device, and
- a power supply system based on lithium batteries, solar panels, a buck boost power supply, and a battery charger.

The physical structure of the device has also been presented.

Finally, the three main restrictions (maximum height, antenna footprint and resolution) that appear due to using the IPT technique have been detailed characterising the operational margin.

4 CHAPTER 4 INTERFERENCE PATTERN TECHNIQUE: REVIEW OF EXISTING APPLICATIONS

This chapter introduces the main applications of the IPT that were developed along a Ph.D Thesis dissertation [1].

4.1 SOIL MOISTURE RETRIEVALS: BARESOIL

This situation is the simplest that can be seen over land. Basically, it consists of a two-layer model; one is air and the other is land surface. With this situation a theoretical interference pattern can be simulated as is shown in Figure 4.1.

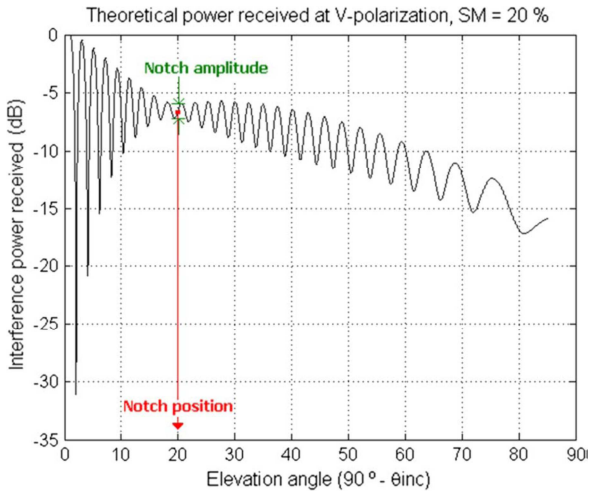

Figure 4.1: Simulated interference pattern at V-Pol for land with 20% of soil moisture [1].

The evolution of the pattern can be clearly seen as a function of the elevation angle, as explained in section 2.4.2. Looking at Figure 4.1, the first step is to identify the angle corresponding to the notch, which is the point of minimum oscillation amplitude. This angle can be converted to incidence angle by eqn. (4.1).

$$\theta_{elev} = 90 - \theta_{inc}, \tag{4.1}$$

where:

- θ_{elev} corresponds to the elevation angle in degrees (satellite observable), and
- θ_{inc} refers to the incidence angle over the surface in degrees.

Once the incidence angle is known, the ε_r can be obtained by means of eqn. (2.29), which relates the refraction index of the surface directly with the Brewster angle, which is, by definition, the maximum transmission angle. The angle where the notch appears corresponds to the Brewster angle because the reflected wave is

multiplied nearly by 0 (maximum transmission angle), and only the effect of the direct wave is seen in the pattern. Theoretically, if there was no presence of soil moisture the amplitude of the notch should be 0. But, due to the presence of soil moisture, the reflection coefficient is not totally 0 and this is why some amplitude is seen, Figure 4.2. It is seen that for 0% soil moisture, at V-Pol, the reflection coefficient is totally 0, whereas as the percentage of soil moisture increases this 0 value is no more a 0 value and it starts to grow up.

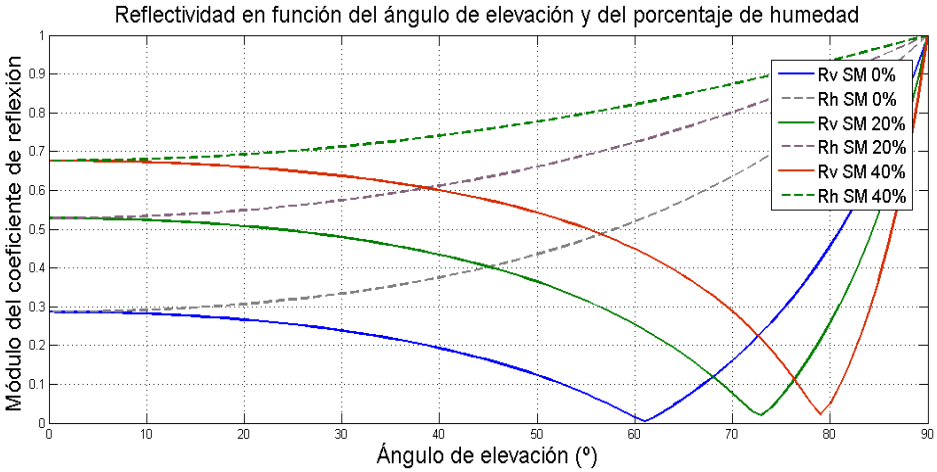

Figure 4.2: Reflection evolution as a function of the incidence angle for different soil moisture values (blue=0%, green=20%, red=40%) and both polarization H-Pol (dashed lines) and V-Pol continuous lines.

Another remarkable aspect that should be clarified from Figure 4.2 is that as the percentage of soil moisture increases the Brewster angle also increases. This is due to the fact that, as soil moisture increases, the ε_r of the surface increases too, increasing the Brewster angle.

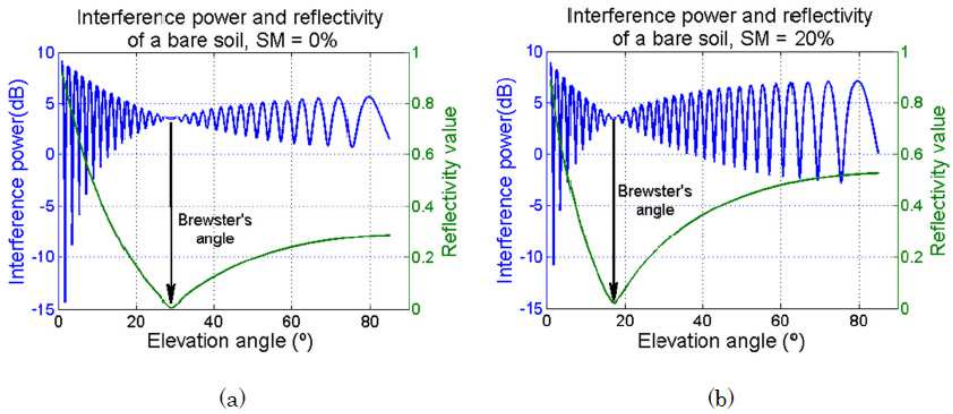

Figure 4.3: Interference pattern (in dB) and reflectivity curve as a function of the elevation angle for two different soil moisture values (0% and 20%) [1].

Figure 4.3 summarises the interference pattern interpretation for bare-soil situations. It shows the commented effects: the change in the notch position and in

the amplitude of the notch. Then, ε_r retrieval is directly related to the soil moisture of the surface by theoretical models. But, with this algorithm it is only possible to extract punctual information. To get a 2-D Map more aspects are taken into account.

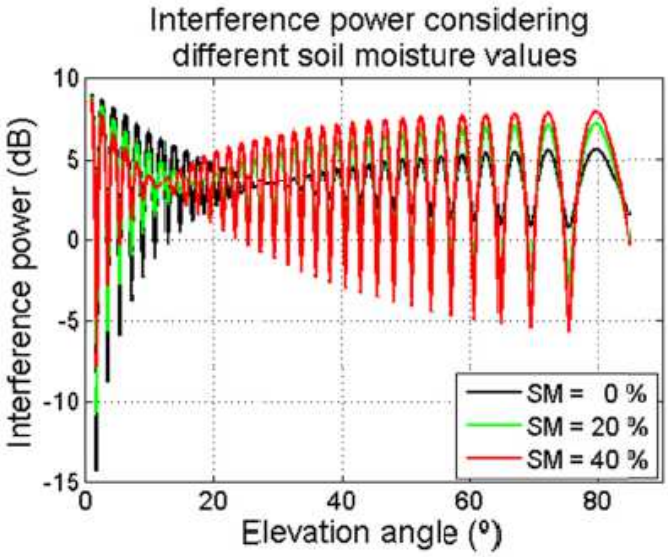

Figure 4.4: Interference pattern simulated for different soil moisture values [1].

As seen in Figure 4.4, when soil moisture changes, the amplitude of the notch and its position varies, but it also changes the amplitude of the whole pattern. By analysing and comparing the amplitude of theoretical patterns, for different soil moisture values, with the measured one, the soil moisture in the rest of the points, where the GPS signal is reflected can be retrieved.

Summarising, the process to obtain soil moisture is:

- look for the notch position,
- obtain the incidence angle of the notch,
- obtain ε_r,
- estimate the soil moisture value for the notch position, and
- analyse the amplitude of the whole pattern to obtain the soil moisture retrievals in the rest of the reflection points.

Some uncertainty depending on the surface roughness is found, but taking as a reference the notch position, the lower uncertainty is obtained, Figure 4.5.

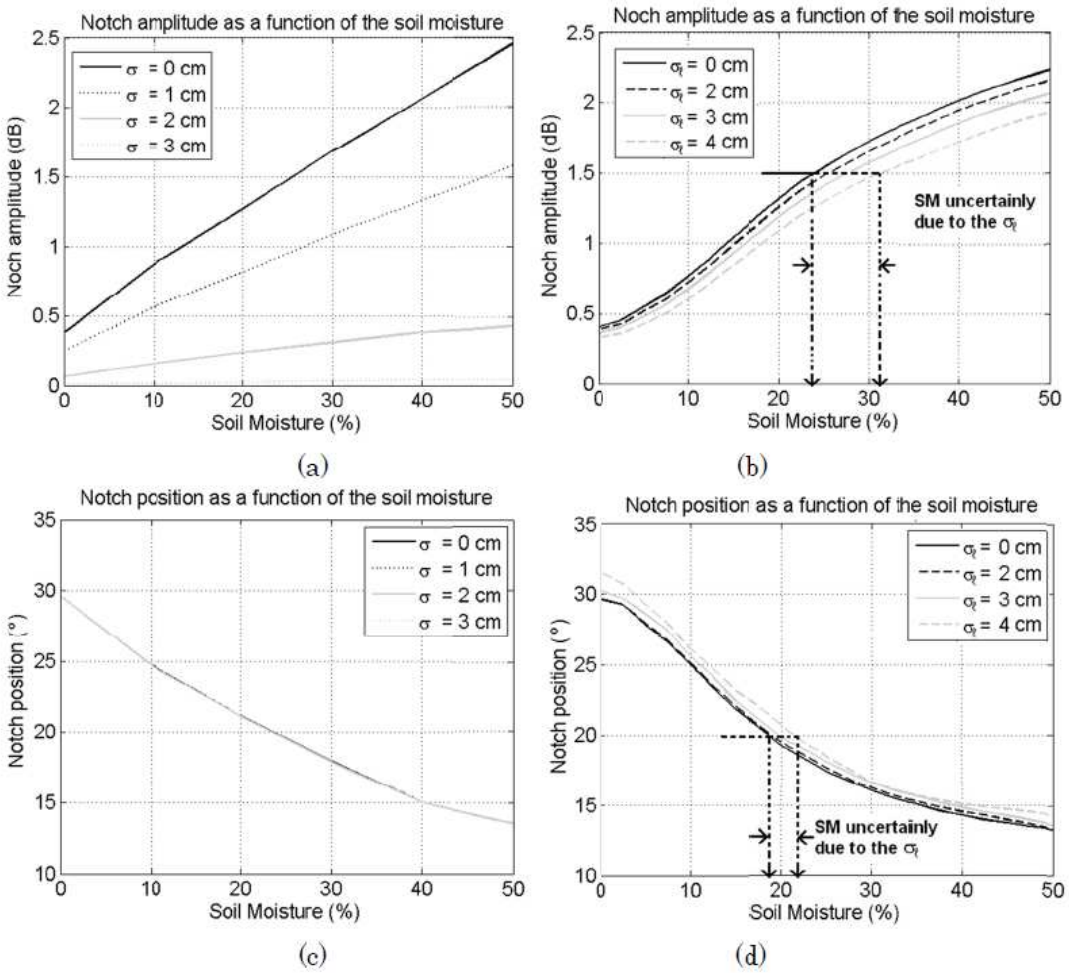

Figure 4.5: Uncertainty introduced by surface roughness. (a) and (b): refer to obtaining soil moisture by evaluating the notch amplitude, whereas (c) and (d): show the uncertainty by taking as a reference the notch position [1].

To get the final results, topographic corrections are applied as it will be explained in section 4.2. Then, Figure 4.6 shows soil moisture results testing the algorithm. On the left the 2-D soil moisture maps obtained are shown for different days. On the right side, the comparison of the retrieved values with the ground-truth is observed. It is seen that the values retrieved do not differ much with the ground-truth data. Furthermore, probes cannot be totally reliable because depending on where they are put the retrieved soil moisture value can change more than a 4% which is higher than the error obtained with the SMIGOL-Reflectometer. Figure 4.7 shows a summary of the retrieval algorithm implemented.

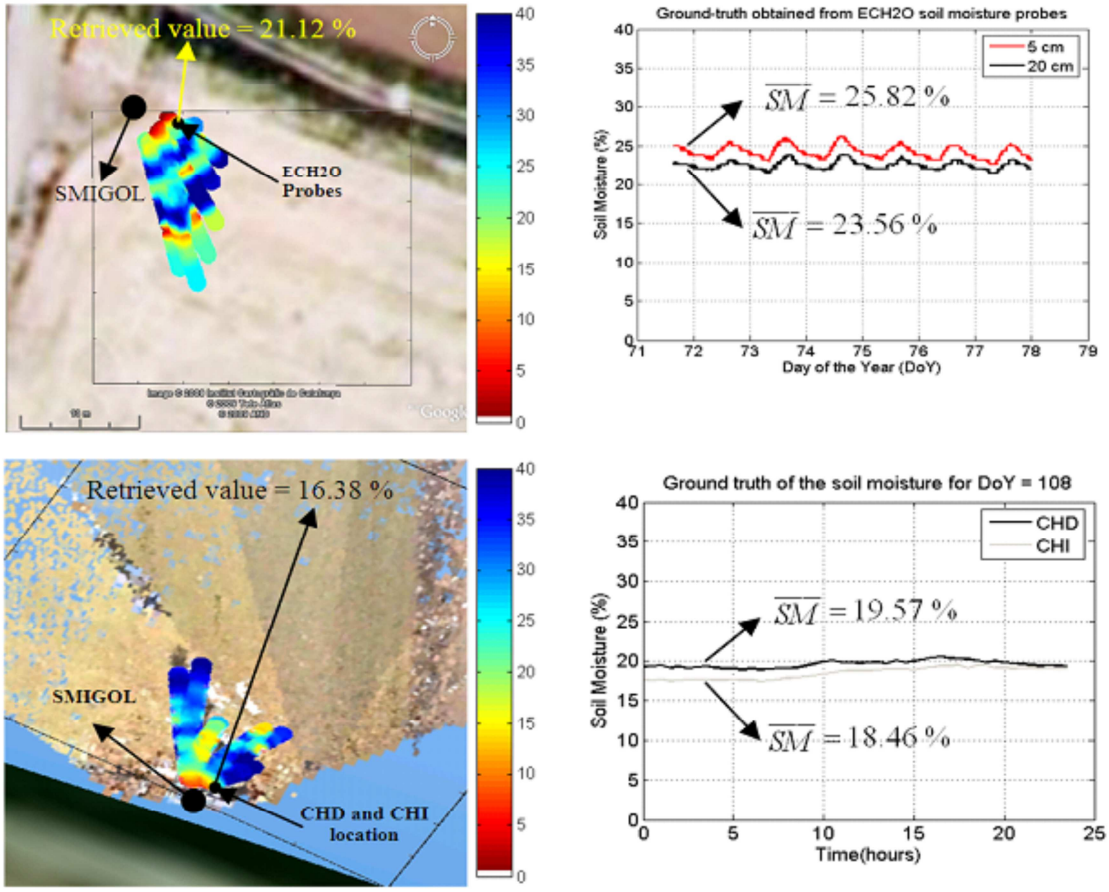

Figure 4.6: Soil moisture results compared with the ground-truth data (soil moisture probes) at different penetration values [1].

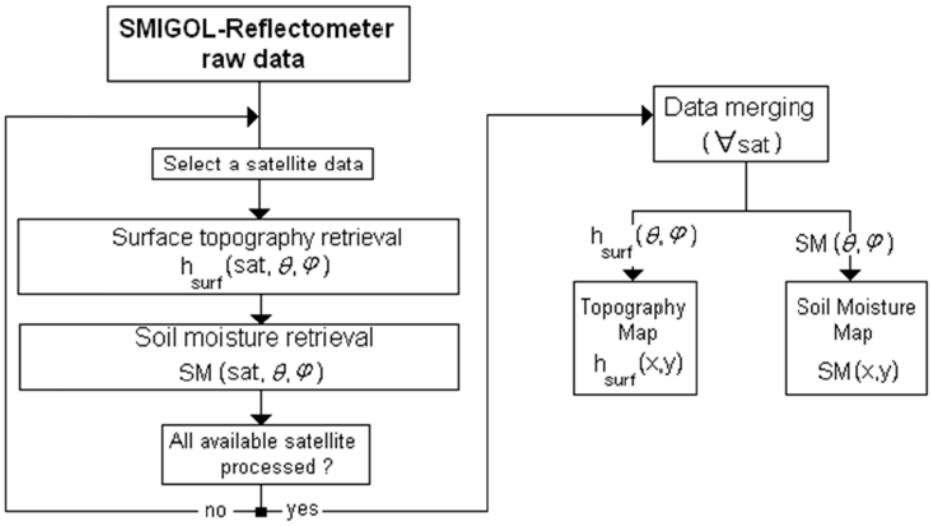

Figure 4.7: Soil moisture retrieval algorithm [1].

4.2 TOPOGRAPHY RETRIEVALS

It was mentioned before that to retrieve soil moisture it is necessary to apply first some corrections due to topography variations. But how does topography affect the interference pattern?

It is mostly related to the oscillation frequency of the interference pattern because the phase term mentioned in eqn. (2.23) is the one that is related to the patch difference between direct and reflected signal. As seen in Figure 4.8 for different paths, a different oscillation frequency is seen and a different SMIGOL height can be retrieved, which is related with topography changes.

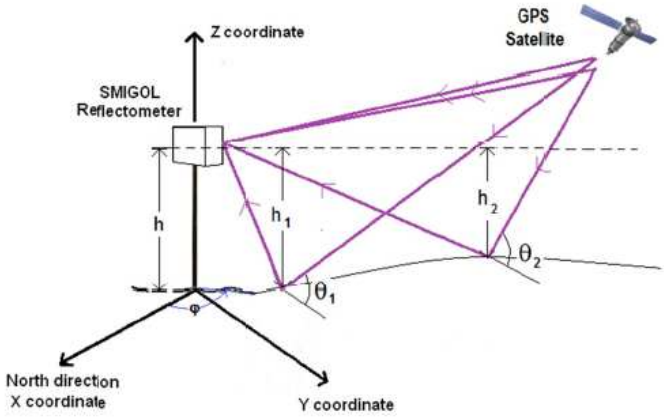

Figure 4.8: Geometry of topography studies with IPT.

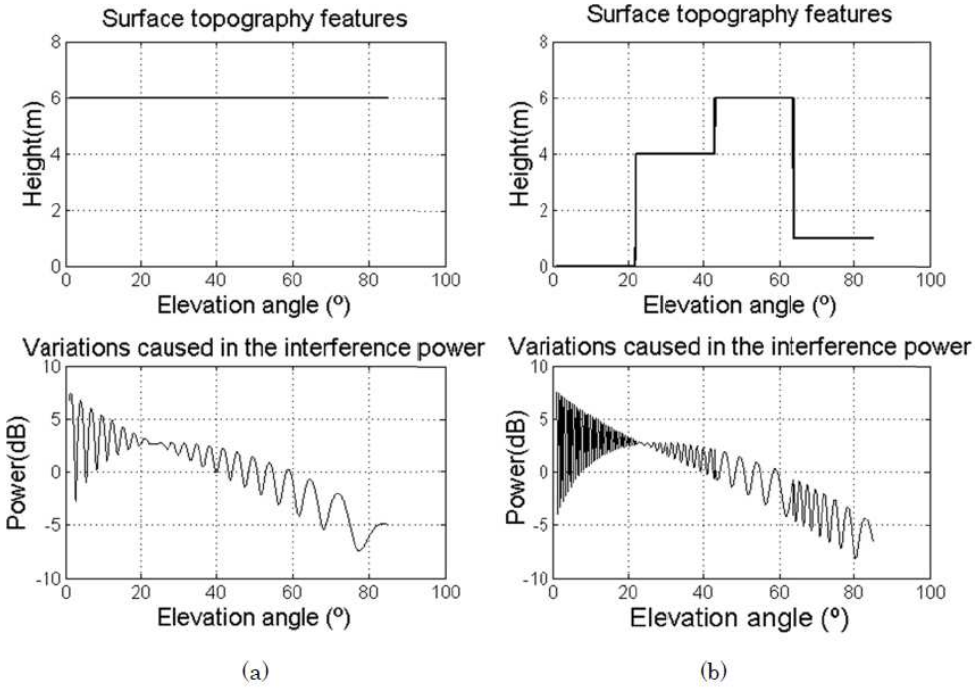

Figure 4.9: Variation of the received interference pattern due to topography changes [1].

Figure 4.9 shows how the oscillation frequency of the interference pattern changes when there is a height difference between reflected points, mostly seen in subfigure (b).

So to recover topography information of the observed surface, it is necessary to look at the oscillation frequency of the pattern and its variations. One approach, for example, is to look at the relative maximum and minimum points of the pattern and trying to compare it with a theoretical one at a certain height, Figure 4.10. Therefore, it is possible to observe the change in the oscillation frequency between consecutive periods.

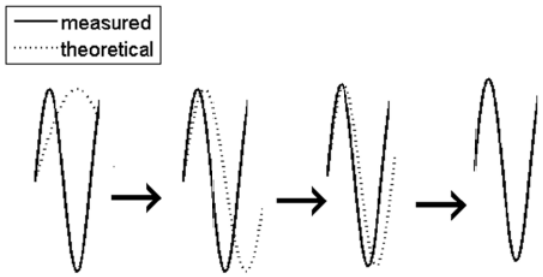

Figure 4.10: Adjustment of the measured interference pattern with a theoretical one [1].

Consequently, just by knowing the height of the instrument at the origin, the topography map can be retrieved by computing the equivalent height shown in Figure 4.8. Eqn. (4.2) shows the formula to extract topography information.

$$h_{surface} = h_{origin} - h_{retrieved}, \tag{4.2}$$

where:

- h_{origin} is the real height of the instrument at the origin (0,0),
- $h_{retrieved}$ is the equivalent instrument retrieved height computed for each satellite, and
- $h_{surface}$ is the topography information of the observed surface.

In general, the only thing that the algorithm does is to look at $\Delta\theta_{os_i}$ values shown in Figure 4.11 and relate them with the evolution of the surface height.

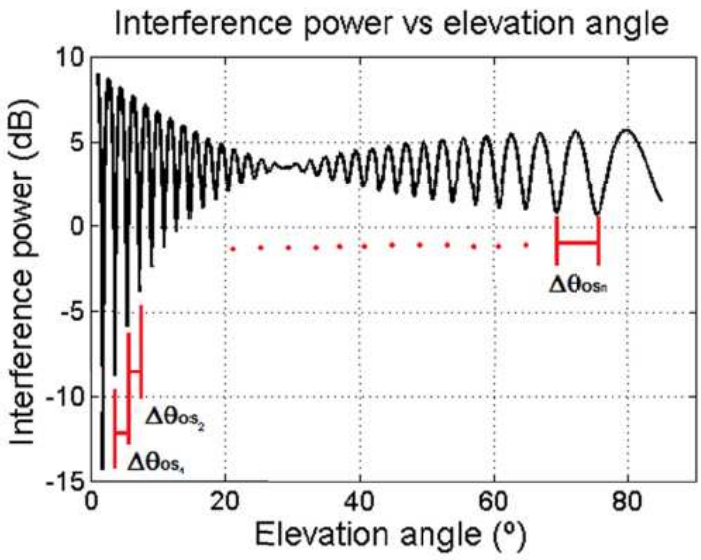

Figure 4.11: Computing topography retrievals [1].

4.3 VEGETATION HEIGHT RETRIEVALS

It has been proven that the IPT works very well when few geophysical parameters play a role in the equations, topography, soil moisture and surface roughness. In this section an algorithm to retrieve vegetation height is presented. When vegetation is present in the scene, a three-layer model can be defined, being the first layer the air, the second one the vegetation, and the third one the soil surface. Figure 4.12 shows the theoretical interference pattern obtained

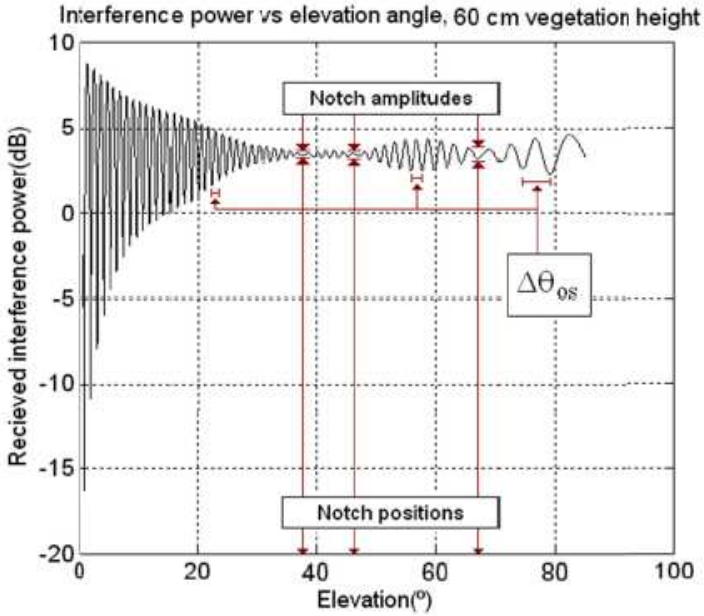

Figure 4.12: Theoretical interference pattern obtained when there is a vegetation layer of 60 cm in the scene [1].

where:

- $\Delta\theta_{os_i}$ refers to the change in the oscillation frequency of the interference pattern, which refers to topography,
- there is more than one notch in the pattern, and
- notch amplitudes and notch positions are determined.

The number of notches depends on the thickness of the vegetation layer, as shown in Figure 4.13.

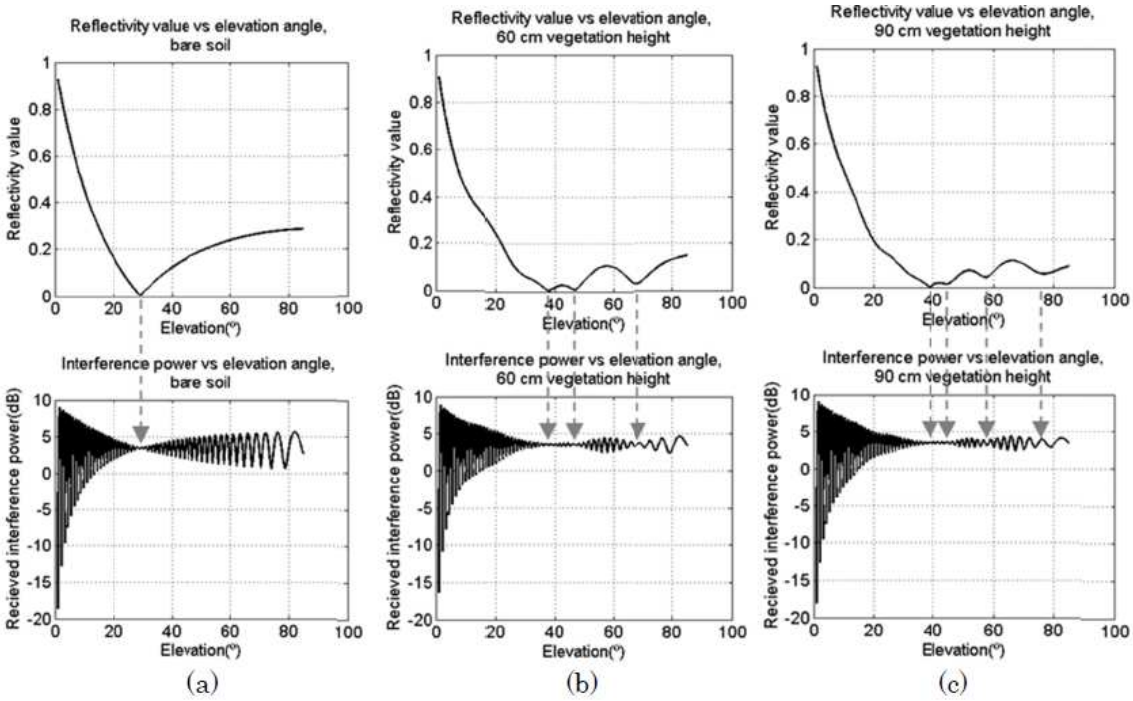

Figure 4.13: Interference patterns obtained for different vegetation layer heights. (a): bare soil, 0 cm of vegetation height. (b): 60 cm of vegetation layer, 3 notches appear. (c): 90 cm of vegetation height layer, 4 notches appear [1].

Therefore, intuitively, it is seen that there is a relationship between the number of notches and the vegetation height, and it follows, obviously, the reflection coefficient curves, (Figure 4.14). One of the notches corresponds to the Brewster angle and the other ones to the multipath effect due to the vegetation layer where multiple reflections occur inside. This vegetation layer can be modelled as a layer of a determined thickness with a constant dielectric permittivity.

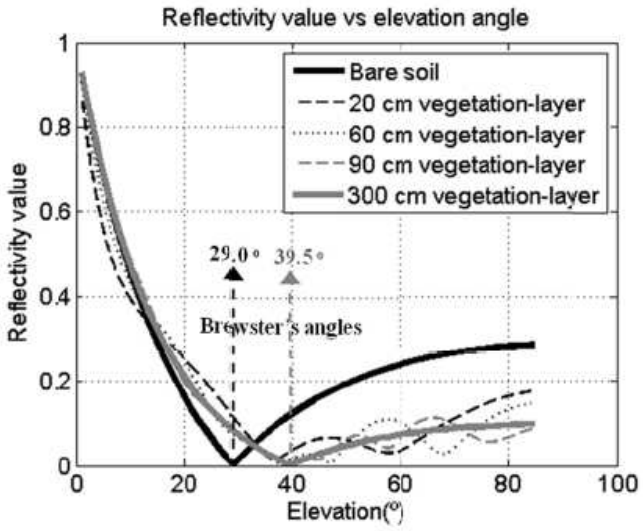

Figure 4.14: Reflectivity curves as a function of the elevation angle for different values of vegetation thickness [1].

In Figure 4.14 it is seen that for a vegetation layer of 3 m thickness there is no more influence of the soil roughness and soil moisture in the interference pattern which means that the model is more similar to having just two layers (air + vegetation), being the notch obtained (Brewster angle) to the corresponding ε_r of the vegetation layer. Therefore for vegetation thickness higher than 3 metres, the algorithm does not perform correctly.

The retrieval algorithm developed for vegetation-covered soils is shown in Figure 4.15.

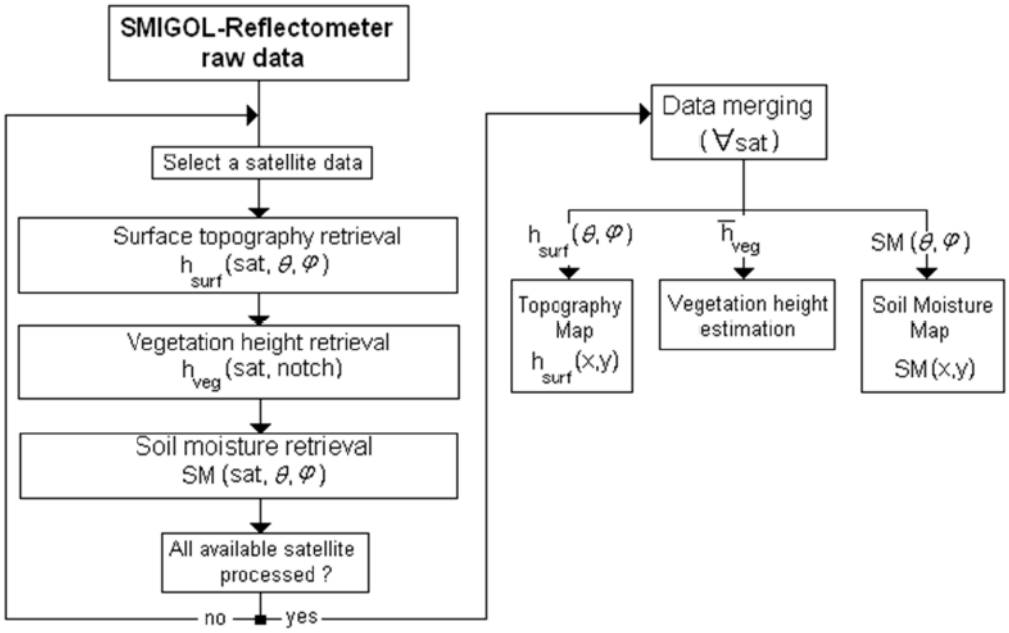

Figure 4.15: Vegetation-covered soil retrieval algorithm [1].

Basically, the retrieval algorithm is based on retrieving first the surface topography by looking to the change in the oscillation frequency comparing it with the SMIGOL height at the origin. Then, by the height and the dielectric constant of vegetation layer over the field, theoretical models are developed and the number of notches and their positions (data measured) are compared with them, as done in Figure 4.16 for maize vegetation.

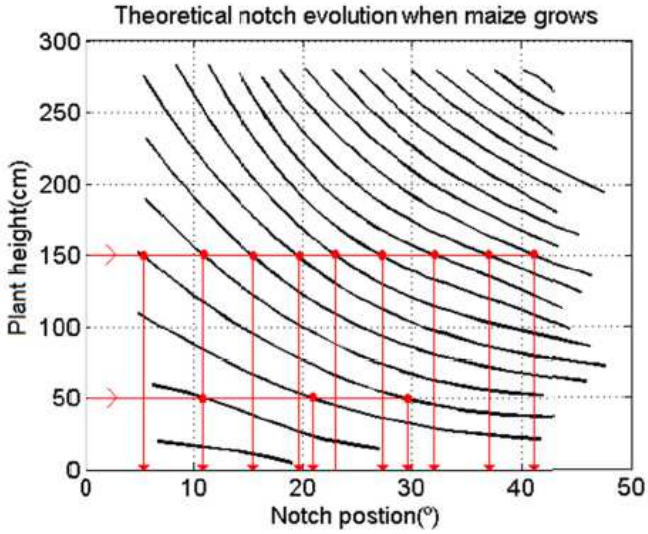

Figure 4.16: Theoretical model of the maize plant: determining the height as a function of the number of notches and its position [1].

The final step is to is determine soil moisture by looking at the amplitude of the different notches. Now, it cannot be used the Brewster angle because it is not possible to identify which is the corresponding notch. So, by comparing with a theoretical model developed for each kind of vegetation, soil moisture is retrieved, Figure 4.17.

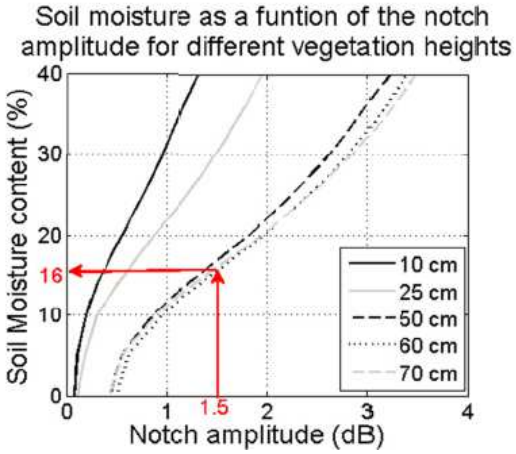

Figure 4.17: Soil moisture as a function of the notch amplitude for different vegetation heights [1].

To end this section some measurements are shown. In Figure 4.18 the evolution of maize is seen by processing data of different days. It is seen that for black dots (Maize height retrieved (cm) for each satellite in sight) a tendency is followed, but if the average value is computed (red dots), the ground-truth and mean height retrieved are perfectly matched.

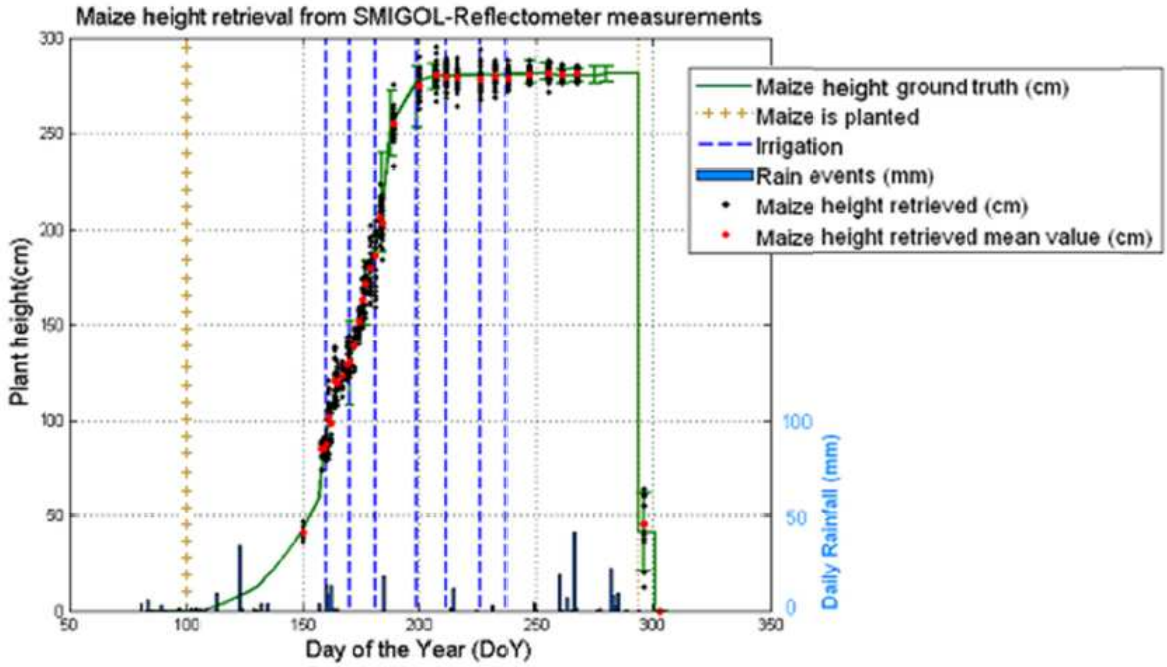

Figure 4.18: Maize height compared with ground-truth data [1].

Once again, in Figure 4.19 (a) it is seen the variability for all satellites in sight, but the mean values match the ground-truth. In Figure 4.19 (b) the evolution of barley over the days is seen and the mean values (black stars) match very well the ground-truth retrieved values.

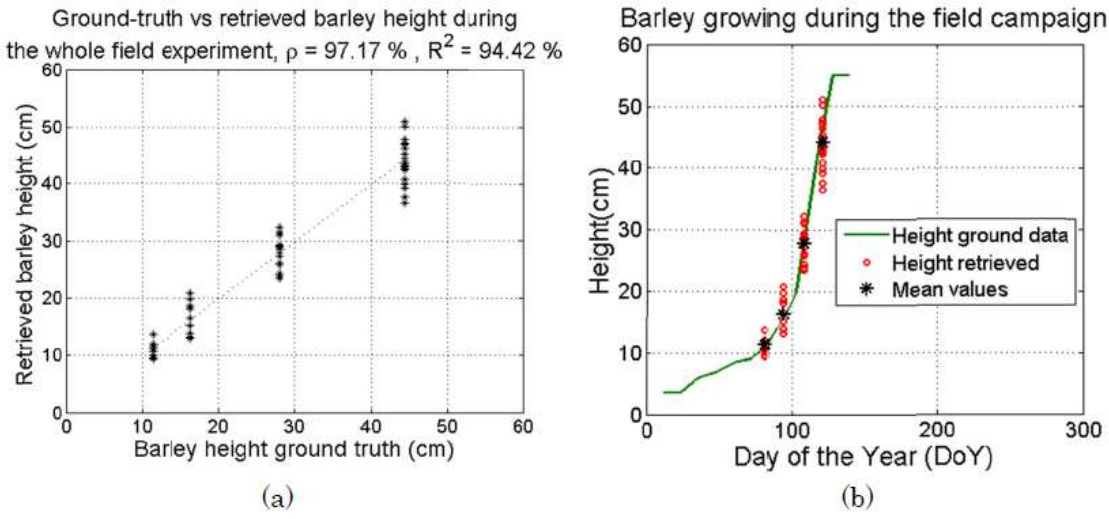

Figure 4.19: Barley height study during a field campaign [1].

4.4 WATER LEVEL MONITORING IN RESERVOIRS

This application is a particular case of the topography retrieval application. As seen in Figure 4.20, once again the oscillation frequency varies as a function of the instrument height. Therefore, if an initial ground-truth value is known, the evolution of water in a reservoir can be monitored. A remarkable point is that water in reservoirs is totally calm water and its level does not vary within the measurement hours, it varies from time to time or when rain events happen.

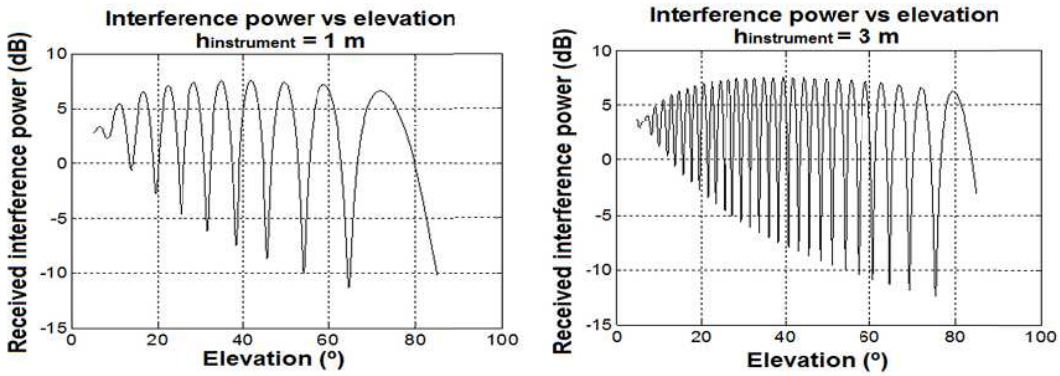

Figure 4.20: Interference pattern as a function of the elevation angle [1].

So this technique was proposed to monitor water level and has been tested in a field campaign. The retrieval algorithm is the same than for topography: the pattern is split in windows of relative maximums and minimums and the oscillation frequency is monitored, computing the corresponding heights of the instrument. Finally, an average can be performed because the water-level in reservoirs do not change quickly during the measuring time.

Now, some results obtained are shown:

Figure 4.21: Field appearance. (a): overview. (b): FOV of the SMIGOL [1].

Figure 4.21 shows the appearance of the field campaign. Then, Figure 4.22 shows the signals recovered from two different days (October 30th, 303 DoY, and December 10th, 344 DoY, of 2010). The black line refers to the measured pattern and dotted line corresponds to the retrieved interference pattern.

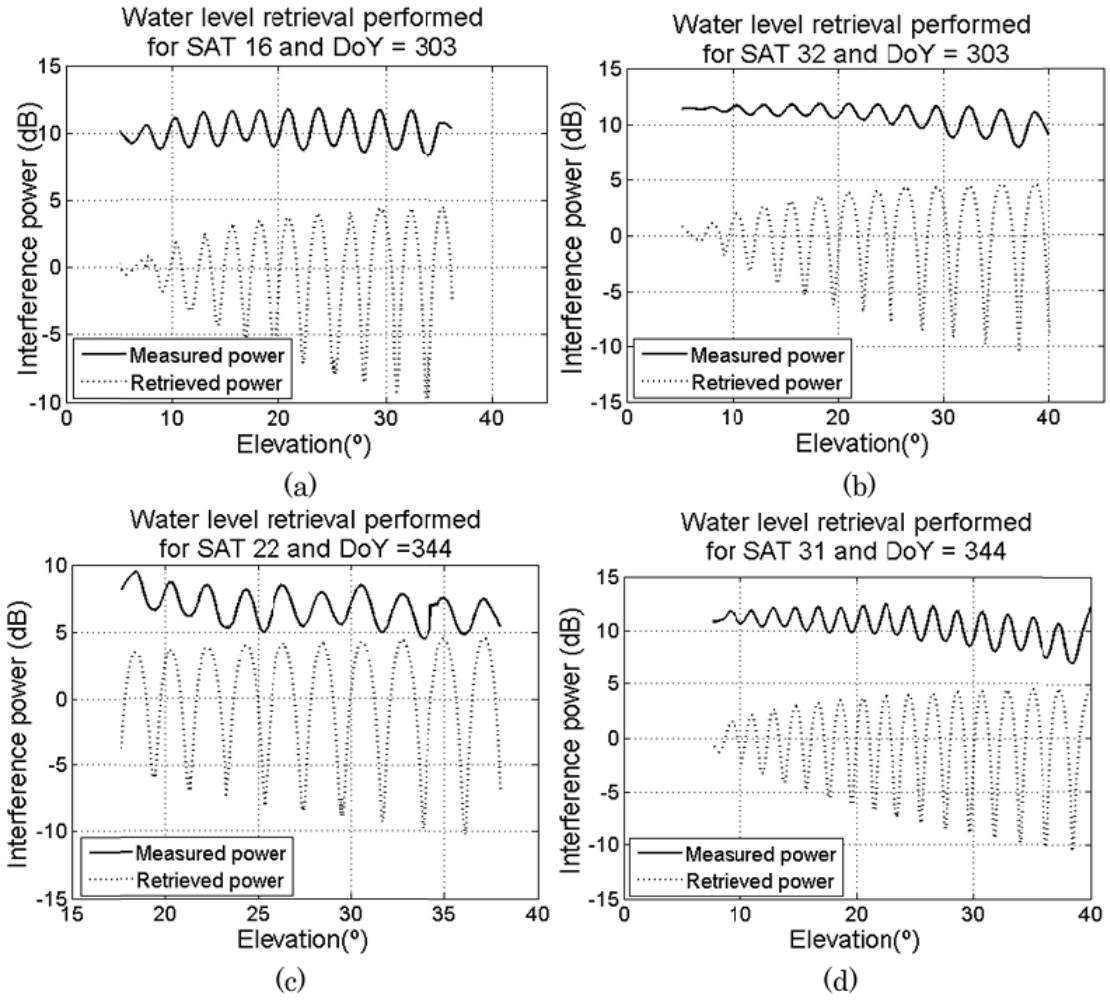

Figure 4.22: Signals recovered [1].

In this field campaign the ground-truth value was measured with a laser, with an accuracy of +/- 1.5 mm averaging 10 independent measurements. The ground truth value data obtained was:

- October 30th: 2.14 m.
- December 10th: 3 m.

Finally, results obtained for the same satellites are shown in Figure 4.23.

SAT	Mean level retrieved	σ	RMSE	Δh
16	2.133 m	0.6 cm	0.9 cm	0.7 cm
32	2.127 m	0.6 cm	1.4 cm	1.3 cm

SAT	Mean level retrieved	σ	RMSE	Δh
22	**2.982 m**	**6.7 cm**	**8.8 cm**	**1.8 cm**
31	**2.991 m**	**0.9 cm**	**1.3 cm**	**0.9 cm**

Figure 4.23: Results obtained [1].

4.5 SUMMARY

In this chapter a summary of the main IPT applications developed in the RSLab research group at UPC have been shown providing some experimental results to prove the good performance of the technique.

This chapter starts with the easiest case, which is bare-soil, obtaining topography and soil moisture retrievals. Then, when the vegetation layer is introduced the model gets more complex obtaining different shapes in the interference patterns. Finally, a particular application of the topography retrievals the water-level monitoring is found.

In general, when looking an interference pattern obtained by the IPT technique the main points where to focus are:

- oscillation frequency of the pattern, which is related to topography or water level,
- Brewster angle (notch), which is related to soil moisture,
- The number of notches and their positions, which are related to the vegetation height, and
- The amplitude of the notches that are related with soil moisture again.

5 CHAPTER 5 FIELD EXPERIMENT

This chapter presents the field experiment carried out to test the SMIGOL-Reflectometer on a dynamic surface. The experiment is fully detailed and so is the data processing performed. An empirical formula is developed pending to be tested with data from a larger field campaign.

5.1 FIELD EXPERIMENT DESCRIPTION

In order to test the IPT technique over a dynamic surface (sea) the harbour of Vilanova i la Geltrú (41°12'46.35"N, 1°44'11.12"E) has been selected for three main reasons:

- available ground-truth data of water tides (RADAR VEGA PULS),
- available ground-truth data of wind speed (Meteorological station), and
- high-speed dynamics of the sea due to sea-waves or currents can be neglected due to being inside a harbour.

Therefore, the water can be in principle modelled as a low-dynamic surface where water is calm and it only should vary due to sea-tides.

Figure 5.1: Schematic of the field experiment, all the elements presented are mark at its position.

Figure 5.1 shows an overview of the Field experiment. It was done on the January 19, 2012, starting at 7:00h. and ending at 16:30h. Now, some images describing the field are presented. Figure 5.2 shows the SMIGOL-Reflectometer together with the RADAR VEGA PULS [16].

Figure 5.2: SMIGOL Reflectometer and RADAR VEGA PULS [16].

Figure 5.3: Instrument at 10:00h, 19/01/2012.

Figure 5.4: SMIGOL-Reflectometer at 16:00h, 19/01/2012.

Figure 5.3 and Figure 5.4 show the instrument installation and FOV at different times of the day. At 10:00h water appears to be totally calm, but at 16:00h it is easy to identify the appearance of small waves in the sea surface. This means that the model of calm water is not totally accurate and signals obtained must be analysed critically to see how this roughness affects them.

5.2 ANALYSIS OF THE SIGNALS OBTAINED

The signals obtained in this field campaign can be divided in two different blocks. The ones obtained in the morning, where the sea surface is quite flat, which means with small roughness, and the ones obtained in the afternoon where the sea surface was much more dynamic. Figure 5.5 shows the interference power patterns of the signals obtained in the morning, as a function of the elevation angle. It can be seen that signals are quite clean and look like the signals obtained in the reservoir experiment. Then, Figure 5.6 shows once again the interference power patterns as a function of the elevation angle, but now the signals retrieved look like much noisier than the ones obtained in the morning. This is mainly due to the sea surface roughness, which was larger, and the effect of “noise” (fast oscillations) is seen in the pattern. If we try to link this concept with the DDM technique presented [2], it is seen that if sea surface roughness is higher, the glistering zone is larger, and contributions from a larger area reach the antenna, and as they preserve the signal coherence, consequently they affect the interference power retrieved.

A good aspect of this noisy signal is that information about sea surface roughness is hidden in the fast oscillations. The goal is to extract it, as well as the surface's level (tides), which was the original goal.

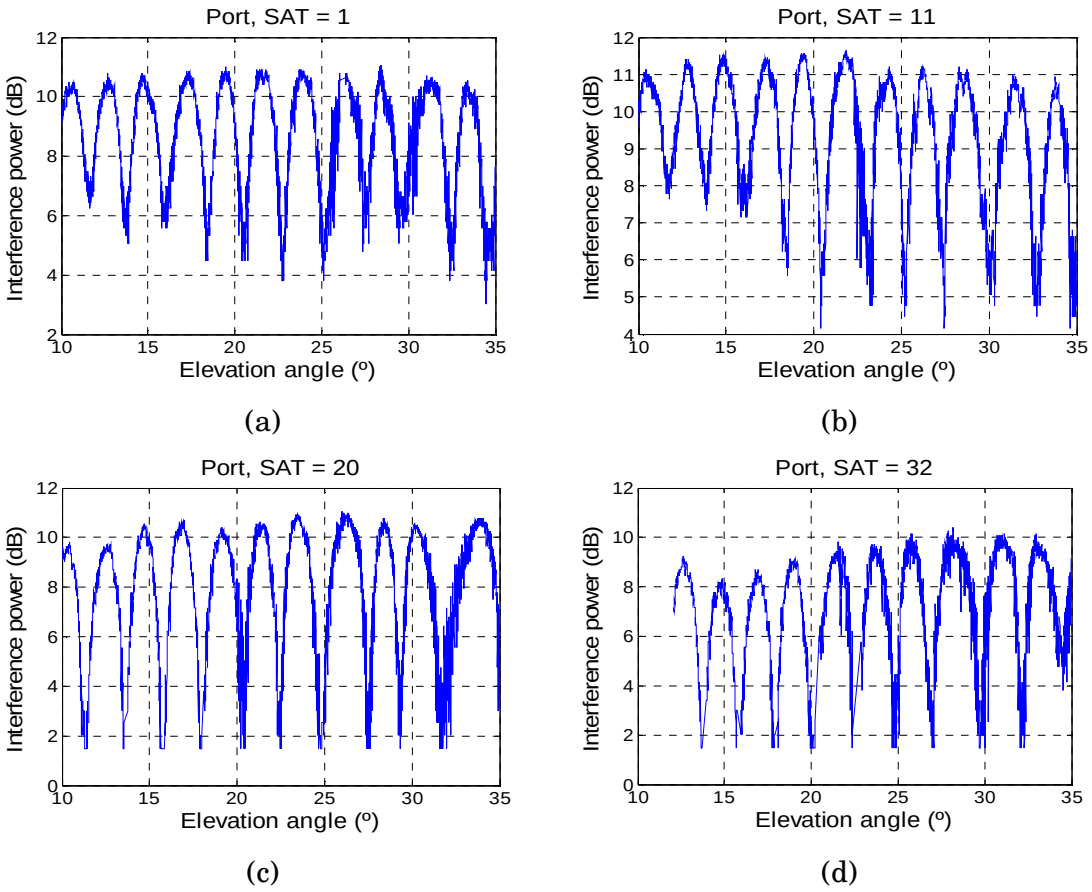

Figure 5.5: Signals obtained in the morning (7:00h-13:00h, 19/01/2012), interference power pattern as a function of the elevation angle.

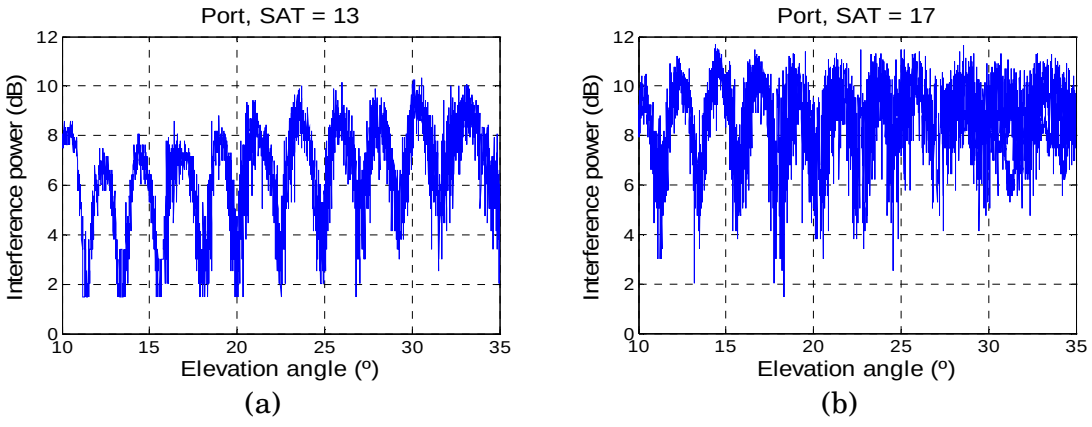

Figure 5.6: Signals obtained in the afternoon (13:00f-16:30h , 19/01/2012), interference power pattern as a function of the elevation angle.

Figure 5.5 and Figure 5.6 can be shown as a function of the time to then compare them with ground truth data which is given as a function of the time since each elevation angle data can be related to the time of acquisition.

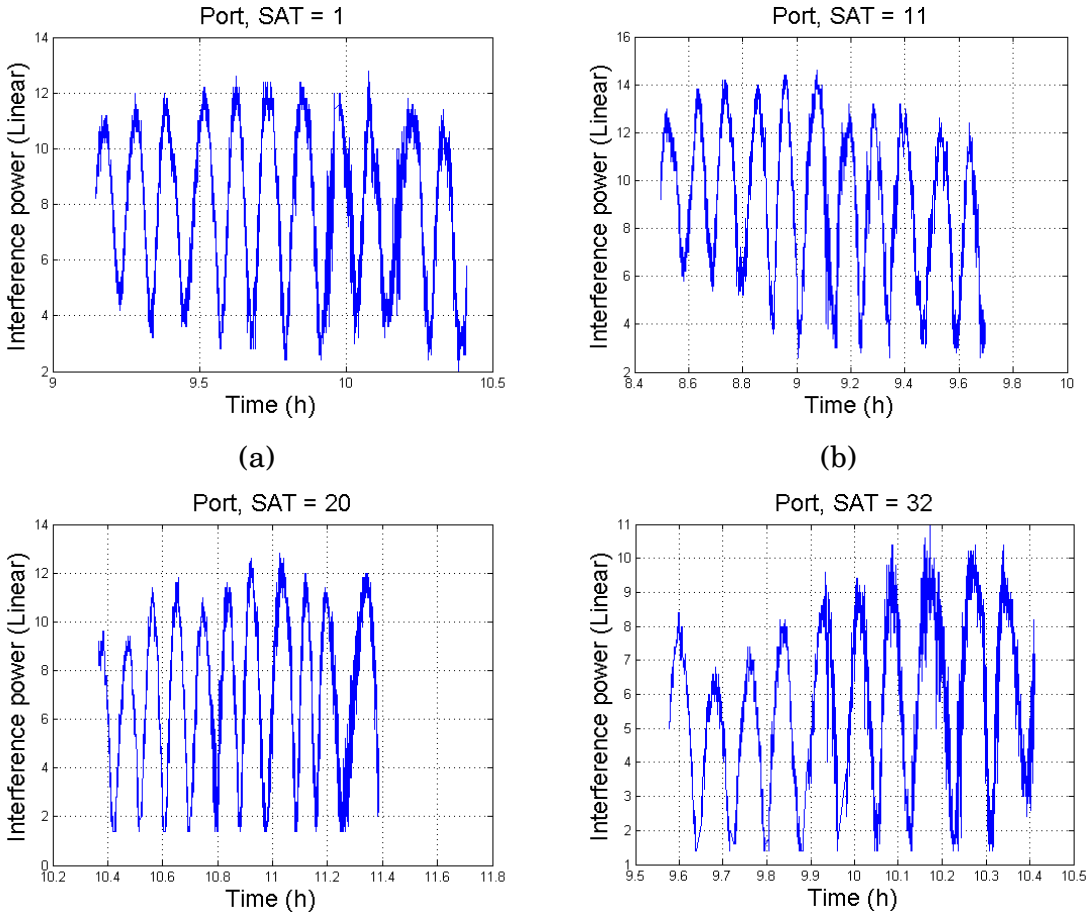

Figure 5.7: Interference power pattern retrieved over time in the morning (7:00h-13:00h, 19/01/2012).

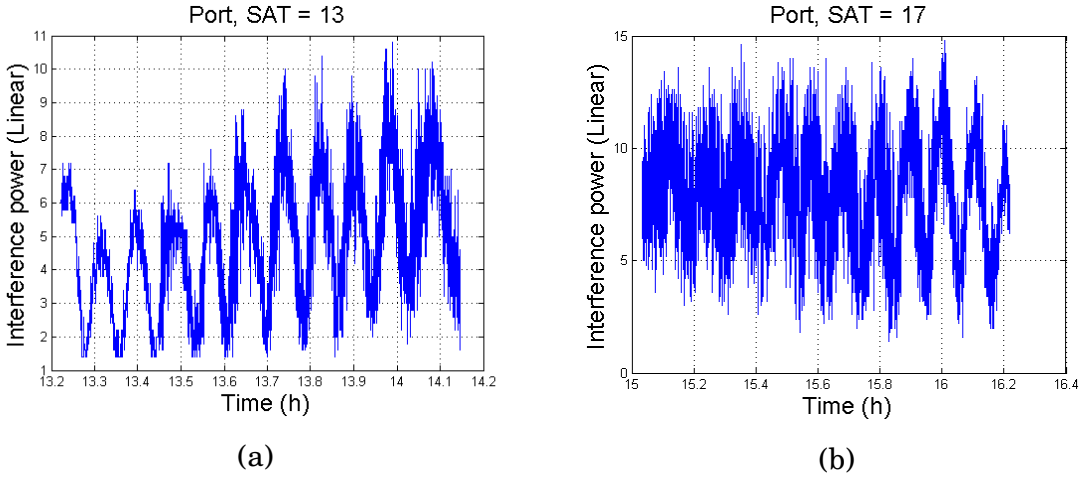

Figure 5.8: Interference power pattern retrieved over time, in the afternoon(13:00f-16:30h , 19/01/2012).

Figure 5.7 and Figure 5.8 show the interference power obtained in linear units as a function of time. The main difference between Figures 5.5 and 5.6, and Figures 5.7 and 5.8 is that units have expressed in dB and linear units, and the x-axis has been changed from elevation angle to time to easily compare with the ground truth data.

One difference that should be remarked from changing the elevation domain for the time domain is that it is easier to identify if the GPS orbit is ascending or descending. All orbits shown here are ascending orbits, despite satellite 17 (Figure 5.6 (b) and Figure 5.8 (b)), which is a descending orbit because when changing from elevation domain to time domain the pattern is inverted. It is seen because the noisiest levels appear in different places of the pattern.

5.3 SIGNAL PROCESSING ALGORITHM

As it is seen from the recovered signals, two different aspects are observed. The low-dynamics behaviour due to the shape of the interference pattern recovered, which is related to the differences in path of direct and reflected signals, and the high-dynamics behaviour due to the backscattering area of the signal, which is related to sea surface roughness and any element involved in it.

Therefore, the first step to process correctly the data is to split the information in two different parts, the low-dynamics, which should give information about height retrievals and consequently sea-tides, and the high-dynamics, which should give information about sea surface roughness. To do that the proposed technique is to is to filter the signal using a Fast Fourier Transform (FFT). For the low-dynamics, the filter applied is a low pass-filter, whereas for retrieving the high dynamics it is a high pass filter.

Figure 5.9 shows the FFT of all the satellites in sight (left column) and the low-pass filtered FFT (right column) to process the low-dynamics and to consequently extract sea-tides information.

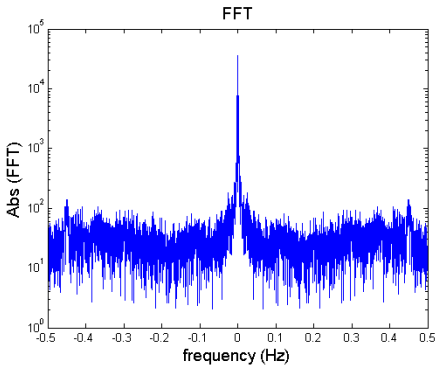

(a)

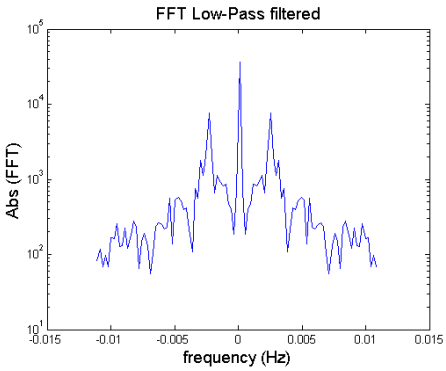

(b)

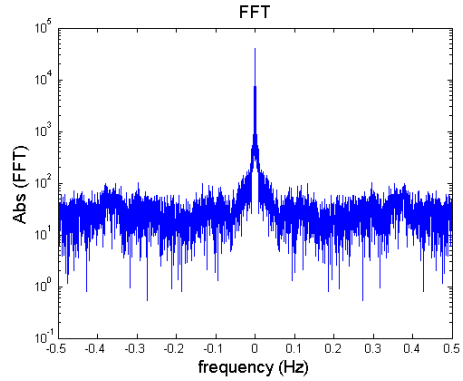
FFT
Abs (FFT)
frequency (Hz)

(c)

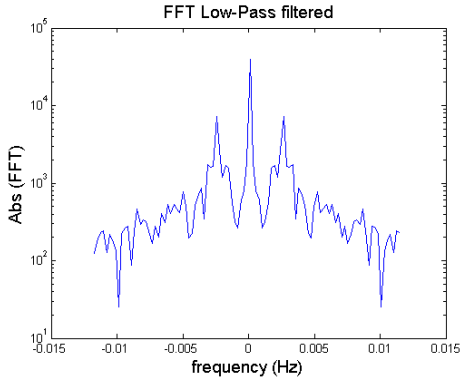
FFT Low-Pass filtered
Abs (FFT)
frequency (Hz)

(d)

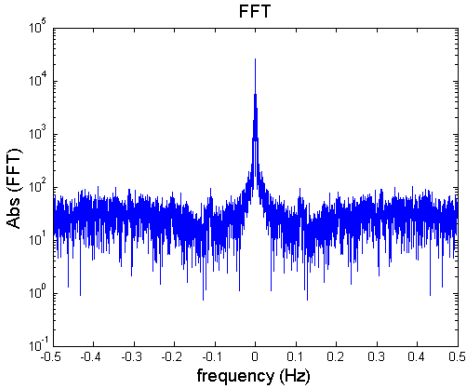
FFT
Abs (FFT)
frequency (Hz)

(e)

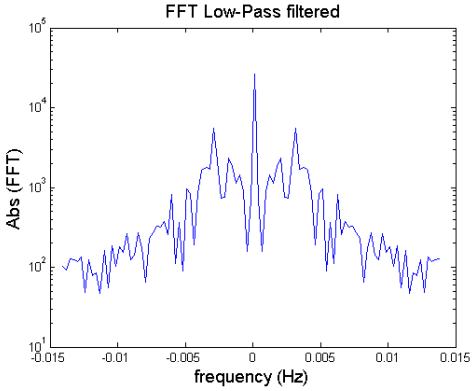
FFT Low-Pass filtered
Abs (FFT)
frequency (Hz)

(f)

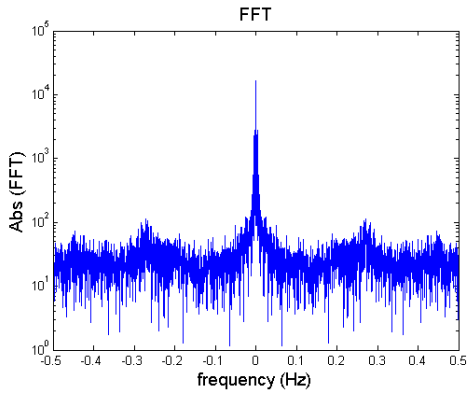
FFT
Abs (FFT)
frequency (Hz)

(g)

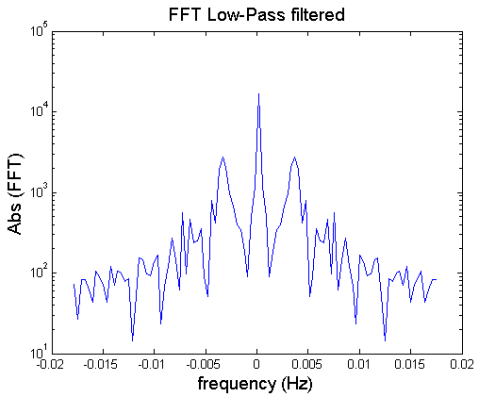
FFT Low-Pass filtered
Abs (FFT)
frequency (Hz)

(h)

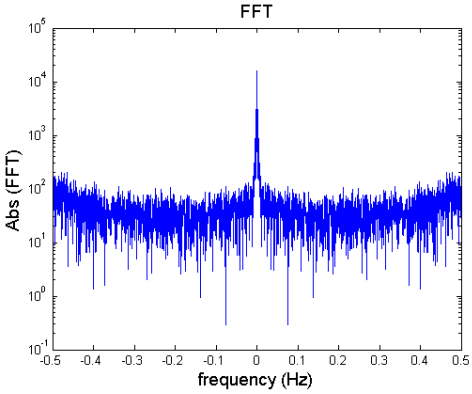
FFT
Abs (FFT)
frequency (Hz)

(i)

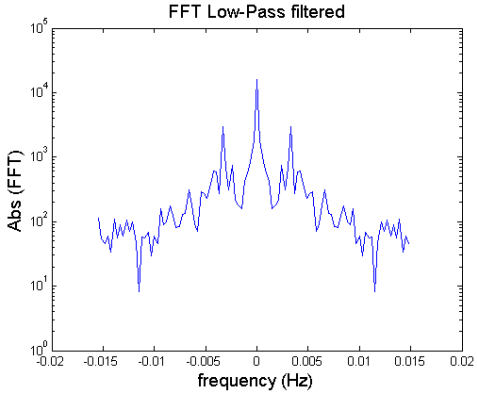
FFT Low-Pass filtered
Abs (FFT)
frequency (Hz)

(j)

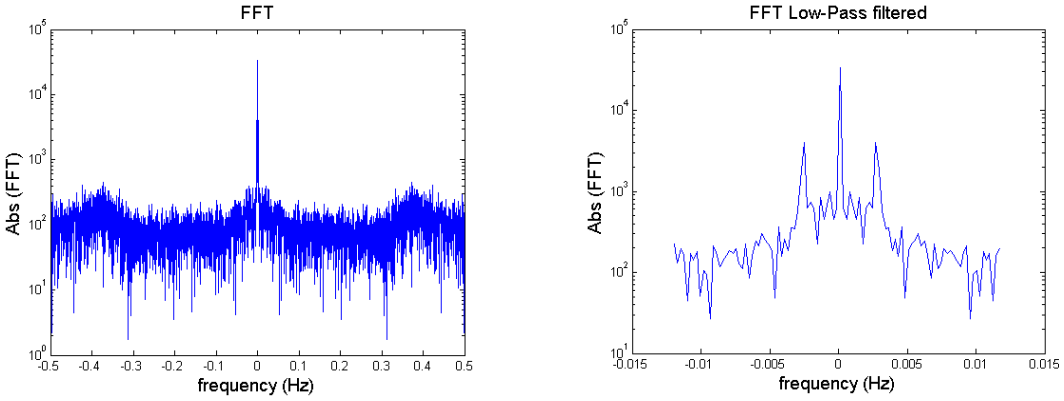

(k) (l)

Figure 5.9: Fast Fourier Transform of the signals obtained and the low-pass filtering applied. (a), (b): SAT1, morning. (c), (d): SAT11, morning. (e), (f): SAT20, morning. (g), (h): SAT32, morning. (i), (j): SAT13, afternoon. (k), (l): SAT17, afternoon.

On the left columns, where the FFT of the interference patterns is shown, one big difference can be seen in the power of the "noisy" zone. The ones from the afternoon retrievals have higher power than the ones in the morning retrievals, and this is related to the higher dynamics, which are seen in the signals shown in Figure 5.7 and Figure 5.8. On the right columns it is seen mainly the periodic effect of the interference patterns, which can be identified by two peaks close to the central one, which is the one related to the "DC" or amplitude modulation (AM) component.

In Figure 5.10 the FFT of the retrieved signals and the high-pass filtering effect is shown. To keep on with the data processing now the Inverse Fast Fourier Transform (IFFT) must be applied to analyse the resulting temporal signals. The topography and water level monitoring algorithm is applied to the low-pass filtered signals, whereas a statistical analysis of the high-pass filtered signals is done.

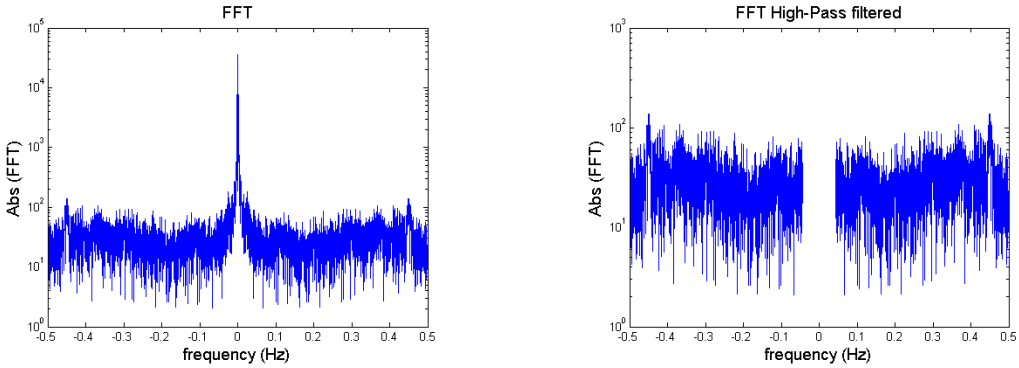

(a) (b)

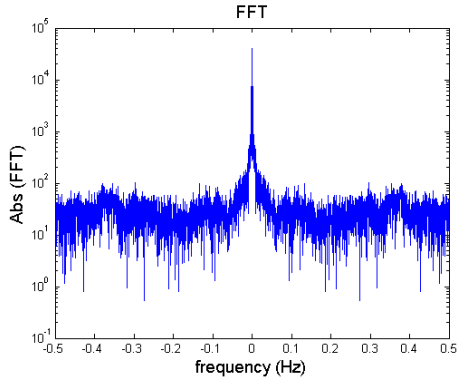
FFT
Abs (FFT)
frequency (Hz)

(c)

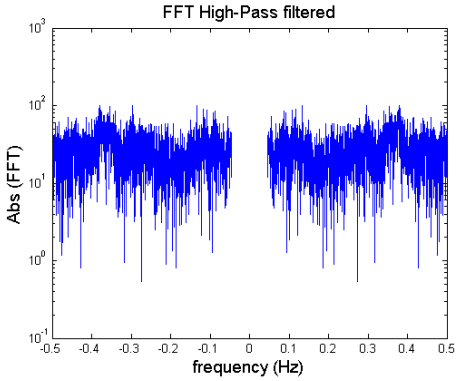
FFT High-Pass filtered
Abs (FFT)
frequency (Hz)

(d)

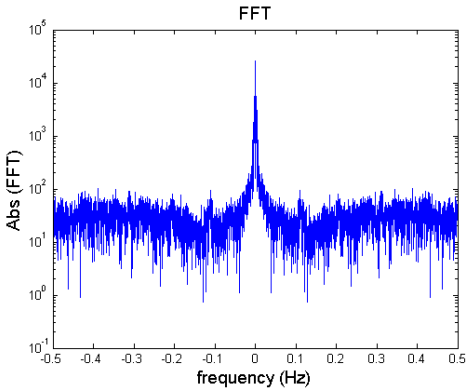
FFT
Abs (FFT)
frequency (Hz)

(e)

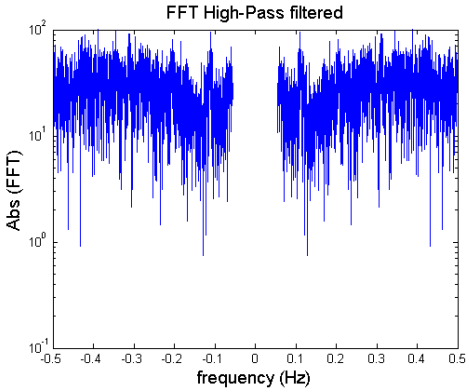
FFT High-Pass filtered
Abs (FFT)
frequency (Hz)

(f)

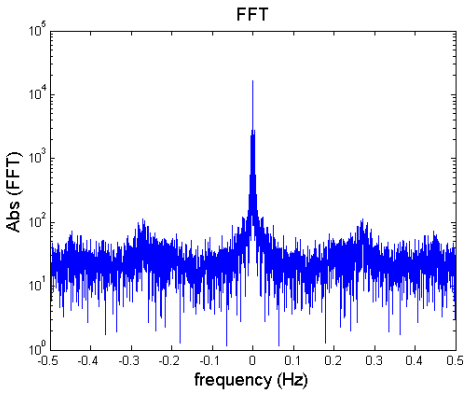
FFT
Abs (FFT)
frequency (Hz)

(g)

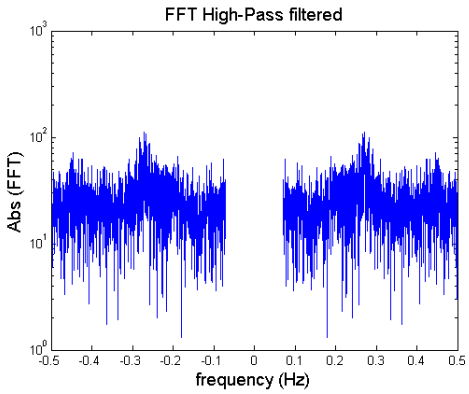
FFT High-Pass filtered
Abs (FFT)
frequency (Hz)

(h)

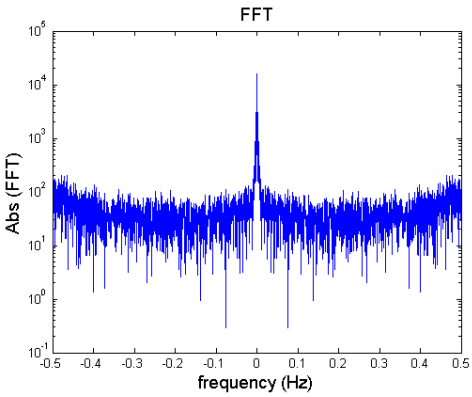
FFT
Abs (FFT)
frequency (Hz)

(i)

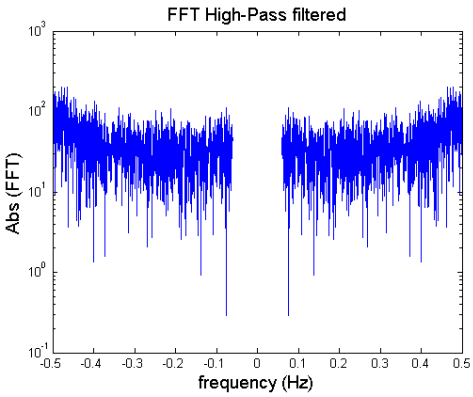
FFT High-Pass filtered
Abs (FFT)
frequency (Hz)

(j)

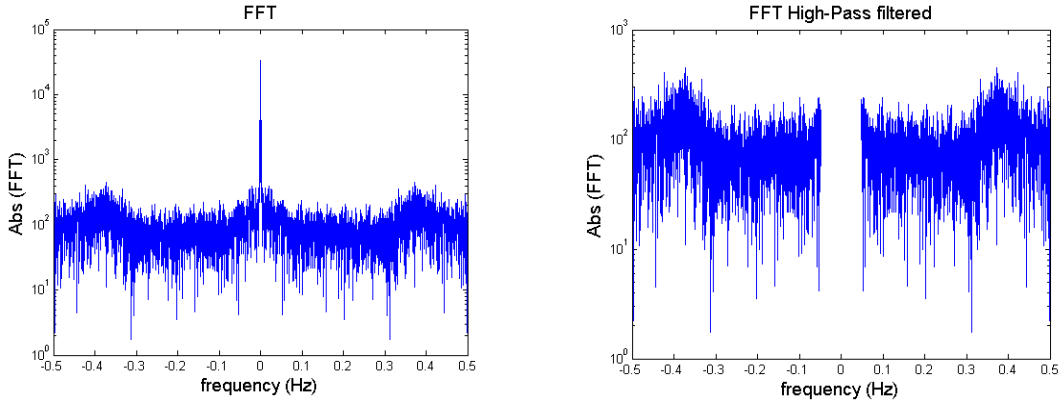

(k) (l)

Figure 5.10: Fast Fourier Transform of the signals obtained and the high pass filtering applied. (a), (b): SAT1, morning. (c), (d): SAT11, morning. (e), (f): SAT20, morning. (g), (h): SAT32, morning. (i), (j): SAT13, afternoon. (k), (l): SAT17, afternoon.

The signals to be processed to obtain the high dynamics effects are shown in the right column. Now, an IFFT is applied to filtered signals obtaining the signals to process accordingly. For the low-pass filtered ones, which are related with the low-dynamics of the sea, the data obtained are shown in Figure 5.11.

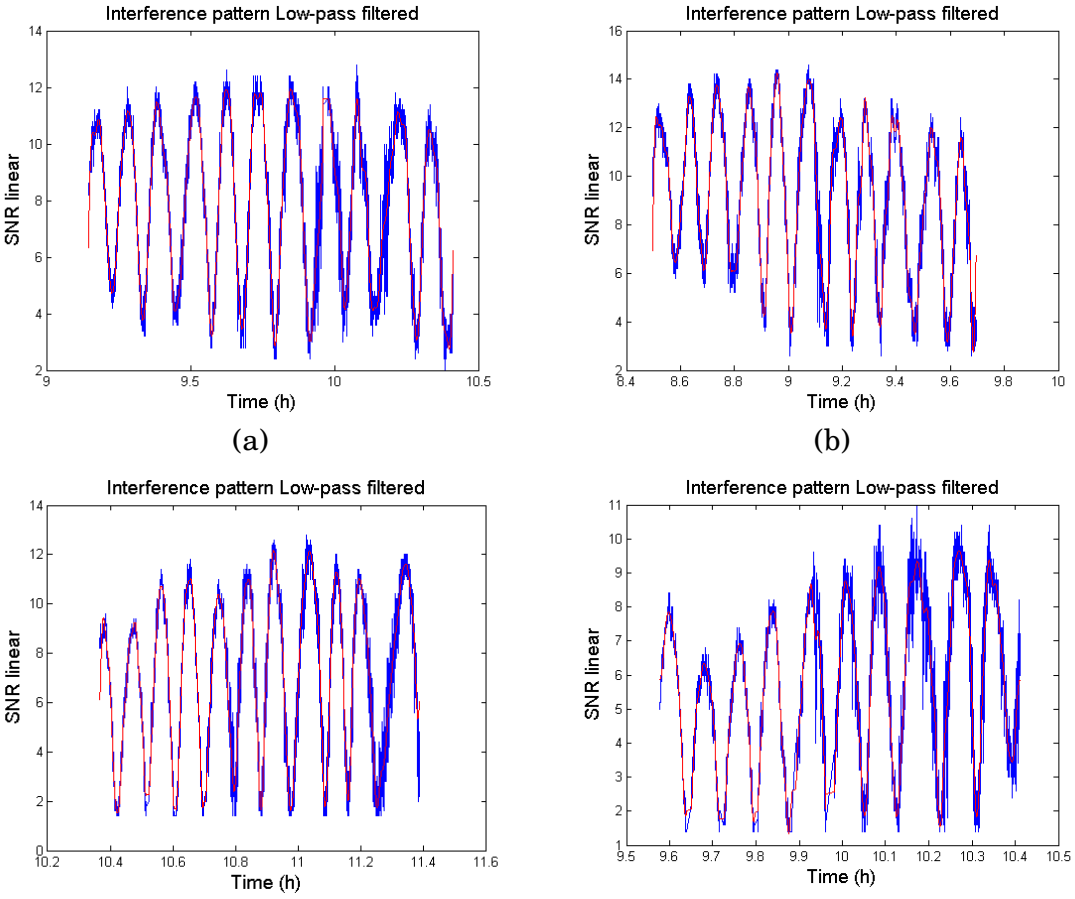

(a) (b)

(c) (d)

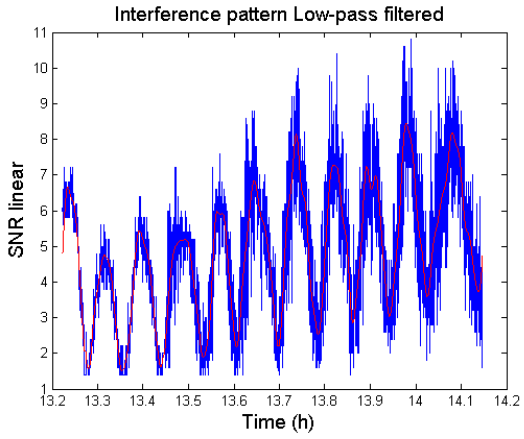

(e)

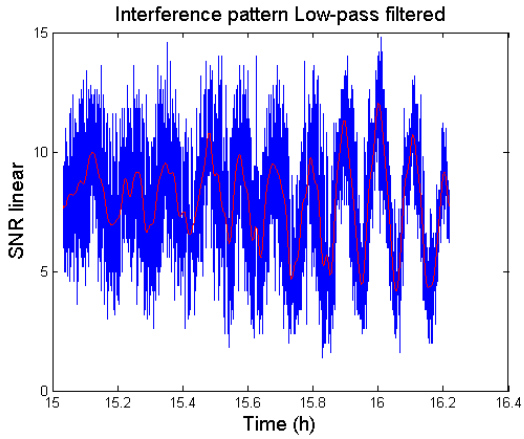

(f)

Figure 5.11: Interference power retrieved as a function of time with the low-pass filtered signals superimposed.

Figure 5.11 shows the signals retrieved from the different satellites (blue) together with the same signals low-pass filtered (red). It is seen that for the ones obtained in the morning (Figure 5.11 (a), (b), (c) and (d)) the shape is totally well preserved whereas for the ones obtained in the afternoon the amplitude information is lost. Further on, it will be seen how this affects the water height retrievals.

Figure 5.12 shows the temporal variation of the high pass filtered signals. As it has been followed until now, (a), (b), (c) and (d) represent the signals obtained in the morning whereas (e) and (f) represent the signals obtained in the afternoon. The noise power effect is seen in the amplitude of the "noise" signals obtained, which was seen before in the FFT presented.

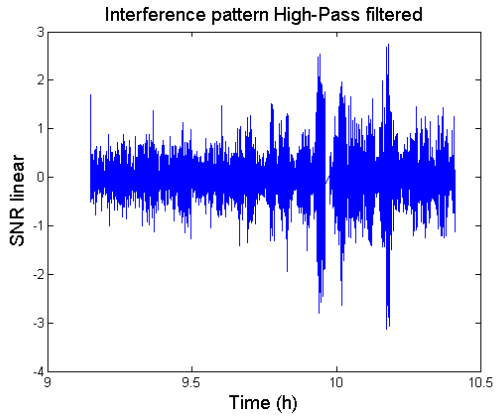

(a)

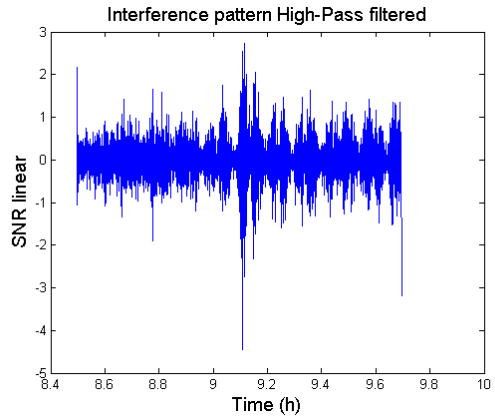

(b)

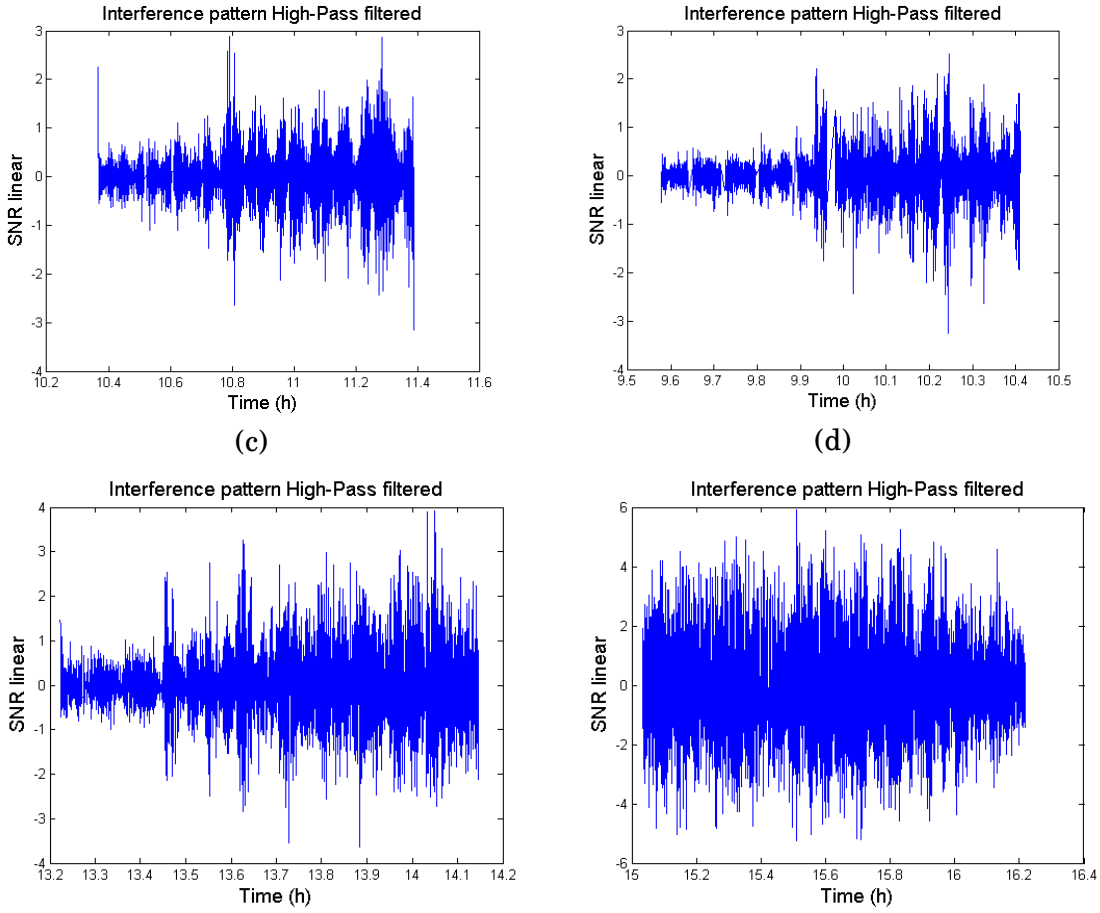

Figure 5.12: Temporal variation of the high-pass filtered signals.

The algorithm to process the high dynamics data is the following:

- FFT of the interference pattern in linear units,
- high-pass filtering,
- IFFT of the high-pass filtered signal, Figure 5.12,
- computing the mean variance,
- removing the peak noisy values due to geometry effect,
- computing the standard deviation of the signals in windows of 10 minutes,
- comparing the values retrieved with ground-truth data, and
- creating an empirical formula.

Once the empirical formula is created, the standard deviation of the high-pass signals is computed, and retrievals can be obtained, (Figure 5.13). A word of caution: this empirical formula should be validated with longer field campaigns.

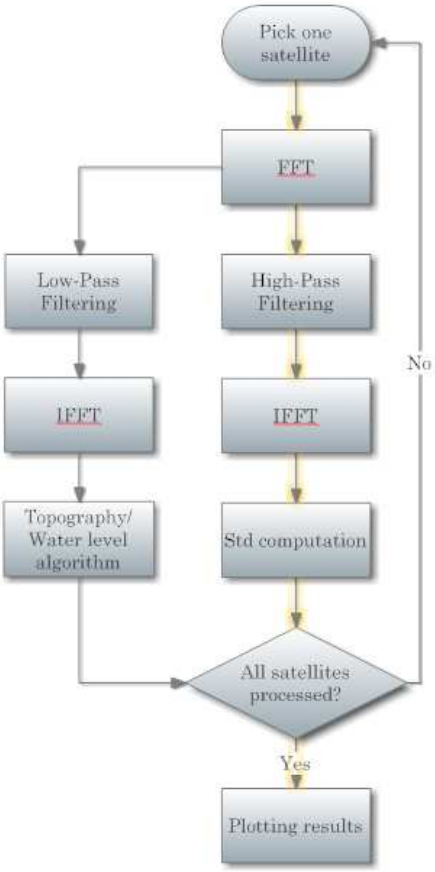

Figure 5.13: Retrieval algorithm.

5.4 RESULTS OBTAINED

In this section the results obtained along the one-day field campaign are shown. Firstly, the sea-tides retrievals are shown in Figure 5.14.

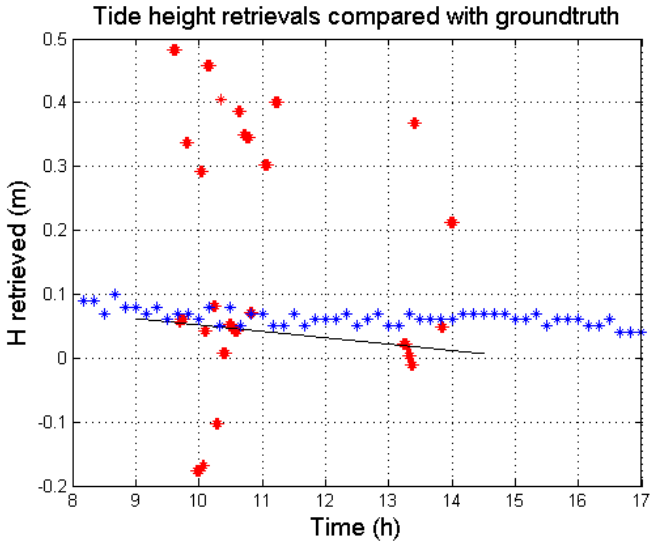

Figure 5.14: Water-height as a function of time. Ground-truth (blue), data obtained (red) regression curve (black).

Looking at the results obtained it can be noted that the algorithm is not working correctly in this case, but some aspects must be commented. To obtain water-height retrievals it is necessary to be in steady-state conditions, at least for each window where a maximum and minimum exist, because the algorithm is extremely sensitive to these positions. A small movement in these positions is translated to retrieval errors and the noise in the signals highly affects to how correctly the estimation of these positions is. A smooth filter has been tried in order to preserve the shape of the signals when they are extremely noisy, but no improvement has been seen.

Then, the high-dynamics effect has been compared with wind speed ground-truth data because in a harbour currents and waves are supposed to be negligible, but if a ship passes or wind blows strong enough some roughness in sea-surface is created and it is seen by the instrument. As a first step the ground-truth is shown in Figure 5.15, where the speed of the wind is monitored in two different ways, mean value (red) and burst wind speed (blue). The green curve represents the difference between them.

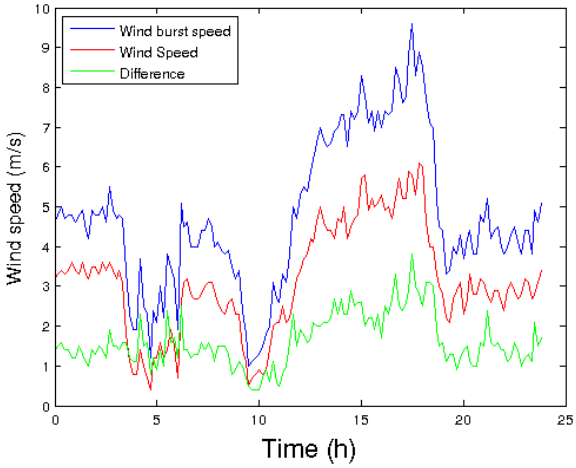

Figure 5.15: Ground-truth data.

Then, the algorithm shown in Figure 5.13 is applied to the data shown in Figure 5.12 plotting them versus the mean wind speed, red curve of Figure 5.15. Results obtained are shown in Figure 5.16. A fitting algorithm is applied to see the correlation between both parameters. The R-square coefficient is 0.9567 which means that the fit is good enough. The fitting curve is shown in eqn. (5.1):

$$Std = a * e^{b \cdot windspeed} + c \tag{5.1}$$

where:

- a=0.0003687,
- b=1.542, and
- c=0.2505.

From eqn. (5.1) if standard deviation is known, wind speed can be retrieved.

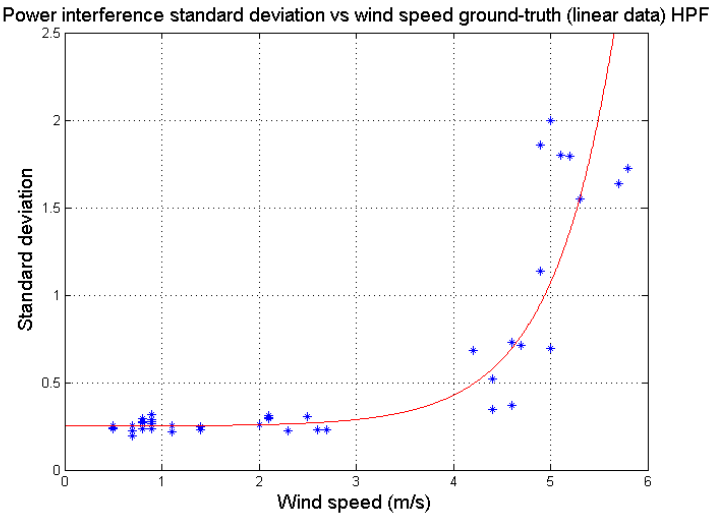

Figure 5.16: Wind speed versus standard deviation of the interference pattern obtained (blue) and the fitting curve (red).

The correlation coefficient of the fitting curve is 0.8, which has been computed with the help of Matlab software, is good enough to rely on the results obtained.

What can be clearly observed from Figure 5.16 is that for wind speeds lower than 3 m/s the sea-surface is not affected since waves do not start to develop. Once the sea starts developing the sea surface is affected and its value follows and exponential line that may be approximated by a linear function in this region. It is reasonable to say that a saturation point might be reached, but to identify that point, higher winds speeds are needed to better fit the data.

5.5 SUMMARY

In this chapter the field campaign carried out in Vilanova i la Geltrú has been presented describing the entire environment. It lasted for 10 hours, but data depended on the available satellite at each moment.

A deep description of the signals obtained is done, and all the elements in them have been interpreted accordingly, and compared to the conditions encountered such as noisy levels due to high-dynamics of the sea.

The signal processing algorithm has been explained in detail showing all the intermediate steps performed. To separate the low-dynamics and the high-dynamics effects observed, a FFT filter is used and then each one is processed with the appropriate algorithm.

Finally, the retrieved parameters are shown as a consequence of applying each algorithm and they are compared with ground-truth data. A critical analysis has been performed and all the differences with ground-truth data are justified.

6 CHAPTER 6 CONCLUSIONS AND FUTURE WORK

6.1 CONCLUSIONS

This Master Thesis has presented a whole analysis of the IPT in order to monitor the sea surface. To do this, the GNSS signals have been introduced giving place to introduce two different GNSS-R techniques as the DDM and the IPT, which are based in very different principles, but both have the same purpose: to retrieve geophysical parameters of different surfaces where they are applied.

The hardware developed is presented in Chapter 3, firstly commenting its restrictions, and justifying its design to meet the IPT requirements to then presenting it with detail. An overview of the whole system is finally given to point out the main characteristics of the hardware.

In Chapter 4 real applications of the IPT are shown. First, the Brewster angle is presented showing its effect in the IPT and the high performance in retrieving land-surface soil moisture because the IPT notch position is extremely sensible to the land surface water content. By looking at the whole pattern a 2-D Map can be obtained. Then, the topography algorithm is presented mainly as a correction factor for the soil moisture retrievals, but it is another application to take into account. As a third step, it has been proven that mean vegetation height can be obtained with success just by comparison of the theoretical notch positions with the ones obtained in the patterns. Finally, it is shown that the topography retrieval algorithm has been used to monitor water-level in reservoirs because its dynamics only changes when some natural elements, such as rain, happen.

As the topography algorithm performs well in water-level monitoring in reservoirs, it has been applied to monitor sea-tides, where dynamics change with higher frequency than in reservoirs. To do so, Chapter 5 presents a field campaign where the only conditions that would affect water-level should be sea-tides. The field campaign is described with high detail remarking the understanding of the concept and showing all the intermediate steps of the algorithms designed. Finally, it is shown that due to the dynamics of the sea, water-level cannot be retrieved with the precision required or the precision proven over reservoirs. On the contrary, it has been shown a high correlation between sea-surface roughness and wind speed,

which can be retrieved just by analysing the standard deviation of the high dynamics of the interference power patterns obtained. An empirical formula has been developed, but additional experimental validation is required.

6.2 FUTURE WORK

As has been seen, following the promising results a longer validation of the empirical wind speed retrieval equation given en section 5.4 is pending. To do so, a longer field campaign is required to obtain much more data to refine the coefficients, as well as to get higher wind speeds.

Also some corrections due to the incidence or elevation angle and the wind direction should be analysed in order to improve the presented equation.

It is advisable also to put the instrument in open sea and look at if sea-waves can be retrieved just by looking once again at the FFT of the interference pattern, because of the periodic effect of the waves must be seen somehow in the measured patterns. The do so, the sampling frequency of the GPS receiver should be increased. Our group is going to do a field campaign on the Pont del Petroli, Barcelona, Spain, where the required conditions are encountered.

Another advisable research line to be done is to enlarge the margin of elevation angles seen of the patterns in the processing algorithm. This should be done because the ε_r of the sea depend on Sea Surface Salinity (SSS) and it has been proven enough how sensitive is the IPT to the Brewster angle which is directly related to the ε_r of the reflecting surface.

REFERENCES

[1] N. Rodríguez Álvarez, Contributions to Earth Observations Using GNNS-R Opportunity Signals, Barcelona: UPC, 2011.

[2] E. Valencia, «On the Use of GNSS-R Data to Correct L-Band Brightness Temperatures for Sea-State Effects: Results of the ALBATROSS Field Experiments,» *IEEE TRANSACTIONS ON GEOSCIENCE AND REMOTE SENSING,* pp. 3225-3235, 2011.

[3] X. Bosch-Lluis, On the design of microwave radiometers with digital beamforming and polarization synthesis for Earth Observation, Barcelona: UPC, 2011.

[4] I. Ramos Pérez et al., «Synthetic Aperture PAU: a New Instrument to Test Potential Improvements SMOSops,» de *IGARSS*, 2012.

[5] J. Tarongi et al., «Multifrequency Experimental Radiometer with Interference Trancking for Experimental over Land and Littoral: MERITXELL,» de *IGARSS*, South Africa, 2009.

[6] S. Gleason and D. Gebre-Egziabher, GNSS Applications and Methods, Boston: Artech House, 2009.

[7] K. Borre, D. M. Akos, N. Bertelsen, P. Rinder y S. H. Jensen, A software-defined GPS and GALILEO Receiver: A single-Frequency Approach, 2007.

[8] M. Martín-Neira, «A passive reflectometry and interferometry system (PARIS): Application to Ocean Altimetry,» *ESA J.,* pp. 331-355, 1993.

[9] J. Garrison, S. J. Katsberg y M. Hill, «Effect of Sea Roughness on Bistatically Scatered Range Coded Signals from the Global Positioning System,» *Geophysical Research Letter,* p. 4, 1998.

[10] A. Komjathy, «Sea Ice Remote Sensing Using Surface Reflected GPS Signals,» *Proceedings of the IEEE International Geoscience and Remote Sensing Symposium,* pp. 2855-2857, 2000.

[11] J. L. Garrison, «Wind Speed Measurements Using Forward Scattered GPS Signals,» *IEEE Transactions on Geoscience and Remote Sensing,* 2002.

[12] V. U. Zavorotny y A. G. Voronovich, «Scattering of GPS Signals from the Ocean with Wind Remote Sensing Applications,» *IEEE Transactions on Geoscience*

and Remote Sensing, pp. 951-964, 2000.

[13] A. Alonso Arroyo, Diseño, Desarrollo y test de una red de sensores inalámbrica para medir la humedad de terreno, Barcelona: UPC/PFC, 2011.

[14] S. Electronics, «Sparkfun Electronics,» [En línea]. Available: http://www.sparkfun.com/products/9013.

[15] Sparkfun, «Sparkfun,» [En línea]. Available: http://www.sparkfun.com/products/9530.

[16] XIOM, «XIOM,» [En línea]. Available: http://www.xiom.cat/vilanova.aspx.

[17] «http://www.insidegnss.com/aboutgps,» [En línea].